MECHANICAL PROPERTY CHANGES IN THE CERAMIC ELECTROLYTE LLZO DUE TO POROSITY, MICROCRACKING AND LITHIUM INCORPORATION

By

Aaron Foster

A THESIS

Submitted to
Michigan State University
in partial fulfillment of the requirements
for the degree of

Materials Science and Engineering - Master of Science

2014

ABSTRACT

MECHANICAL PROPERTY CHANGES IN THE CERAMIC ELECTROLYTE LLZO DUE TO POROSITY, MICROCRACKING AND LITHIUM INCORPORATION

By

Aaron Foster

The intent of this study was to determine the effects of lithium flux on the elastic moduli of the solid electrolyte lithium lanthanum zirconium oxide (LLZO), with a goal of using the elasticity measurements as a gauge of Li dendrite growth. Several LLZO billets were prepared and analyzed using resonant ultrasound spectroscopy (RUS).

The specimens of LLZO had Young's modulus, E, ranging from 90.7 GPa to 129.0 GPa, and the range for shear modulus, G, was 33.62 GPa to 50.65 GPa. Published values for LLZO list E = 149.8 GPa and G = 59.6 GPa at 3% porosity [Ni 2012]. The cause for the difference in elastic moduli values is uncertain. Porosity alone was determined not to account for the difference in moduli among specimens. A microcrack damage model predicted that surface microcracks induced by sanding would result in changes that are too small to be measureable by RUS.

In order to predict whether Li dendrite growth would be detectable by elasticity measurements, several models were considered for LLZO and Li forming a fiber/matrix composite. In addition to fibers (dendrites), Li may also form a solid solution with LLZO, so models based on Nordheim's rule were also considered.

Dedicated to my grandfather
You were the man I will always strive to be

ACKNOWLEDGMENTS

I would like to thank my advisor Dr. Case and Dr. Sakamoto for providing the opportunity to be involved in this study, and to experience true scientific research first hand. Thanks to Dr. Case for the guidance and invaluable expertise he offered over the course of this work, as well as the extensive revision work and for helping me to find the motivation to press on. Without his encouragement and mentoring, this work could not have been done. I would like to thank Dr. Sakamoto and his students Asma Sharafi and Regina Garcia who provided the samples and assisted me in this study.

I would also like to thank Robert Schmidt for showing me the ropes of graduate school, research, RUS and our lab. Though he was a fellow graduate student, his knowledge and guidance made him far more of a mentor than a peer.

The financial support for the research of Next Energy through the grant “Ceramic electrolytes enabling solid state batteries” is gratefully acknowledged.

Lastly, I would to thank my parents who loved me unconditionally and set an example to always work hard. I hope to make you proud.

TABLE OF CONTENTS

LIST OF TABLES

LIST OF FIGURES

1.0 Introduction

Understanding and characterizing the elastic moduli of materials is critical to the development of the products they make. The great interest in batteries today causes a great need for research and development of the materials that compose them such as Lithium Lanthanum Zirconium oxide (LLZO) which is used as a solid electrolyte. Resonance ultrasound spectroscopy (RUS) is a nondestructive method for characterizing the elastic moduli of LLZO so the same specimens could be further tested. In this study, RUS was used to analyze LLZO and better understand its properties.

1.1 Need for Batteries

Improving battery technology is a critical need for modern technology and a major goal for many researchers. The increasing cost of oil and increasing desire to use cleaner forms energy is increasing the demand for electric vehicles (EV). The limiting factor in electric vehicles is the energy supply, which is the battery. The specific energy of current batteries is fairly low when compared to gasoline [Amine 2014]. State of the art lithium ion batteries have specific energy values of 150- 200 Wh kg^{-1} which is only a fraction of gasoline, around 13,000 Wh kg^{-1} [Amine 2014]. The theoretical limit of intercalated batteries is around 900 Wh kg^{-1} and even more exotic designs like Li/S have theoretical limits around 2600 Wh kg^{-1} [Amine 2014]. However, electric vehicles can be very efficient, with 80-90% of the energy in the battery going to propulsion [Delucchi 2014]. For gasoline powered vehicles, only about 25% of the energy is used for motion [Chau 2007]. Materials are being researched with the goal that future batteries will make EVs competitive with internal combustion engine (ICE) vehicles.

Another major area of interest for batteries is load leveling [Whittingham 2012]. Solar and wind energy have received a lot of attention because the energy can be harvested locally, and without emissions [Amine 2014] . However the intermittent supply of energy from solar and wind sources makes these technologies unsuitable to the current grid [Whittingham 2012]. If large scale batteries could be developed, solar and wind energy could be utilized to a much greater extent [Goodenough 2010; Whittingham 2012; Amine 2014].

Furthermore, portable electronics have become ubiquitous in the modern world. The increasing usage of cell phones, laptops, music players and other devices will also drive the demand for battery performance, both in terms of power output and energy density.

1.2 Lithium-Ion Battery Components

A battery is a system with one or more electrochemical cells that convert chemical energy to electrical energy [Huggins 2009]. Figure 1.2.1 shows the basic components of a lithium ion battery. On the left is the negative electrode, or anode, which is where the electrons leave the battery to power an external circuit as the battery is discharged [Dunn 2011]. As the battery is discharged electrons will exit the cell to provide energy to an external circuit [Dunn 2011]. To balance the loss of the negatively charged electrons, positively charged ions leave the anode and travel through the electrolyte. The lithium ions and the electrons arrive at the positive electrode or cathode via different routes. The electrolyte can be a solid or a liquid but it must not be an electrical conductor, or its electrical conductivity must be so low it is negligible.

For the electrochemical cell to function there must exist a chemical driving force between the electrodes, which is the difference in the chemical potential [Huggins 2009]. In lithium batteries the chemical driving force is due to the lithium ions inclination to move from

the anode to the cathode. This can be measured by the difference between the Gibbs free energy of formation for the products and reactants:

$$\Delta G_{rxn}^{o} = \Sigma\, \Delta G_f^{o}(\text{products}) - \Sigma\, \Delta G_f^{o}\ (\text{reactants}) \qquad 1.2.1$$

where ΔG_{rxn}^{o} is Gibbs free energy change per mole of reactant and ΔG_f^{o} is the Gibbs free energy of formation [Huggins 2009] both expressed in units of joules per mole.

When the battery is not externally connected, there will be an internal electrostatic driving force in the opposite direction as the chemical driving force that prevents or inhibits the reaction [Huggins 2009]. The maximum work that the electrostatic force can exert can be expressed by

$$W_{max}=nFE \qquad 1.2.2$$

where n is the moles of electrons, F is Faraday's constant and E is the cell voltage [Vincient 1984].

Because the electrostatic force and the chemical potential are balanced [Huggins 2009]

$$W_{max}= -\Delta G_{rxn}^{o} \qquad 1.2.3$$

and, therefore

$$\Delta G_{rxn}^{o} =-nFE \qquad 1.2.4$$

The label for anode and cathode is reversed when the battery is charging [Huggins 2009]. To avoid confusion this thesis will only consider the condition when the battery is being discharged. Components for the battery are discussed in more detail below.

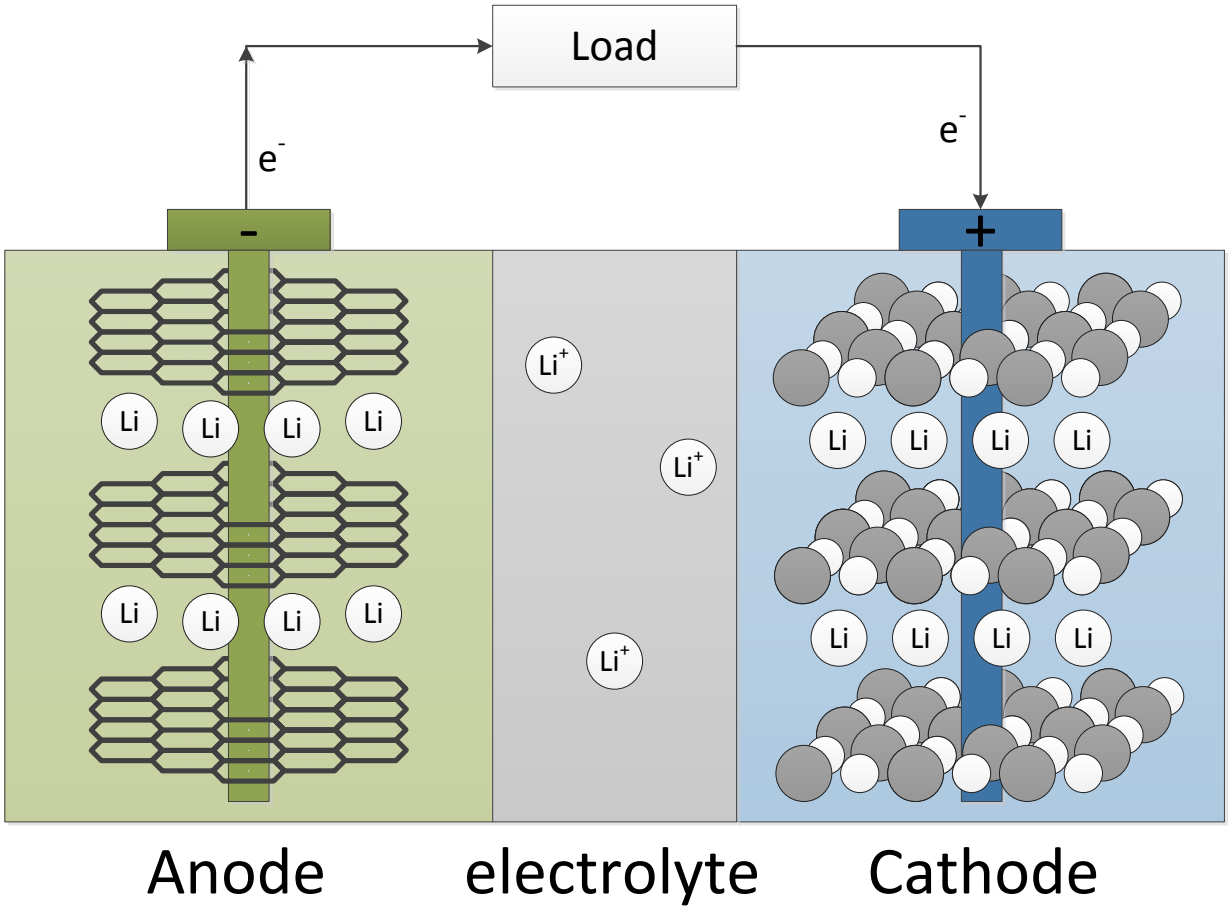

Figure 1.2.1 Diagram of the basic components of a lithium ion battery, not drawn to scale or proportion. The anode on the left is composed of graphene layers with lithium intercalated between the layers. The cathode on the right represents various compounds that also intercalate lithium such as CoO_2, TiS_2 and many others. The electrolyte in the middle can be a polymer, a non-aqueous liquid or a ceramic. (adapted from figure 3 from Dunn et al.[Dunn 2011] and Figure 1 from Bruce et al.[Bruce 2008])

1.2.1 Intercalation Electrodes

Until lithium ion batteries were created, most electrode materials consisted of a homogeneous metal or alloy [Vincient 1984]. Lithium-ion batteries are different, they operate as an insertion reaction electrode [Huggins 2009]. In this type of electrode, a host species has a stable crystal structure that forms many parallel planes [Ebert 1976]. Another species can be inserted to or removed from the voids between these planes without destroying the host structure [Huggins 2009]. This is called an intercalation reaction. For a visual representation,

see Figure 1.2.1. The host structure may be altered by changes in the stacking order, volume or bond distance [Ebert 1976].

Intercalation was precisely the advance that made rechargeable lithium batteries possible. Lithium metal is highly reactive and has safety and structural issues when the battery is recharged. Lithium in batteries could be made much more stable by placing the particles into another compound. Rather than lithium ions interacting, the lithium particles are separated by the host species. During charging or discharging, they become ionized and move across the battery, thus the name lithium-ion batteries.

Many different crystal structures are utilized for intercalation electrodes. For the anode side of a Lithium ion battery, graphite is commonly used, making a chemical composition of LiC_6 [Bruce 2008]. TiS_2 was the first intercalation cathode material (Figure 1.2.2). Each sulfur atom connects to three titanium atoms. Each titanium atom occupies an octahedral site and connects to six sulfur atoms. These structures form into layers where Li-ions can be inserted. $LiCoO_2$ is a common cathode material that forms a similar structure.

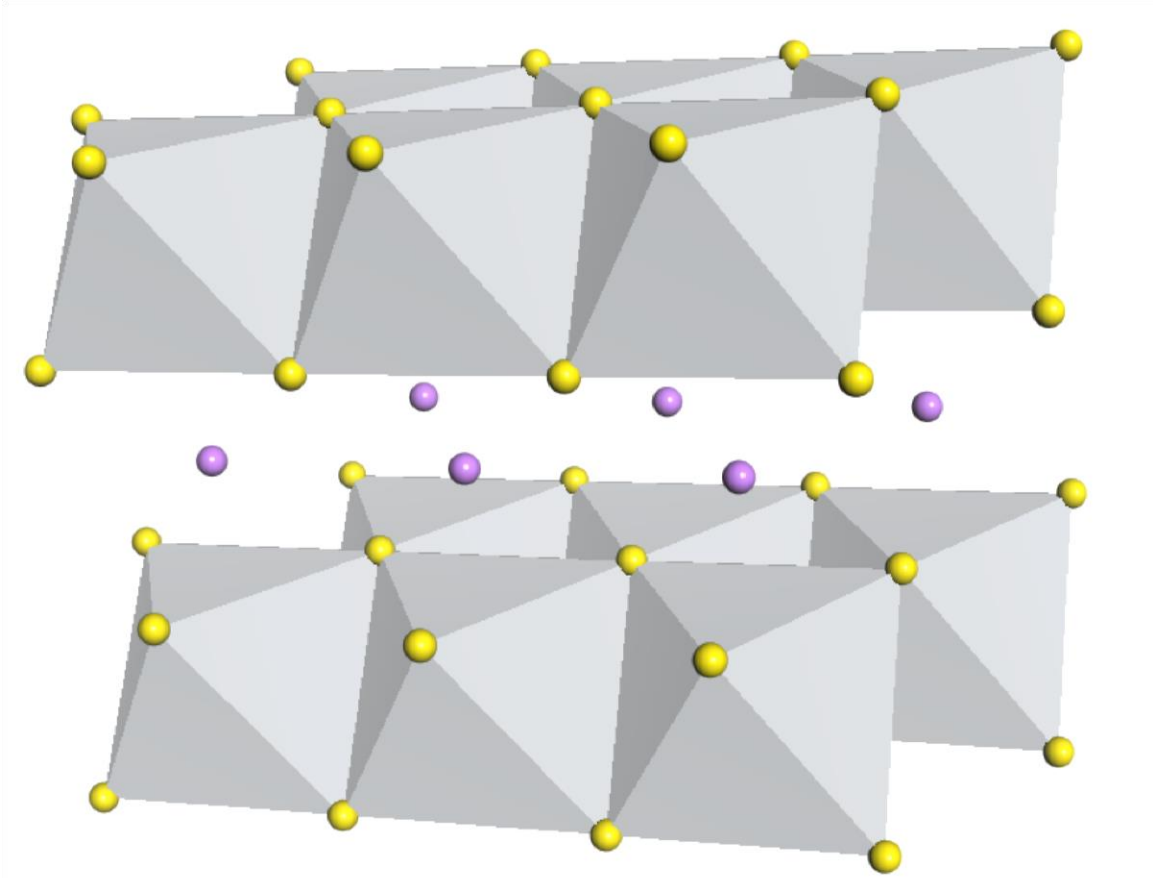

Figure 1.2.2 A diagram of TiS_2 intercalation cathode. The titanium occupies octahedral sites and the material forms into layers in which the lithium ions can insert. Yellow atoms are sulfur and the purple atoms are lithium.

Another popular crystal structure for a cathode material is the spinel structure named after the naturally occurring mineral that bares this structure, $MgAl_2O_4$ [Barsoum 1997a]. It can be expressed as the general formula AB_2O_4, where A has an oxidation state of $^{+2}$ and B has an oxidation state of $^{+3}$. In the case of a normal spinel, A^{2+} occupies tetrahedral sites and B^{3+} occupies octahedral [Barsoum 1997a]. The structure has a face centered cubic stacking of the A ions. Some examples of spinel cathodes are $LiMn_2O_4$ [Amine 2014], $LiTi_2O_4$ and $LiTi_2S_4$ [Goodenough 2010]. Spinel materials are structurally and thermally stable during lithium extraction and spinel materials used for cathodes can have a voltage of over 3V against Li^+/Li anode [Goodenough 2010].

Similar to the spinel structure is the olivine structure. In 1997, the olivine material $LiFePO_4$ was developed for use as a cathode material [Nanjundaswamy 1997]. Olivines have a hexagonal closed packed structure [Barsoum 1997a]. $LiFePO_4$ is probably the most popular olivine cathode because of the low cost of the materials; but Ni, Co and Mn can replace Fe [Whittingham 2012]. In $LiFePO_4$, phosphorus occupies tetrahedral sites and the iron occupies octahedral sites. the crystal has 1D tunnels for Li deposition [Goodenough 2010]. A visual representation of this material can be seen in Goodenough [Goodenough 2012].

1.2.2 Solid Electrolytes

Solid electrolytes have been known for several decades, and have seen a strong growth in interest in recent years [Takada 2013]. Solid electrolytes can offer enhanced durability and safety over liquid electrolytes [Fergus 2010], they are also more stable and are also less likely to form side reactions when compared to liquid electrolytes [Takada 2013]. This is because liquid electrolytes can act as a solvent for many compounds, whereas solid electrolytes typically only conduct one type of species and are less reactive with other species [Takada 2013].

There are two main types of solid electrolytes: polymers and ceramics [Fergus 2010]. A popular polymer is polyethylene oxide (PEO) which can have various salts dissolved into it while the polymer is being processed [Thangadurai 2003]. Polymer electrolytes tend to be less rigid and easier to produce [Fergus 2010]. Ceramic electrolytes have higher elastic moduli and are more resilient to high temperatures and abusive environments [Fergus 2010]. The weakness for ceramic electrolytes is their low ionic conductivity. The conduction of ions requires the movement of point defects, which requires energy. Consequently, conductivity goes up in ceramics as the temperature increases [Fergus 2010].

In 2003 Thangadurai et al. developed lithium ion conducting garnet materials of the composition $Li_5La_3M_2O_{12}$ (where M could represent different metals) for use as a solid electrolyte [Thangadurai 2003]. One metal that seemed particularly attractive was tantalum, with an electrolyte composition of $Li_5La_3Ta_2O_{12}$ which could operate at room temperature. It showed improved conductivity over other well-known Li ion conductors such as $Li_{2.88}PO_{3.73}N_{0.14}$ (LiPON) and lithium beta-alumina [Thangadurai 2003]. $Li_5La_3Ta_2O_{12}$ was also shown to be stable against molten lithium metal, which attest to the stability of the material [Thangadurai 2003].

1.3 Lithium Deposition

The phenomenon of lithium deposition has been extensively documented [Amine 2014; Brandt 1994; Goodenough 2010; Goodenough 2012; Qi 2010; Kanno 1989; Li 2014]but not fully understood. One idea that is clear and agreed upon, is that unregulated lithium deposition can pose a major threat to the safety and cycle life of lithium and lithium ion batteries, and addressing this issue will be critical to advancing battery technology. When a lithium battery is cycled, lithium ions will pass back and forth between the anode and cathode through the electrolyte. Ideally, when the ions come back to the anode they should redeposit in a uniform layer, but this is not always observed.

1.3.1 Lithium Deposition and Dendrite Formation in Electrolytes

There have been numerous studies on dendrites in liquid electrolytes. In lithium metal batteries, lithium deposition on the surface of the anode is intended but its morphology is difficult to control [Li 2014]. Defects, such as cracks, pits or grain boundaries, can cause uneven deposition below the Solid Electrolyte interphase (SEI) [Li 2014]. This can cause small

protrusions which are described as mossy or granular, but can stay confined within the SEI layer [Li 2014]. If there is a sufficient current density or the protrusion is quite large, it can grow beyond the plane of the SEI [Li 2014]. Subsequently, the protrusions can evolve into long fiber or branch like structures called dendrites [Li 2014]. The exact mechanism as to how dendrites grow is cause of some debate. Early models predicted that the dendrites would grow from the tip as ions are deposited at the end [Barton 1962]. Later models predicted that dendrites grow out from the surface of the anode [Yamaki 1998] Others predicted somewhat of a hybrid theory: the dendrite initially grow from the base, but the lithium ions will eventually to deposit on the tip of the dendrite [Nagy 1997].

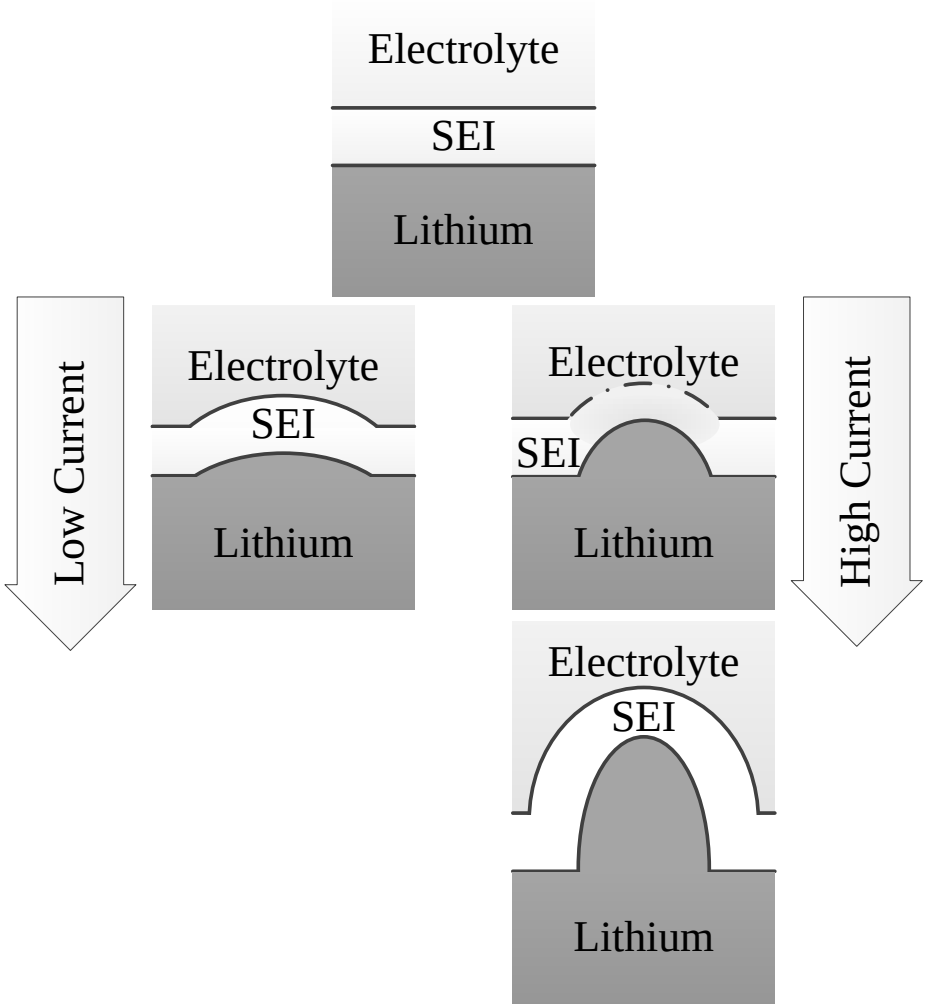

Figure 1.2.3 An illustration of lithium deposition in a lithium metal electrode. SEI stands for Solid electrolyte interface. The top box is the starting point where the surface of the metal anode is relatively smooth. If there is low current, the process moves to the middle left image where lithium deposits under the SEI. If the current is high, the lithium deposits under the SEI too rapidly, and the volume change causes the layer to break. There is much less ionic resistance so more Li^+ move towards that point causing the growth of the protrusion. If the current stops, the SEI layer reforms around the protrusion. Adapted from Aurbach [Aurbach 2002]

Most researchers agree that when the electrolyte surface has been covered with protrusions and the current is high enough, the ions will begin to deposit at the tip of the dendrites and dendrite growth will continue with further cycling, see Figure 1.2.3 [Li 2014]. If the dendrites grow until they extend from the anode to the cathode, the battery will be short circuited resulting in a drop in battery voltage [Rosso 2006]. Even worse, the short circuit can

cause explosions or fires in the battery [Aurbach 2002]. The heating or explosion can occur because the electrolyte is an electrical insulator, but Li metal is a very good electrical conductor. When a dendrite connects the anode to the cathode, a surge of electricity can flow through the dendrite, causing very rapid Joule heating [Wen 2012].

1.3.2 Filaments

A similar phenomenon similar to dendrite formation is Filament growth. The formation of a filament is similar to the formation of a dendrite. A defect in the anode or in the SEI layer leads to a high amount of lithium deposition at one point [Huggins 2009]. As the filament grows, the SEI layer will be less thick at this protrusion than at the surface of the anode. This causes diffusion to occur much easier along the protrusion [Huggins 2009], similar to dendrite formation. The protective layer gets thinner along the protrusion as it gets further away from the surface of the anode. Therefore, more lithium will deposit towards the tip [Huggins 2009]. During discharge, if the lithium is taken away from the protrusion at a uniform rate across the surface, the protrusion will disconnect. Therefore, the filament is taken away from the reaction process, so the lithium can be considered dead and the capacity of the battery is reduced [Huggins 2009].

1.3.3 Anodes as a Means to Control Lithium Deposition

Perhaps the most effective strategy for stopping dendrite formation that is presently available is the use of intercalation electrodes. When a lithium ion battery is recharged, the ions diffuse through the electrolyte and then diffuse into the intercalated anode. If the lithium ions are again intercalated, the ions are kept separate from one another in the anode, thus eliminating the possibility they could form dendrites. However, if the ions arrive at the

anode/SEI layer faster than they diffuse into the anode, a surface layer of Li can be deposited on the anode surface [Purushothaman 2006], then the battery would face the same issues as a lithium metal battery. Overcharging can also cause lithium deposits to occur on the surface of a graphite anode [Li 2014]. This is because the anode cannot intercalate any more of the lithium trying to diffuse in so the ions in the SEI layer will instead be deposited on the surface [Li 2014]. Graphite is the most common of the intercalation anodes. If lithium particles can interact, dendrite or deposition issues may ensue, but intercalation electrodes inhibit this.

Other strategies for limiting lithium dendrite growth include using metal electrodes. Al, Sn or Si will form lithium alloys and will help to keep lithium particles from interacting and generating dendrites, but most alloy-forming electrodes experience large volume changes (320% and 260% for Si and Sn, respectively) which tends to pulverize the anode resulting in irrevocable capacity loss[Zhang 2011].

Many methods have been used to try to overcome dendrite growth. In lithium ion batteries, increasing the size of the anode relative to the cathode, or increasing the surface area of the anode, can suppress the dendrite growth [Tang 2009]. To reduce charging time without enabling dendrite growth, pulse charging has been utilized [Purushothaman 2006]. The pulse charging concept is based on the idea that by quickly saturating the interface, but not exceeding the saturation level, maximum lithium diffusion into the anode will occur. At a constant charge rate, Purushothaman [Purushothaman 2006] observed that the time it takes to saturate the interface could be up to an hour. By the same concept, dendrites can be avoided in lithium ion batteries if they are charged over a long period of time so that the SEI is never saturated with lithium [Li 2014]. This would be acceptable if the batteries were allowed long lengths of time to recharge, and if the batteries were never exposed to frequent charging and discharging that

may lead to spikes in lithium at the SEI layer. Unfortunately, this would make most applications of batteries (laptops, music players, electric vehicles) much less practical.

In Lithium metal batteries, the approach is somewhat different. Rather than trying to prevent conditions that can cause lithium deposition on the surface, the focus is to manage lithium deposition on the surface so that dendrites do not evolve [Li 2014]. It has been observed that using a lower current densities will cause the lithium protrusions that form on the surface of the metal anode to be mossy in nature rather than dendritic [Li 2014]. What exactly defines "high" current density is not precise. Current densities as low as 0.2 mA cm^{-2} with a lithium metal anode can generate protrusions [Dollé 2002], but they may only become mossy up to current densities of 0.45 mA cm^{-2} [Orsini 1998]. Other sources report dendrite formation at 0.5 mA cm^{-2} [Jeong 2008]. Experiments such as those done by Orsoni et al. observed clear dendritic growth above 2.2 mA cm^{-2} in a system with a lithium metal anode [Orsini 1998]. For many experiments that are deliberately avoiding dendrites, the current density is kept below 1 mA/cm^{-2} [Whittingham 1976; Kanno 1989; Yazami 1983]. But again, this is impractical for most realistic battery applications.

Recent work also shows that defects in the subsurface of the lithium metal anode may be the cause of dendrites [Harry 2014]. Using hard X-ray tomography, Harry found small irregularities forming below the metal surface before protrusions started forming on the surface. Harry et al.[Harry 2014] suggests that the structures are what dendrites on the surface nucleate from. These structures form due to the presence of defects, most likely chemical contamination [Harry 2014].

1.3.4 Electrolytes as a Means to Control Lithium Deposition

There are many methods for suppressing dendrite formation in electrolytes. In liquid electrolytes, increasing concentration of the salt, such as $LiPF_6$ or $LiClO_4$, could accommodate a thinner SEI layer which would then offer lower resistance to the ions so they would pass through more rapidly [Jeong 2008]. This has been observed to increase the number of cycles before the capacity drops to zero in a lithium metal battery with a liquid electrolyte [Li 2014].

Yet another method for suppressing dendrite growth with a metal lithium anode is the application of mechanical pressure in the electrolyte [Li 2014]. Gireaud et al. showed that if the lithium anode contacts a liquid electrolyte, then the cycling efficiency increased as the pressure increased over a range from 0.7 kg cm^{-2} to 7 kg cm^{-2} [Gireaud 2006]. Gireaud et al. [Gireaud 2006] state that the development of dendrites was unavoidable and was caused by defects in the microstructure of the lithium anode, such as cracks or stress lines.

Another method used to try to suppress dendrite growth was to increase the operating temperature of the battery to help the ions diffuse through the SEI layer and prevent a buildup of ions at the surface of the SEI [Mogi 2001; Li 2014]. Conversely, Park [Park 2008] found increasing the temperature during recharging, while holding the current constant, would actually enhance the dendrite formation. In the study by Park [Park 2008], it was observed that as the temperature of the electrolyte material was increased, the resistance decreased, so in order to keep the same current, the voltage also had to decrease. Li [Li 2014] suggests that the contradiction in the findings may be a result of the SEI layer forming slower at lower temperatures. Therefore, when the entire system is at an elevated temperature because of ambient conditions, the SEI layer between the anode and electrolyte will form more rapidly than at lower temperatures; but if the increase in temperatures is created by the resistance in the

electrolyte, the SEI will still be at a lower temperature to start with and will form slower than in the case of elevated temperatures from an ambient conditions [Li 2014].

Many battery designs use solid and liquid electrolytes together [Johnson 1998; Goodenough 2010]. The solid electrolytes can slow the process of dendrite growth [Fergus 2010; Miyashiro 2005]. However, Rosso et al. observed dendrite growth through a solid polymer electrolyte that led to cell failure [Rosso 2006]. Dendrite growth in solid electrolytes has been observed elsewhere, either at the anode/electrolyte interface or by penetrating the electrolyte itself [Orsini 1998; Fergus 2010; Dollé 2002; Sakamoto 2013]. If the solid electrolyte has a shear modulus of twice that of the lithium, surface roughening between the anode and solid electrolyte interface can be suppressed [Monroe 2005]. Furthermore, Monroe and Newman calculated that at a high enough shear modulus for the electrolyte, dendrites will be prevented from penetrating into the electrolyte altogether [Monroe 2005].

1.4 Major Developments in Lithium Ion Batteries

There has been numerous challenges in creating lithium batteries, and there has been even more efforts to overcome them. As early as the 1960's there was research into secondary lithium batteries, but they mostly focused on high temperature systems [Jasinski 1967]. The first rechargeable lithium-ion batteries would come from the work of M.S. Whittingham while working for Exxon [Fletcher 2011]. In 1976 he reported the first use of a lithium intercalating material for electrochemical energy storage at ambient room temperatures [Whittingham 1976]. Titanium disulfide (TiS_2) was used as a cathode, metallic lithium was used as the anode and a liquid organic solution was used as the solvent [Whittingham 1976]. The experimental batteries in this research were able to be cycled over a thousand times and had a theoretical density of 480Wh/kg, contemporary batteries were only able to achieve this charge at elevated

temperatures [Whittingham 1976]. A major drawback to this research was the low current densities 1-10 mA cm^{-2} [Mizushima 1980]. Materials for the anodes, cathodes and electrolytes would have to be further developed to achieve higher power output.

A group led by John. B Goodenough developed the $LiCoO_2$ cathode, which was an improvement over the previous cathode because the theoretical specific energy would be over 1 kWh kg^{-1}[Mizushima 1980]. The voltage was also improved, over 4 volts in $LiCoO_2$ versus about 2 volts in titanium disulfide [Mizushima 1980]. However, the current density had to remain low because of issues with the available electrolytes and the lithium metal anode [Mizushima 1980]. At high current density or voltage, the liquid electrolyte could break down [Mizushima 1980]; and lithium deposition was also a major concern. According to Mizushima, using an anode other than lithium metal reduced the voltage that can be obtained from the battery [Mizushima 1980]. The high voltage of the $LiCoO_2$ cathode opened the door for different anode materials to be used [Mizushima 1980].

The graphite electrode was first successfully used in 1983 by utilizing a solid electrolyte, polyethylene oxide [Yazami 1983]. In this setup, the graphite electrode was used as the cathode and lithium metal was used as the anode. To maintain high efficiency when cycled, the cell was still limited to low current densities like the cells that first used TiS_2 and $LiCoO_2$. By the late 1980's many carbon based materials were being used for intercalation anodes [Kanno 1989].

Sony made further improvements on this developments and in 1991 they were able to introduce the first commercial lithium ion battery [Amine 2014]. This battery had a practical specific energy of 90 Wh/kg, which was almost double that of Nickel Cadmium based batteries,

and at least 10% more than Nickel metal hydride, the two closest competing chemistries that were commercially-available [Fletcher 2011].

A history that seems to run intertwined with batteries is the developments of the solid electrolyte. In the 1960's, researchers at Ford Scientific Laboratory made the discovery of an alkali metal conducting material [Huggins 2009]. This was quite different from the batteries of the time because it had liquid electrodes and a solid electrolyte [Kummer 1972]. Although this was not a lithium based battery, it did prove that many ions could rapidly transport through solids, including lithium [Yao 1967]. This helped to spark interest in solid electrolytes. Other solid electrolytes would be developed that had faster lithium ionic conduction, such as Li_3N and $LiTi_2(PO_4)_3$ [Takada 2013].

Polyethylene oxide (PEO) is a polymer solid electrolyte that is a very popular. Polymer Solid electrolytes have the advantage of being flexible, easy to produce and many have good ion conductivity, 10^{-4} to 10^{-3} S cm^{-1} [Chatani 1987]. Polymer solid electrolytes have increased in ionic conductivity and generally have higher values than ceramic solid electrolytes. In 2003 Thangadurai and others developed a garnet structure as a fast ion conducting solid electrolyte [Thangadurai 2003]. This material had a nominal structure of $Li_5La_3M_2O_{12}$, where M= Nb or Ta. The solid electrolyte had an ionic conductivity comparable to other ceramic electrolytes of the time, but it was still fairly low, on the order of 10^{-6} S cm^{-1}, but it did have the advantage of being remarkably stable against lithium, it appeared to be unreactive even when placed against molten lithium [Thangadurai 2003].

Thangadurai and Weppner continued to work on the material and in 2007 they published another paper with a reformulated version of the material, $Li_7La_3M_2O_2$ [Murugan 2007]. This material met many of the criteria needed for a usable solid electrolyte: high

temperature stability, low cost materials, high mechanical properties, stability against lithium and negligible electronic conductivity [Murugan 2007]. The main advantage was its improved ionic conductivity over previous ceramic electrolytes. At room temperature the ionic conductivity was around 10^{-4} S cm^{-1} [Murugan 2007]. Work continues on these materials.

1.4.1 Lithium Lanthanum Zirconium Oxide (LLZO)

Further work would produce a new garnet material $Li_7La_3Zr_2O_{12}$ (LLZO) [Murugan 2007]. In the study, LLZO had a conductivity of approximately 6 X 10^{-6} S cm^{-1} at 27 ˚C, which was more than an order of magnitude better than $Li_5La_3Ta_2O_{12}$ [Murugan 2007]. This finding made LLZO the best ionic conductor of any $Li_5La_3M_2O_{12}$ garnet material that had yet been synthesized [Murugan 2007]. LLZO is made from relatively abundant materials that are environmentally benign and LLZO is chemically and thermally stable with most electrode materials; it is also relatively easy to prepare and densify [Murugan 2007]. One drawback is that when the LLZO is being processed, a different product may form, $La_2Zr_2O_7$ also known as pyrochlore, which has low conductivity and is sensitive to air [Murugan 2007]. Another challenge for LLZO is to form the right phase. Two phases exist for LLZO: tetragonal phase, which forms above 950 ˚C in pure LLZO and the more conductive cubic phase, which forms above 1230 ˚C in pure LLZO, but could form as low as 1180 ˚C [Awaka 2011].

Cubic phase has more than an order of magnitude higher conductivity than the tetragonal phase [Wolfenstine 2012a]. Meier and others investigated the ion conducting mechanisms in LLZO [Meier 2014]. Meier found that the tetragonal phase has all of its lithium sites fully occupied, in order to have lithium move through the electrolyte, many lithium ions must move together, all at once [Meier 2014]. For the cubic phase, there are many more free lithium sites in the LLZO electrolyte, and the motion of lithium ions is described as “single-ion

jumps", meaning the ions can move individually to vacant lithium sites, which requires much less energy [Meier 2014].

Several methods have been explored to generate and stabilize the cubic phase. Yttrium had been used as an additive which achieved a conductivity of more than 8 X 10^{-4} S cm^{-1} [Murugan 2011]. Geiger el at. [Geiger 2011] used specimens with Aluminum added to the LLZO material, because the addition of aluminum to LLZO may have occurred unintentionally in previous studies of LLZO. Geiger suspected that in the first experiments to synthesize LLZO as an electrolyte by Murugan and others [Murugan 2007], the aluminum oxide crucibles that were used added small amounts of aluminum to the LLZO. Regardless of intent, Aluminum addition to LLZO proved to be beneficial. Rangasamy et al. later explored the effects aluminum had on the phase [Rangasamy 2012]. They were able to process a cubic phase sample with composition of $Li_{6.24}La_3Zr_2Al_{0.24}O_{11.98}$, pressed at 40 MPa at a temperature of 1000 ˚C. at 98% density, the material had a conductivity of 4 X 10^{-4} S cm^{-1} [Rangasamy 2012]. The processing temperature Rangasamy used, 1000 ˚C, was much below the 1180 ˚C threshold observed by Awaka [Awaka 2011], and that was believed to be due to the Al additive.

To stabilize the cubic phase during calcination at 1000 ˚C, 0.204 moles of aluminum in the LLZO was required, but an excess of 0.389 moles could cause a side product, $LaAlO_3$, to form [Rangasamy 2012]. Furthermore, when the Al concentration was held constant at 0.24 moles, Li concentration between 5.63 and 6.24 moles would form cubic phase, but above that, the tetragonal phase would start to form [Rangasamy 2012].

To better understand the effects of Al substituted for Li in LLZO, Ga was used as the substitute instead, with a formula of $Li_{6.25}La_3Zr_2Ga_{0.25}O_{12}$ [Wolfenstine 2012a]. With Ga, the LLZO material that was hot pressed at 1000 ˚C and 40 MPa appeared to form the cubic phase.

The conductivity was 3.5 X 10^{-4} S cm^{-1} and the density was approximately 91%; compared to LLZO with Al substitution at a similar density, it had slightly better ionic conductivity [Wolfenstine 2012a]. It was proposed that the larger ions of Ga tend to occupy lithium sites that are less necessary for Li-conductivity, leaving Li-sites that are more involved in the lithium transport process to be left vacant [Wolfenstine 2012a].

LLZO can have some variety in its composition, such as Al and Ga substitution previously discussed. Substitutions can take the form $Li_{7-3x}M^{+3}{}_xLa_3Zr_2O_{12}$ where M^{+3} can be Al [Rangasamy 2012], Ga[Wolfenstine 2012a] or Fe[Rettenwander 2013]. All of these cations have a +3 charge and sit on a Li site [Thompson 2014]. To balance the charge, three Li ions must be expelled from the lattice creating two Li vacancies. Other substitutions can take the form $Li_{7-y}La_3Zr_{2-}yM^{+5}yO_{12}$ where M^{+5} can be Sb, Nb or Ta [Thompson 2014]. Because these ions have a higher charge than the Zr they are replacing (M^{5+} versus Zr^{4+}), it will be balanced by creating a Li vacancy. In either method of substitution, 0.4-0.5 Lithium vacancies per formula unit are required to stabilize the cubic structure in LLZO, which corresponds to $x\approx0.20$ for M^{3+}, direct substitution of lithium, and y=0.4-0.5 for M^{5+}, substitution of Zr [Thompson 2014]. To verify that x=0.4 was needed to stabilize the cubic phase, Thompson et al. tested specimens of the composition $Li_{6.75}La_3Zr_{1.75}Ta_{0.25}O_{12}$, which should not have enough vacancies to stabilize the cubic phase and would instead be in the tetragonal phase [Thompson 2014]. Thompson concluded that when there is not enough doping to create 0.4 to 0.5 Li vacancies, both cubic and tetragonal phases will form in the material [Thompson 2014].

For all the advances and breakthroughs that have come, there is still much work to be done and indeed interest and research continues to grow.

1.5 Forced Damped Harmonic Oscillation

In this study the elastic moduli will be determined from the resonant frequencies of disk or rectangular parallelepiped specimens. The concepts of resonance can be related to a forced damped harmonic oscillator. In order to discuss the forced damped harmonic oscillator, we shall first briefly overview the harmonic oscillator and the damped harmonic oscillator.

To help visualize the concepts, an example of a simple harmonic oscillator would be a pendulum in a vacuum. Only the force of gravity would be acting on this pendulum and there would be no loss to the surroundings. A real world example of a pendulum is a person on a swing which would be a damped harmonic oscillator because as the person swings, they are losing energy to friction forces such as wind resistance and the moving parts. If another person pushes the individual on the swing, the example now becomes a forced damped harmonic oscillator. Even though the person on the swing is losing energy, more energy is being put into the system by the person pushing.

The time it takes for a body in simple harmonic motion to complete one cycle or a single round trip is called the period [Halliday 1966]. The frequency is the inverse of the period, or how many cycles per unit time. The unit for frequency is cycles per second, or hertz (Hz).

1.5.1 Simple Harmonic Oscillator

A harmonic oscillator can be modeled as a spring-mass system. A perfect spring has no energy losses. When the mass-spring system of a perfect spring is displaced and then released, the mass undergoes simple harmonic motion. The potential energy can be described by Equation 1.5.01 [Halliday 1966]

$$U(x) = \frac{1}{2}kx^2 \qquad 1.5.01$$

where x is the displacement and k is a constant dependent upon the material. The force acting on a particle at any point can be described by

$$F = -dU/dx \qquad 1.5.02$$

Applying Equation 1.5.01 to Equation 1.5.02 it can be determined

$$F = -kx \qquad 1.5.03$$

This is also known as Hooke's law [Halliday 1966]. Applying Equation 1.5.03 to the well-known Newton's Second Law F=ma and substituting a with d^2x/dt^2 will yield

$$-kx = m\frac{d^2x}{dt^2}$$

or

$$\frac{d^2\mathrm{x}}{dt^2} = -\frac{k}{m}x \qquad 1.5.04$$

According to Halliday the value of x in this Equation must be a function "whose second derivative is the negative of the function itself" [Halliday 1966]. Cosine and sine functions have this property. Therefore the general solution to Equation 1.5.04 can be expressed as

$$\mathrm{x} = \mathrm{A}\cos(\omega t + \delta) \qquad 1.5.05$$

where A, ω and δ are constants. As a simple proof, take the second derivate of Equation 1.5.05

$$\frac{d^2\mathrm{x}}{dt^2} = -\omega^2\mathrm{A}\cos(\omega t + \delta) \qquad 1.5.06$$

apply Equation 1.5.05

$$\frac{d^2\mathrm{x}}{dt^2} = -\omega^2 x \qquad 1.5.07$$

dividing Equation 1.5.07 by Equation 1.5.04 gives

$$\frac{k}{m} = \omega^2 \qquad 1.5.07\ a$$

With the derivation and proof aside, the constants should be discussed. δ is the phase constant, which determines where the maximum is; for Equation 1.5.04, δ=0 and x=A at t=0 (see Figure 1.5.01). A is the amplitude of the motion and ω is the angular frequency [Halliday 1966].

From Halliday [Halliday 1966] The frequency, *v*, of the system is defined by the Equation

$$v = \frac{1}{2\pi}\sqrt{\frac{k}{m}}$$

which shows that the frequency of the spring is only dependent on the constant k and the mass. Thus the displacement of the mass vs time is represented by a cosine function as depicted in Figure 1.5.01.

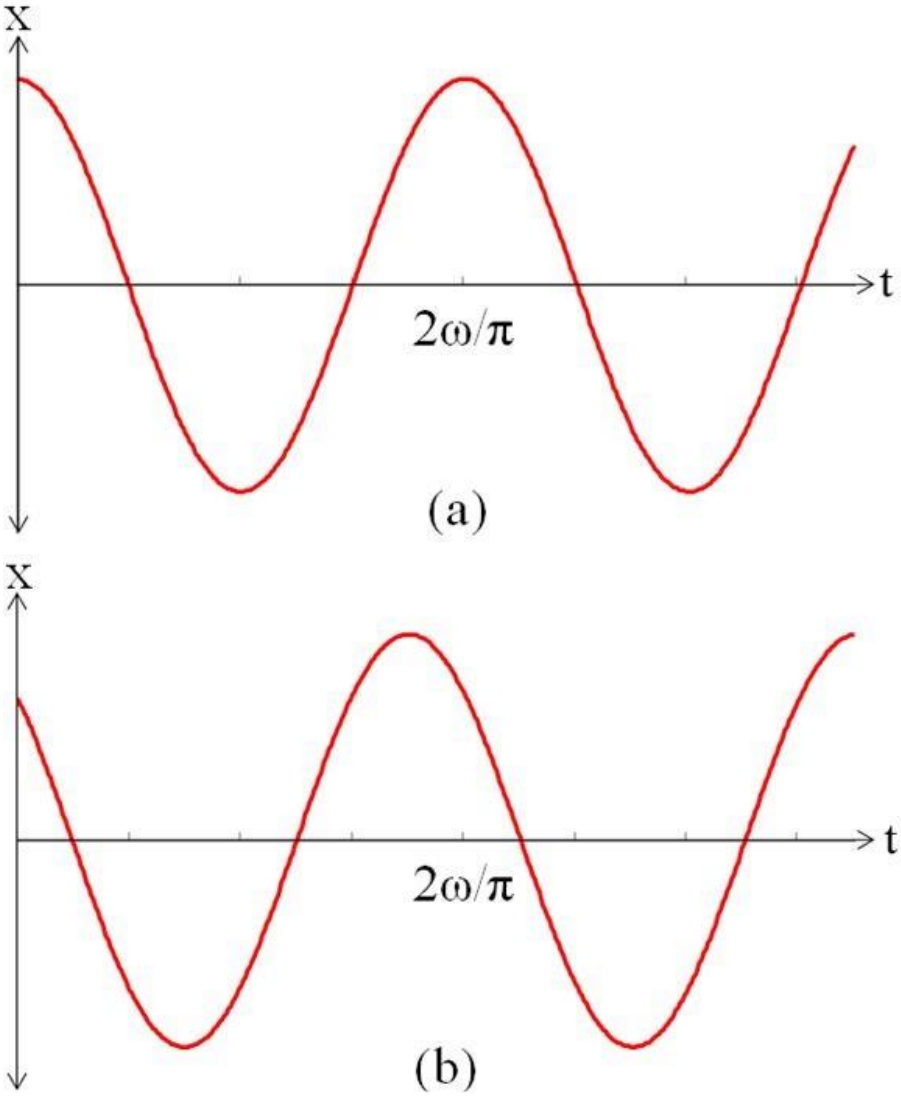

Figure 1.5.01 Displacement of an object with simple harmonic motion. (a) $\delta=0$ (b) same wave with a phase shift of $\delta=45^{o}$, both graphs have tick marks at $\omega/2\pi$ but for (a) every other tick mark is at a zero point and can't be seen

1.5.2 Damped Harmonic Oscillator

For the damped harmonic oscillator the spring does have energy loss so that the time versus displacement curve is different than for the harmonic oscillator [Ohanian 1985]. The damped harmonic oscillator is a cosine function with amplitude that decrease exponentially with increasing time as shown in Figure 1.5.02

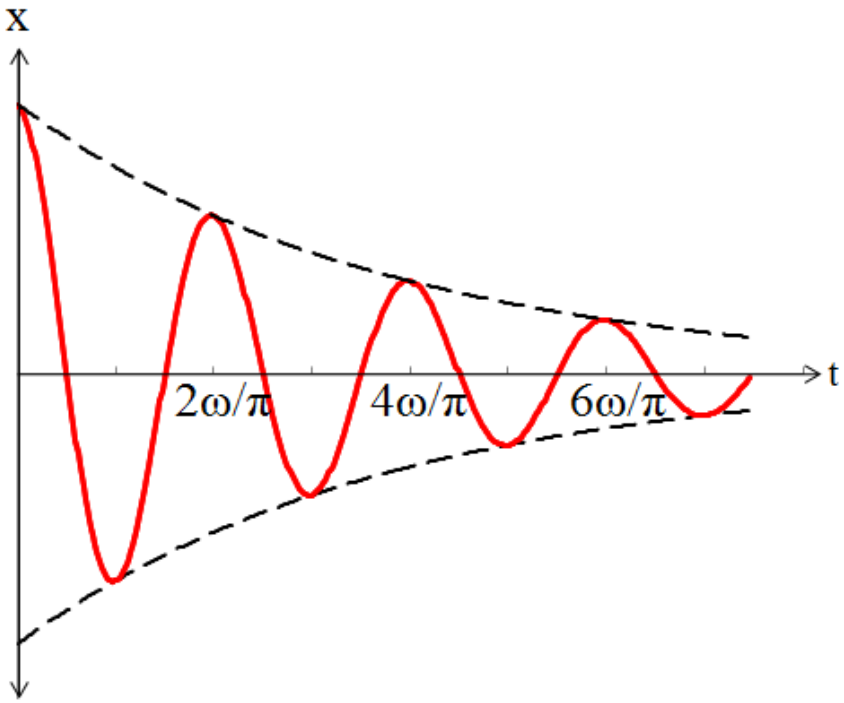

Figure 1.5.02 Damped harmonic motion plotted versus time according to Equation 1.5.15. Time is on the x axis and the displacement is on the y axis. The displacement experiences exponential decay and the maximum amplitude at any point can be expressed as $A(t)=A_o e^{-bt/2m}$

The expression for damped harmonic oscillators is similar to Equation 1.5.04, except there will be an additional term to represent energy loss

$$m\frac{d^2x}{dt^2} = -kx - b\frac{dx}{dt} \qquad 1.5.08$$

where b represents the friction force that is present.

In the case where b is larger than k/m, no oscillation takes place and x quickly goes to zero [Reddick 1955]. Therefore, it would be more beneficial to explore the scenario where b is small. To find the solution to Equation 1.5.08, the characteristic Equation should be considered [Hermann 2014]

$$mr^2 + br + k = 0 \qquad 1.5.09$$

where

$$r = -\frac{b}{2m} \pm \frac{\sqrt{b^2 - 4mk}}{2m}$$

or

$$r = -\frac{b}{2m} \pm i\sqrt{\frac{k}{m} - \left(\frac{b}{2m}\right)^2} \equiv \alpha \pm i\beta \qquad 1.5.10$$

Evidently, some of the roots of this characteristic Equation are imaginary. α and β can be defined as

1.5.11 $$\alpha = -\frac{\mathrm{b}}{2\mathrm{m}}$$ $$\beta = \sqrt{\frac{k}{m} - \left(\frac{b}{2m}\right)^2} = \omega' \qquad 1.5.12$$

Note that when b equals zero, ω' is simply ω. According to Tenenbaum [Tenenbaum 1985] second order, homogeneous differential Equations whose roots follow the form $\alpha \pm i\beta$, will have the general solution

$$\mathrm{x} = \mathrm{ce}^{\alpha \mathrm{t}} \cos(\beta \mathrm{t} + \delta) \qquad 1.5.13$$

where δ is an angle or the phase constant. Substituting 1.5.11 and 1.5.12 into 1.5.13 gives

$$\mathrm{x} = \mathrm{ce}^{-\frac{\mathrm{bt}}{2\mathrm{m}}} \cos(\omega' \mathrm{t} + \delta) \qquad 1.5.14$$

where c is a constant. Figure 1.5.02 shows the value of x will be the highest at the initial amplitude, A_0, at t=0 if there is no phase shift (δ=0). Applying these conditions to 1.5.14, the constant c is shown to be A_0. And the solution is

$$\mathrm{x} = A_0 \mathrm{e}^{-\mathrm{bt}/2\mathrm{m}} \cos(\omega' \mathrm{t} + \delta) \qquad 1.5.15$$

It is important to note that ω' is slightly smaller than ω. Using ω instead of ω' to simplify the Equation will introduce little error, and for simple calculations this is acceptable [Ohanian 1985], but for maximum accuracy it is included here. A more detailed explanation

and following proofs can be found in Tenenbaum and other sources [Tenenbaum 1985; Reddick 1955; Halliday 1966; Ohanian 1985; Hermann 2014].

1.5.3 Forced Damped Harmonic Oscillator

When energy is added at constant intervals to a damped harmonic oscillator system, it becomes a forced damped harmonic oscillator. In the case of harmonic oscillators and damped harmonic oscillators, the period is based on the natural oscillations of the system [Ohanian 1985]. But for a forced damped harmonic oscillator, the period is dependent on the force being applied. Take for example a person on a swing. If they "pump" their legs at the same period as the oscillation of the swing, they can increase how high they swing, or the amplitude, this is called resonance [Ohanian 1985]. However if the person swinging were to "pump" out of phase as the swing or at a different frequency as the swing, it could cause the swing to not swing as high. The displacement will reach a maximum when the drive frequency is equal to the resonant frequency. To find the displacement, start with Equation 1.5.08 and add a new term for the driving frequency [Halliday 1966]

$$m\frac{d^2\mathrm{x}}{dt^2} = -b\frac{dx}{dt} - kx + F_m\cos(\omega'' t))$$

or

$$m\frac{d^2\mathrm{x}}{dt^2} + b\frac{dx}{dt} + kx = F_m\cos(\omega'' t) \qquad 1.5.16$$

where m is the mass, F_m is the maximum force of the driver, ω'' is the frequency of the driver with units of 1/time, b is the term for dampening with units of mass/time, $^{d^2\mathrm{x}}/_{dt^2}$ is acceleration, $^{\mathrm{dx}}/_{dt}$ is velocity and t is time [Halliday 1966].

Equation 1.5.16 is a nonhomogeneous second order differential Equation, therefore the solution can be found using the method of undetermined coefficients [Tenenbaum 1985]. The general solution will be the sum of the characteristic solution, x_c, and a particular solution, x_p. The solution to the characteristic Equation can be determined as though it were a homogeneous Equation and will be similar to Equation 1.5.15

$$x_c = A_0 e^{-bt/2m} \cos(\omega'' t + \delta) \quad 1.5.17$$

Then the particular solution can be found from the right side of Equation 1.5.16.which will be a combination of all of its linearly independ derivatives: cos(ω''t) and sin(ω''t). In this case, F_m is a constant and can be ignored

$$x_p = A \sin(\omega'' t) + B \cos(\omega'' t) \quad 1.5.18$$

To continue the method of undetermined coefficients xp' and xp'' need to be determined

$$\frac{dx_p}{dt} = \omega'' A \cos(\omega'' t) - \omega'' B \sin(\omega'' t) \quad 1.5.19$$

and

$$\frac{d^2 x_p}{dt^2} = -\omega''^2 A \sin(\omega'' t) - \omega''^2 B \cos(\omega'' t) \quad 1.5.20$$

From here Equations 1.5.18, 1.5.19 and 1.5.20 would be inserted into the original Equation 1.5.16 to solve for the A and B variables and get an unambiguous Equation for x_p. Then the solution to x would simply be x_c plus x_p. The algebra for this is somewhat rigorous and can be found in Reddick [Reddick 1955]. For brevity sake, we will skip to the solution

$$x = \frac{F_m}{G} \sin(\omega'' t - \delta) \quad 1.5.21$$

where

$$G = \sqrt{m^2(\omega''^2 - \omega^2)^2 + b^2\omega''^2} \qquad 1.5.22$$

and

$$\delta = \cos^{-1}\left(\frac{b\omega''}{G}\right) \qquad 1.5.23$$

In Equation 1.5.21, x is a distance with units of length, and because the value of the sin term is unitless, the F_m/G term also has units of length. In Equation 1.5.21 it is evident that the system's vibration is determined by the frequency of the driving force ω'' and not the natural frequency ω. From Equation 1.5.22 it can be seen that as ω'' approaches ω, G becomes much smaller and x, the amplitude, rises exponentially. The driving frequency that causes the maximum amplitude is called the resonance frequency. As shown in Figure 1.5.04, as the value of b gets smaller, the resonant frequency approaches the natural frequency. In Equation 1.5.22, if b=0 the resonance frequency will be equal to the natural frequency, ω. For the simple spring mass driver model of the forced damped harmonic oscillator, there is a single mass on a spring and one driver, so there would be one resonant frequency. However for bulk solids have a number of resonant frequencies. Figure 1.5.03 shows the effects different driving frequencies have on a curve. Figure 1.5.04 shows the effects of friction on maximum amplitude.

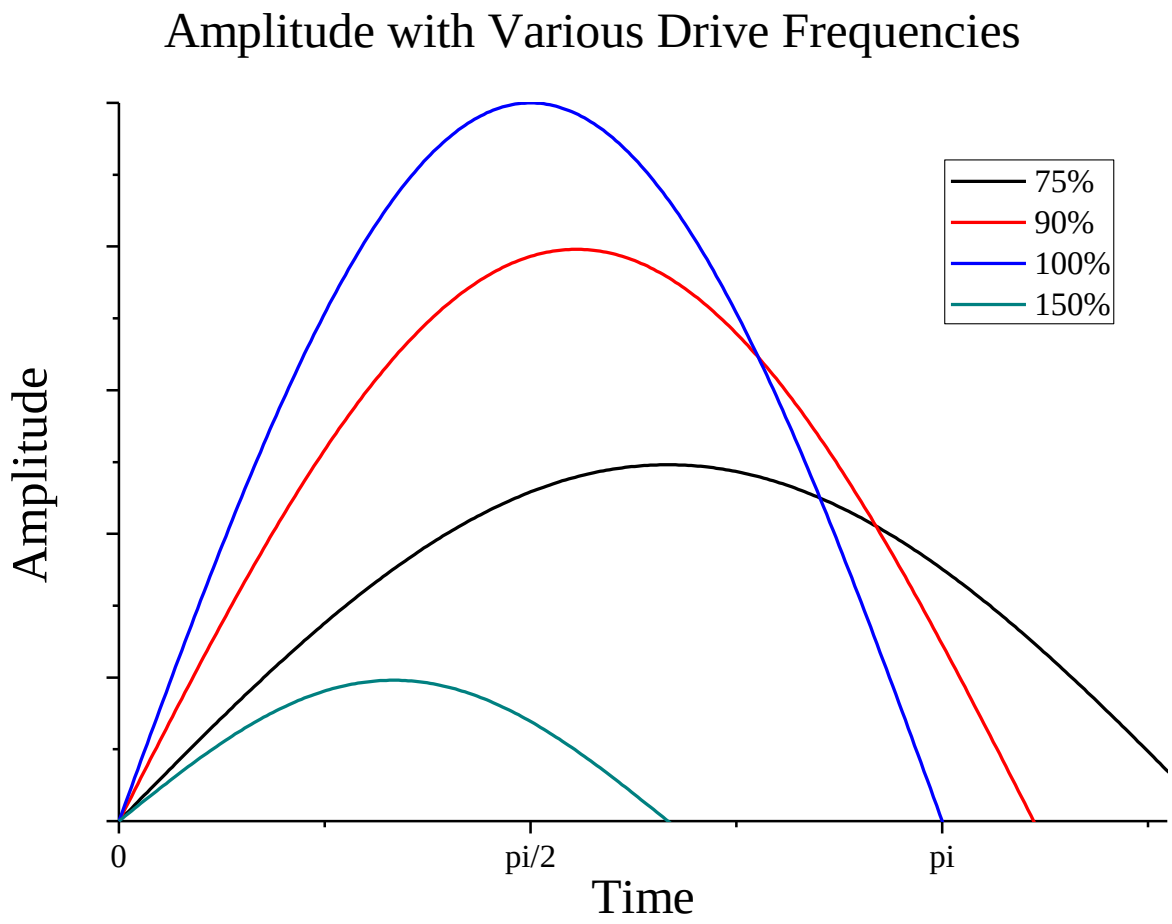

Figure 1.5.03 Amplitude with various drive frequencies assuming no dampening. The percentage represents the drive frequency over the natural frequency, ω’’/ω. The value of x on the y-axis is arbitrary and will change based on the mass of an object and the other variables of Equations 1.5.21 through 1.5.23. For clarity the dampening is set to 0 so they will originate at the same point and be easier to compare. The important matter to note is that as driving frequency approaches the natural frequency, the amplitude reaches a maximum. Equation 1.5.21 shows the systems vibrations are dependent on the drive frequency, and that is also shown here that the frequency of each curve is different and is dependent on the drive frequency.

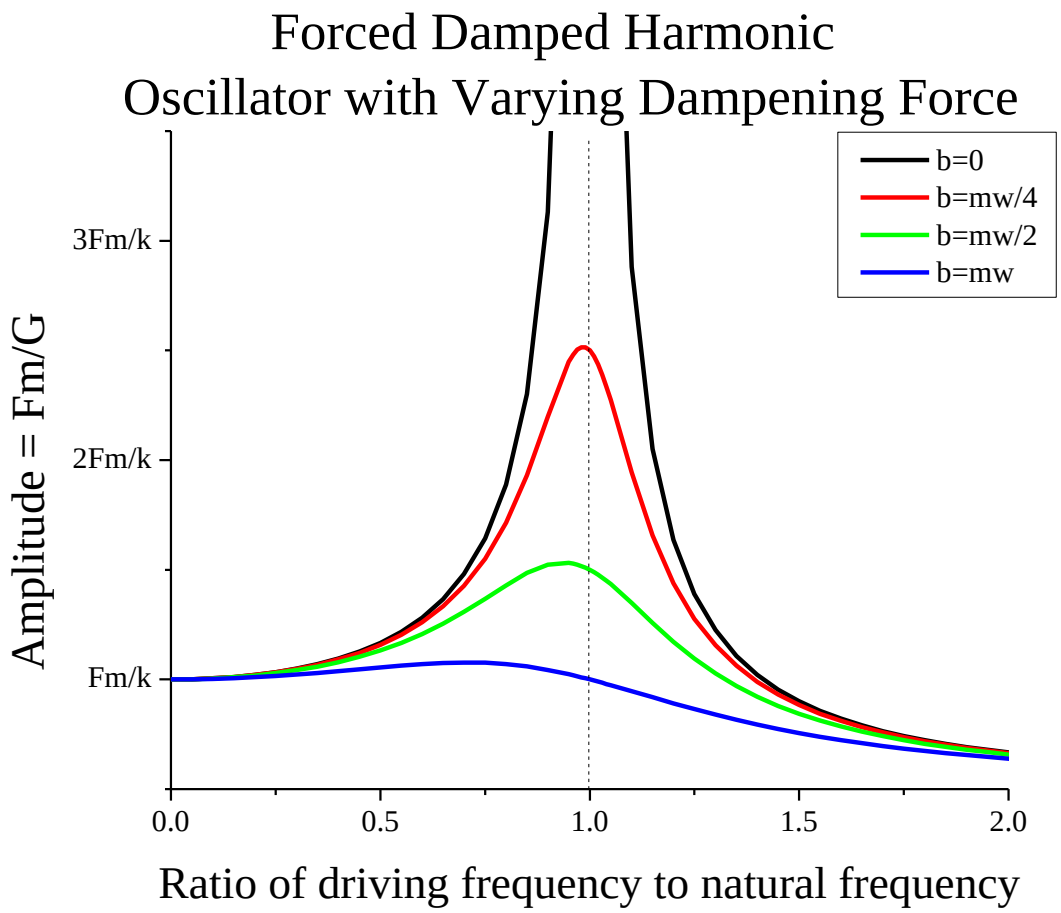

Figure 1.5.04 A diagram of the amplitude with changing friction force based on Halliday [Halliday 1966]. Maximum amplitude is on the y-axis and ω''/ω is on the x-axis. Notice when there is no friction the amplitude approaches infinity. As b increases, the maximum amplitude and the resonance frequency moves to the left.

In this study the resonant ultrasound spectroscopy (RUS) system uses a transducer to send a sine wave through the material. The frequency of the transducer will increase and find several frequencies that resonate. The resistance within the material will damp the wave. It also acts as a forced damped harmonic oscillator by continuing to input energy to maintain the wave. As the damping increases, the amplitude of the peak decreases. If the material is not entirely homogeneous (such as a change in density or change in material phase) it will resonate with less intensity and over a wider range of frequencies causing the peak to broaden, or increases in width [Leisure 2004]. This is called internal friction. There are other sources of

internal friction such as point defects and [Ogi 2006]. RUS be discussed further in later sections, but it is important to understand that the system acts as a forced damped harmonic oscillator.

1.6 Mechanical Properties

How stress affects a material is determined by its mechanical properties. Mechanical properties are inherent material properties that do not change based on the size of the specimen. However, Specimens with the same chemical composition can have drastically different mechanical properties. Many factors determine the mechanical properties of a particular specimen including processing methods, temperature and defects.

RUS is often used to measure mechanical properties such as Young's modulus, E, shear modulus, G, and Poisson's ratio, ν. Hooke's law states the stress is proportionate to the strain [Popplewell 1907]. Accordingly, Young's modulus can be defined by Hooke's law

$$\mathrm{E} = \frac{\sigma}{\epsilon} \qquad 1.6.01$$

where σ is stress and ϵ is strain [Kingery 1976a] (this is an alternative form of Hooke's Law as stated in Equation 1.5.03).

Being that the strain is unitless, the Young's modulus will have the same units as the stress, namely Pascal (Pa), often on the order of GPa for metals and ceramics. The shear modulus can be expressed in a similar way [Kingery 1976a]

$$\mathrm{G} = \frac{\tau}{\gamma} \qquad 1.6.02$$

where G is the shear stress, τ is shear stress and γ is shear strain [Kingery 1976a].

Shear modulus for metals and ceramics can also have units of GPa, though of less magnitude than the Young's modulus. Porosity will decrease a materials modulus value. Higher

porosity will mean more empty space in a cross sectional area, which in turn means less material to bear the stress, leading to a lower modulus value (this will be further discussed in section 3.2.1).

Poisson's ration, ν, can be defined by Equation 1.6.03 [Kingery 1976a]

$$\nu = \frac{\Delta d/d}{\Delta l/l} \qquad 1.6.03$$

where d is thickness and l is length.

This is the ratio of the thickness decrease to length increase. For elastic deformation, values typically range from 0.2 to 0.3 for ceramics [Kingery 1976a]. Poisson's ratio can be related to Young's modulus and shear modulus by the formula [Kingery 1976a]

$$\nu = \frac{E}{2G} - 1 \qquad 1.6.04$$

A single crystal may have directional dependent values for E and G based on the orientation of the crystal. In graphite, for example, when the stress is parallel to the graphene sheets, they have high modulus values; but when the stress is perpendicular to the sheets, the sheets can be pulled apart with little resistance resulting in a low modulus. In the same way as graphite, any material, such as a composite material or a layered material, that has a different structure in a different directions will also have different modulus values in the various directions.

1.6.1 Young's Modulus of Solid Solutions as a Function of Composition

As a crystal forms it may be exposed to a different type of atom than the ones that forms its structure. If incorporating the secondary atom into the existing structure raises the energy, the crystal will reject it or be unstable [Kingery 1976b]. But if incorporating the atom into the crystal lowers the energy, it will be added to the [Kingery 1976b]. If more of the secondary

atoms are added, the crystal may change into a more order structure, or form two separate crystals, the intermediate phase is called a solid solution [Kingery 1976b]. Perhaps the most important characteristic of a solid solution is that the material will have a range of secondary atoms it can absorb. It can be less than 1% like in the case $CaCl_2$ or form a complete solid solution over the entire range of composition such as the case of Si and Ge. When both materials are completely soluble over the entire range of composition it is known as complete solid solubility [Barsoum 1997b].

A substitutional solid solution is when the atom of one material replaces an atom of the host structure, this is common in ceramics [Kingery 1976b]. Several factors determine whether or not an atom can form a substitutional solid solution with another material including; size factor, valance charge, chemical affinity and structure type [Kingery 1976b].

Another type of solid solution is the interstitial solid solution. Rather than the atoms substituting in place of one of the host ions, the smaller added atoms sit on the interstitial sites between the host atoms. This is most common with metallic bonds who then incorporate H, C, N or B into interstitial sites [Kingery 1976b]. Solid Solutions will be discussed further in section 3.2.5

1.6.2 Young's Modulus of a Fiber Matrix Composite

Another type of material that may explain lithium deposition in LLZO is a composite that contains fibers. Lithium-ion flux in a battery can cause dendrites to grow into the solid electrolyte, in a form that resembles fibers [Dollé 2002; Rosso 2006]. This could change the elastic moduli of the material. Kingery presents several models to analyze how changes in composition can affect the elastic moduli [Kingery 1976a].

The simplest method to estimate the Young's modulus in a composite material is the rule of mixtures (ROM) and inverse rule of mixtures (IROM) for the upper and lower bounds, respectively [Islam 2011]

$$E_{CU} = V_m E_m + V_r E_r \quad \text{(Rule of mixtures)} \qquad 1.6.05$$

and

$$\frac{1}{E_{CL}} = \frac{V_m}{E_m} + \frac{V_r}{E_r} \quad \text{(Inverse Rule of mixtures)} \qquad 1.6.06$$

E_{CU} = Upper estimate for Young's modulus of the composite material, E_{CL} = Lower estimate for Young's modulus of the composite material, V_m = Volume of matrix, E_m = Young's modulus of matrix, V_r = Volume of reinforcement, E_r = Young's modulus of reinforcement [Kingery 1976a].

The ROM model estimates the upper bound and assumes the fibers, or layers, are aligned in the direction of the stress [Kingery 1976a]. The IROM model sets the lower bound and assumes the two phases, as layers or fibers, are perpendicular to the applied stress [Kingery 1976a]. The ROM and IROM and also known as the Voigt and Ruess models, respectively. The bounds set by these models are rather wide. Hashin and Shtrikman determined Equations with narrower bounds which did not require any particular geometry for the phases, so it could be more widely used [Kingery 1976a]. The Equations, where $K_2 > K_1$ and where $G_2 > G_1$, are

$$K_{CL} = K_1 + \frac{V_2}{\frac{1}{K_2 - K_1} + \frac{3V_1}{(3K_1 + 4G_1)}} \qquad 1.6.07$$

$$K_{CU} = K_1 + \frac{V_1}{\frac{1}{K_1 - K_2} + \frac{3V_2}{(3K_2 + 4G_2)}} \qquad 1.6.08$$

$$G_{CL} = G_1 + \frac{V_2}{\frac{1}{G_2 - G_1} + \frac{6V_1(K_1 + 2G_1)}{5G_1(3K_1 + 4G_1)}} \quad 1.6.09$$

$$G_{CU} = G_2 + \frac{V_1}{\frac{1}{G_1 - G_2} + \frac{6V_2(K_2 + 2G_2)}{5G_2(3K_2 + 4G_2)}} \quad 1.6.10$$

K = bulk modulus, G= shear modulus, V = Volume fraction. In Equation 1.6.07 through 1.6.10, the subscripts 1 and 2 refer to the two materials, where the stronger material is labeled 2. Bounds for the Young's modulus using the bounds from the Hashin Shtrikman Equations inserted into the relation

$$E = \frac{4KG}{3K + G} \quad 1.6.11$$

An application of the ROM and IROM as well as other fiber/matrix composite models will be utilized and discussed further in section 3.2.2.

1.6.3 Effects of microcracking on Young's modulus

Microcracks are small cracks that cannot typically be seen by then naked eye and have a detrimental effect on elastic moduli [Case 1993]. Microcrack can occur during polishing, during machine operations, due to temperature change or accidental damage to the surface [Barsoum 1997c]. Microcracks can be induced by small abrasive particles, like the sanding medium, which can mimic a "sliding indentation" creating a crack on the specimen surface. Microcracking can also be correlated to temperature. Microcracking is unavoidable when the material is cooled below a critical microcrack initiation temperature [Zimmermann 2001; Case 1980]. One major cause can be buildup of stress at grain boundaries during temperature change due to a mismatch in thermal expansion coefficient [Barsoum 1997c]. The critical microcrack

initiation temperature can be defined by Equation 1.6.12 [Case 1980]

$$T_{MI} = \frac{-14.4\gamma_f}{E * \Delta\alpha_{max}^2} * \left(\frac{1}{g_s}\right)^{1/2} + T_0 \qquad 1.6.12$$

Where T_{MI} is the temperature at which microcracks will begin to initiate upon cooling to (or below) this temperature , g_s is grain size, γ_f is the fracture energy, E is the Young's modulus, $\Delta\alpha_{max}$ is the maximum change in thermal expansion coefficient over the given temperature range and T_0 is temperature at which the internal stresses are no longer relieved [Case 1980].

Equation 1.6.12 shows the microcrack initiation temperature is a function of fracture toughness, thermal expansion, grain size, and the total temperature change.

The extent to which the microcracks affect the elastic modulus properties is dependent upon microcrack number density, orientation geometry and the size of the microcrack [Case 1993]. Models are available to characterize the effects that microcracking has on a material, as discussed by Case and Kim [Case 1993; Kim 1993a; Kim 1993b]. The material was modeled as a layered composite, where microcracks exist to a certain depth, but below this layer is an unaltered, crack free region [Case 1993]. In a layer with microcracks, assuming homogeneous distribution of the cracks, the change in Young's modulus can be expressed by Equation 1.6.13 [Case 1993]

$$\frac{E_0 - E}{E_0} = fGN_v \qquad 1.6.13$$

where E_0 is the Young's modulus of the material with no microcracks, E is the Young's modulus of the material with microcracking, f is a function of the spatial orientation of the microcracks, N_v is the number of cracks per unit volume and G represents the crack geometry which can be represented by the Equation

$$G = \frac{2}{\pi}\frac{< A^2 >}{< p >} \qquad 1.6.14$$

where A and p are the area and perimeter of the microcrack respectively [Case 1993].

Equation 1.6.13 is applicable for a single layer or a material with homogenous microcrack distribution, but the Equation is inadequate for a material where the crack is limited to a surface layer and a crack free layer exists. To predict the modulus of a multilayer of material, Case and Kim [Case 1993]use a modified rule of mixtures (ROM) Equation

$$E_{2ROM} = V_l E_l + V_m E_m \quad 1.6.15$$

where E_{2ROM} is the rule of mixtures for a material with 2 layers, a microcrack damaged layer and a microcrack free layer V_l and V_m are the volume fraction of the microcrack layer and the microcrack free layer, respectively, and E_l and E_m are the Young's modulus of the microcrack layer and the microcrack free layer, respectively [Case 1993].

If there are cracks on both sides of the material it can be viewed as a 3 layered material with a similar application of the ROM [Case 1993]

$$E_{3ROM} = V_{l1} E_{l1} + V_m E_m + V_{l2} E_{l2} \quad 1.6.16$$

where $l1$ and $l2$ represent layer 1 and layer 2 respectively.

Equation 1.6.15 and 1.6.16 can be combined with Equation 1.6.13 to get Equation 1.6.17 and Equation 1.6.18 to get a general expression for changes due to the microcrack containing layers [Case 1993]

$$\frac{E_m - E_{2ROM}}{E_m} = f G_l N_l V_l = f G_l N_v \quad 1.6.17$$

and

$$\frac{E_m - E_{3ROM}}{E_m} = f_{l1} G_{l1} N_{v1} V_{l1} + f_{l2} G_{l2} N_{v2} V_{l2} \quad 1.6.18$$

(for a more detailed derivation see Case and Kim [Case 1993])

In the 3 layer model Equation 1.6.18, if the two layers microcrack containing layers have the same cracks size, shape, orientation, geometry and number density, then Equation 1.6.18 reduces to Equation 1.6.17. With some understanding of the geometry of the cracks, *f* and G_l can be calculated using the Equations in Table 1.6.01.

Table 1.6.01 expressions for *f*, *G* and ε depending on alignment and crack geometry [Kim 1993a]

Crack geometry	***f*(ν₀)**	***G***	**ε**	**Orientation**
Penny	$16 * (1 - \nu_0^2)/3$	$\pi a^3/2$	$N\langle a^3\rangle$	Aligned
	$16 * \frac{(1 - \nu_0^2 * (10 - \nu_0)}{45(2 - \nu_0)}$			Random
Half Penny	$16 * (1 - \nu_0^2)/3$	$\pi a^3/4$	$0.5N\langle a^3\rangle$	Aligned
	$16 * \frac{(1 - \nu_0^2 * (10 - \nu_0)}{45(2 - \nu_0)}$			Random
Slit	$\pi_0^2 * (1 - \nu_0^2)/2$	$2c^2l^2/(c+l)$	$4N\langle c^2l^2\rangle/(\pi(c+l))$	Aligned
	$\pi_0^2 * \frac{(1 - \nu_0)(5 - 4\nu_0)}{30}$			Random
Ellipse	$16 * (1 - \nu_0^2)/3$	$\pi^2bd^2/4E(k)$	$N\pi\langle bd^2\rangle/2E(k)$	Aligned
	$16 * \frac{(1 - \nu_0^2 * (10 - \nu_0)}{45(2 - \nu_0)}$			Random
Half-Ellipse	$16 * (1 - \nu_0^2)/3$	$\pi^2bd^2/8E(k)$	$N\pi\langle bd^2\rangle/4E(k)$	Aligned
	$16 * \frac{(1 - \nu_0^2 * (10 - \nu_0)}{45(2 - \nu_0)}$			Random

ν_0 is the Poisson's ratio of the microcrack free layer, $\langle a \rangle$ is average radius of crack, c is half of average crack size for slit, l is the depth of the slit crack, b is half of the major axis of crack, d is half of the minor axis for the crack and E(k) is the complete elliptical integral of the second kind where $k = (b^2-d^2)^{1/2}/2$

A plot of $(E_0-E)/E_0$ versus N_v would be a straight line with a slope, S_n, which is defined as the product of the crack orientation, *f*, and crack geometry, *G*. S_n can be defined by the Equation 1.6.19 [Fan 2012]

$$S_n = f\frac{2 < A^2 >}{\pi < p >} \qquad 1.6.19$$

which can then be used in Equation 1.6.13 to get Equation 1.6.20 [Kim 1993b]

$$\frac{E_0 - E}{E_0} = S_n * N \qquad 1.6.20$$

Equation 1.6.20 applies to both 2 and 3 layer specimens if the outside layers of the 3 layer specimen have the same thickness, orientation and geometry [Kim 1993a]. Equations for S_n can be found from Table 1.6.02 [Fan 2012]

Table 1.6.02 Equations for S_n based on crack geometry where ν is the Poisson's ratio, c is the idealized crack depth and a is half of the indentation mark diagonal length [Fan 2012]

Model	Equation
Unmodified slit geometry	$S_n = \pi^2 \frac{(1 - v_0^2)}{2} \frac{2(2c^2)^2}{4\pi c}$
Modified slit crack geometry	$S_n = \pi^2 \frac{(1 - v_0^2)}{2} \frac{2(2c^2 - \pi a^2/2)^2}{\pi(4c + \pi a)}$
Unmodified half ellipse crack geometry	$S_n = 16 \frac{(1 - v_0^2)}{3} \frac{2(\pi c^2/2)^2}{\pi^2 c}$
modified half ellipse crack geometry	$S_n = 16 \frac{(1 - v_0^2)}{3} \frac{2(\pi c^2/2 - \pi a^2/2)^2}{\pi(\pi c + \pi a)}$

To help understand Table 1.6.02, Figure 1.6.01 shows where c and a would be measured on a crack and what each crack is labeled. Based on figures from Kim and Case and Fan [Kim 1993a; Fan 2012].

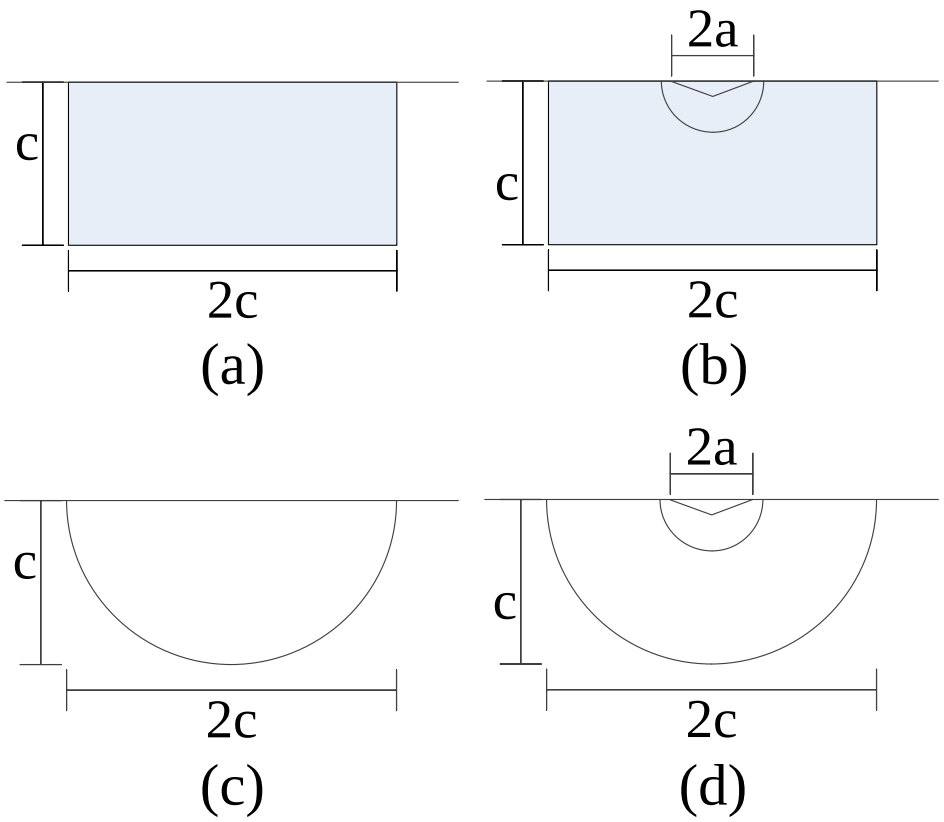

Figure 1.6.01 Various cracks, (a) is a slit crack (b) is a modified slit crack geometry with the mark from an indentation, (c) is a half ellipse geometry and (d) is a modified half ellipse geometry. Lengths a and c for the Equations in Table 1.6.02 are shown in each figure [Kim 1993a; Fan 2012]

Similar to Equation 1.6.20 is Equation 1.6.21 which can to find a change in Poisson's ratio [Fan 2012]

$$\frac{v_0 - v}{v_0} = S_v * N \qquad 1.6.21$$

where ν is the Poisson's ratio of the specimen with microcracks, ν_0 is the Poisson's ratio of a specimen free of microcracks. S_v can be defined as $4\pi c^3/3$ [Walsh 1965] for randomly aligned microcracks.

Using Table 1.6.01 and Table 1.6.02, as well as Equations 1.6.13 to 1.6.21, require very fine measurements and can become quite tedious. Furthermore, the flat face has a biaxial stress state and the bulk material has a triaxial stress state, this would make it more difficult to get a

reliable number for N_v [Fan 2012]. A predicted S value, S_p, can be used in 1.6.20, which is easier to measure and doesn't require detailed measurements of the cracks. S_p can be found from Equation 1.6.22

$$S_p = \frac{r^2 + 3}{(r+1)^2} \frac{r}{(2+1)} f \qquad 1.6.22$$

where r is the depth of the microcrack layer divided by the depth of the microcrack free layer.

Microcracking can influence the elastic moduli values of a material. The effects of microcracking on LLZO specimens in this study are discussed in section 3.2.4.

2.0 Experimental Procedure

The experimental procedure consisted of several different processes. The LLZO material was fabricated by Professor Sakamoto's group. In this project, specimens were prepared for analysis by resonant ultrasound spectroscopy (RUS) by various means. RUS was used to determine the elastic moduli of the specimens.

2.1 Labels

The First two specimens in table are from previously published work [Ni 2012].The rest of the specimens that were analyzed in this study have the same labeling format. The first letter stands for the Professor's lab where the specimen was made. The second group of letters is the abbreviated name of the material. The group of numbers indicates the date that the specimen was received. Any specimens that share these first three parts of the label are cut from the same billet. The last character is either the letter or number that designates individual specimens cut from a single original billet. For example:

Table 2.1.1 Explanation of the specimen labels used in this report

S-LLZO-71014-A			
S	LLZO	71014	A
Lab where specimen was made: Dr. Sakamoto's Lab	specimen material: Lithium Lanthanum Zirconium Oxide	date the specimen was received: 7/10/14	Individual specimen label

Additionally some specimens were analyzed more than once after, typically after some reprocessing. Therefore the specimen has an additional designation in their label such as "Pre-sanding" or "Post Sanding". The reprocessing, such as cutting a cylinder into a rectangular parallelepiped or sanding a specimen, typically improved the RUS analysis result. If a label for

reprocessing is not listed on the specimen, it is the latest results from that specimen; and prior, less accurate results are not included or do not exist.

2.2 Specimen Preparation

Samples need to be made into specimens that could be analyzed with a resonant ultrasound spectroscopy RUS. For most of the samples in this project, a billet received from Dr. Sakamoto's group was cut it into disks one to two millimeters thick. Some of these samples were sanded. Some samples were cut into rectangular parallelepipeds. All samples were scanned using the RUS analysis. The RUS data was then analyzed using commercial software to determine the elastic moduli.

2.2.1 Cutting

2.2.1.1 Cutting Sample Billet into Several Specimens

The billet was placed on a glass slide to prepare it for cutting. The slide and the sample were slowly heated on a hot plate to prevent thermal shock, which may produce cracking. The sample was affixed to the glass slide with enough thermal plastic to cover most of the edges in order to prevent chipping during the cutting, see Figure 2.2.1. The heat setting on the hot plate was adjusted so that the hotplate was typically just hot enough to soften the thermoplastic, but not hot enough to liquefy the thermoplastic.

Figure 2.2.1 The LLZO billet being prepared for cutting. The left image shows the billet being affixed to a glass slide with thermoplastic covering more than half of the specimen to prevent chipping. Some minor chipping can be seen, as that was how the specimen was received. The image on the right shows the glass slide mounted to the cutting arm of the slow speed diamond saw. A cut that had been started can be seen on the left side of the billet.

The cuts of the as received billet were made using the low speed diamond blade saw (Isomet Low Speed Saw, Buehler, Evanston, IL) at a speed setting between 2 and 4. The micrometer mounted on the Buehler saw was used to move the cutting sample to ensure opposite faces of the disks would be parallel. The next cut was also made at a setting between 2 and 4. Most individual cuts took from 15 to 45 minutes, depending on the rotations per minute of the saw blade, the mass of the counter weight and the hardness of sample. After the cutting was complete the specimens were removed from the thermoplastic by heating on the hot plate. Again, the specimen was heated just enough to make the thermoplastic pliable, but not hot

enough to liquefy it which allowed the pieces of thermoplastic to be removed from the specimen in complete sections and minimized the thermoplastic melting to the surface of the specimen. The specimens were then washed with acetone to remove remaining residual thermoplastic. In the early stages of this project, the acetone was applied directly to the sample, but this was changed. Acetone was applied to Kim wipes and the samples were wiped repeatedly until no visible signs of thermoplastic remained. The resulting specimens were cylindrical disks.

2.2.1.2 Cutting Rectangular Parallelepipeds

Cutting the rectangular parallelepiped follows a similar procedure with some modification. The specimen to be cut into a parallelepiped initially was cylindrical disk. The disk was mounted to a glass slide and then the glass slide was mounted to an aluminum block. The glass slide was placed between the sample and the aluminum block to prevent the saw blade from cutting into the aluminum mounting block.

The block was mounted to the low speed diamond blade saw (Isomet Low Speed Saw, Buehler, Evanston, IL) at two points 90^{o} away from each other, that is to say, on adjacent faces of the block which allows the block and samples to be rotated so the cuts in the specimen are oriented at 90^{o} from one another (see Figure 2.2.2).

When cutting a parallelepiped, the blade needs to cut deep into the glass so the curved blade can cut through the flat material. Another reason for cutting deep into the glass slide is that the blade has a beveled edge. So in order to not have any sort of ridge at the edge of the specimen, the blade needs to cut sufficiently through the sample.

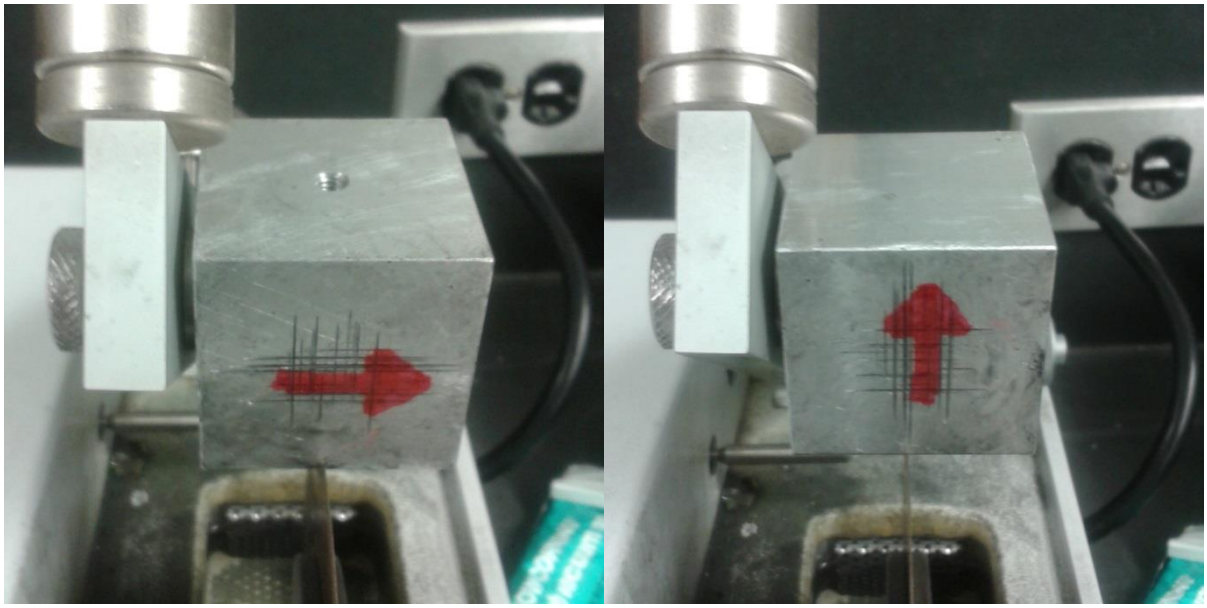

Figure 2.2.2 Notice the screw hole on the top side of the block in the left picture. In the picture on the right, the block is remounted to the saw using that screw hole. In doing so, the arrow will be rotated exactly 90^{o}, so the cuts will be at exactly 90^{o} to one another.

2.2.2 Sanding

Some of the cylinder samples were sanded. In some cases reducing the specimen thickness improved the RUS scan. In other cases, sanding was needed because the low speed diamond saw cut was not made adequately parallel to the existing surface. By sanding one face of the specimen, the change in thickness across the specimen would be reduced. Different methods of sanding were used as the study progressed.

At the beginning of the study, the specimens to be sanded were placed between two glass microscope slides that were affixed to a smooth aluminum plate, see Figure 2.2.3. Initially the specimens were secured in place using thermoplastic, enough to reach the thickness of the glass slides but not to the top of the specimens. This way the thermoplastic would not be sanded needlessly, until the sanding is nearly complete. After a few trials, the specimens were taped down with double sided tape instead of using thermoplastic to glue them down between the glass slides, see Figure 2.2.3. After the specimen was sanded to a uniform thickness, the

specimen would be removed from the tape. The specimen was then lightly sanded on the side that contacted the tape to remove any adhesive residue. Using double sided tape avoided applying a second coat of thermal plastic to the specimen and thus also eliminated the need for the specimen to be washed with acetone a second time.

There was a slight difference in height between the two glass slides on either side of the specimen, but it was very close and far more precise than sanding them free hand. It also helped to control the angle at which the specimens were sanded so the edges of the specimen wouldn't be rounded. After sanding, the variation in thickness would usually decrease to less than 0.06 mm. The specimens were sanded, individually or could be sanded in groups of 2 or 3, see Figure 2.2.3.

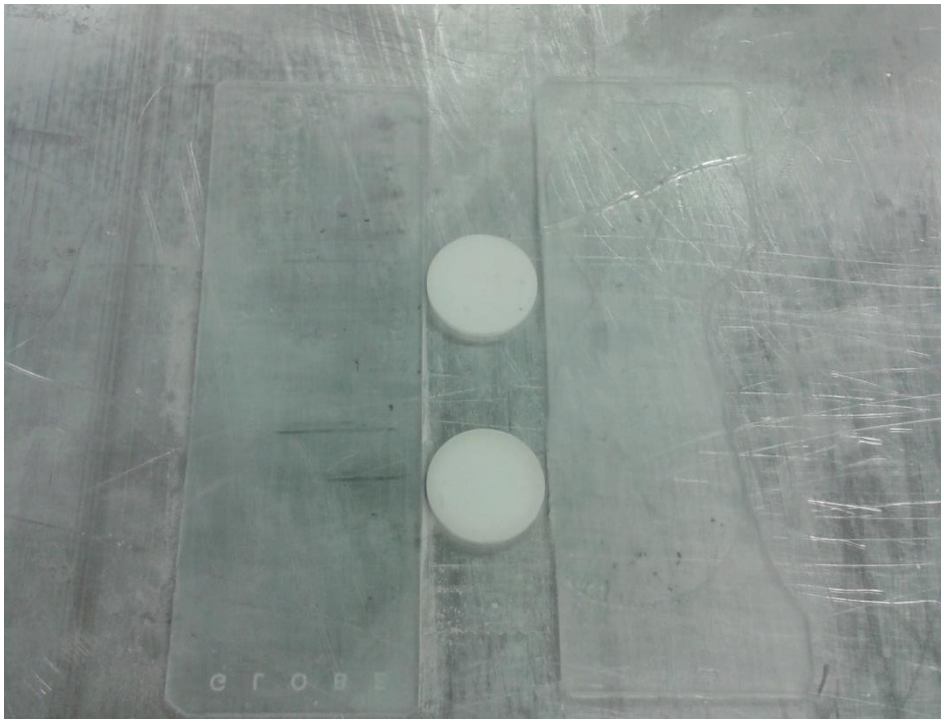

Figure 2.2.3 The specimens to be sanded were placed between the two glass slides and were sanded down to the thickness of the glass slide. In the image, this specimen is taped down instead of being affixed with thermoplastic. Using thermoplastic to attach the specimens to the aluminum plate would have required another round of acetone washing, so taping the specimen was preferred.

The specimens were sanded using 400 grit sand paper. When they were sanded down to the height of the glass slide, the specimens were then removed from the aluminum plate. If they were secured with thermoplastic they would have to be cleaned with acetone wipes, similar to the procedure after cutting. This method using the glass slides, as depicted in Figure 2.2.3, had a sever limitation: all specimens would be sanded to the thickness of the glass slides, which was about 1.16mm.

A later iteration of the sanding process involved using the lapping fixture from lab 2530 (Southbay Technologies model #150) to make parallel faces. If the specimen was a middle section of the original billet, the specimen would have parallel faces; but if one of the two circular faces of the specimen was one of the original billet faces, it would not be precisely parallel to the cut face. In this circumstance the lapping fixture was used. The specimen was affixed to the lapping fixture using double sided tape with the cut surface facing out, that way the cut surface became parallel to the original billet surface which was at a 90˚ angle of the radial surface of the disk. Once the surfaces were made parallel by sanding, the sample was removed from the double sided tape. If further sanding was required the specimen was held down against sandpaper by hand and lightly sanded in a circular fashion, then changing directions. The specimen would be sanded an equally number of times clockwise as counterclockwise. After a few changes of direction, the specimen would be rotated around and sanded on a different area of the sand paper.

The sandpaper that was used was Silicon Carbide (SiC) with a grit number 600. Typically, if more than 0.2mm needed to be removed (usually in the case where the specimen's faces were not parallel and were being sanded to make them parallel) lower grit number

sandpaper (400 or 240) would be used to start. A final polish of 600 would be used before the specimen was analyzed using RUS. Later a final polish of 1200 would be utilized.

Changing the sanding procedure allowed less material to be wasted. The height of the glass slides required every sample to be sanded to the same height. For example, In the later sanding method, when a sample was cut with an average thickness of 1.40 mm but did not have parallel faces, rather than sanding it with the glass slide fixture (see Figure 2.2.3) and losing about 0.24 mm worth of material, it would only need to be sanded until it was parallel.

2.3 Resonant Ultrasound Spectroscopy Scan

The resonant ultrasound spectroscopy (RUS) scanning and analysis are the most involved steps of the procedure, and accordingly have the most software to assist in the tasks. Resonant Ultrasound Spectroscopy (RUS) is a non-destructive method for determining elastic modulus of a specimen [Zadler 2004].

2.3.1 Initial Measurement

Resonant Ultrasound Spectroscopy (RUS) equipment (Quasar RUSpec, Quasar International, Albuquerque, NM) was used for the measure the elastic moduli. A three transducer setup was used, one drive transducer and two receivers. The transducers were arranged so that they touched the corners of the specimen, this allows for the optimal transfer of vibrations in and out of the specimen and minimal mechanical impendence [Migliori 1993].

Figure 2.3.1 An aluminum sample mounted to the three transducer setup. Notice in the image how the transducers are on the edge of the specimen. The transducers are rounded so the contact area is very small. Aluminum was not studied here, but the large specimen makes a clear visual.

One of the three transducers in the RUS apparatus is a driver transducer that induces sinusoidal mechanical vibrations in the specimen. The driving frequency is swept through a range of frequencies, where the upper and lower frequency limits are set prior to the RUS scan. As the driving frequency is increased, the specimen will resonate at characteristic frequencies that depend on the specimen density, composition, dimensions and porosity. When the specimen vibrates at a resonant frequency, it creates a sharp rise in amplitude, or a peak, see Figure 2.3.2. The set of characteristic resonance frequencies create a spectrum for this particular specimen. The RUS experiment is controlled and recorded by the software (Quasar Galaxy RI2000 and RPModel software, Quasar International). For each specimen, the measurements were repeated several times. The specimen was rotated or flipped several times to get different scans. Each time the specimen was moved, the transducer contacts the specimen at a different set of points. Some points on the specimen will have little or no mechanical

vibration these are called antinodes. Antinodes cause the receiver transducers to detect lower amplitude peaks or miss certain vibrational modes altogether. Taking multiple scans from different transducer contact points can reveal low amplitude peaks or modes that do not show up at different contact points. In light of the presence of antinodes in the specimen, it should be noted that the corners of the specimen is the least likely point to contain the antinodes [Migliori 1993]. The frequency ranges was between 3 to 600 kHz. Most vibrational modes that were detected were in the range of 30 to 400 kHz, above that range the vibrational modes were too small in amplitude to differentiate from noise.

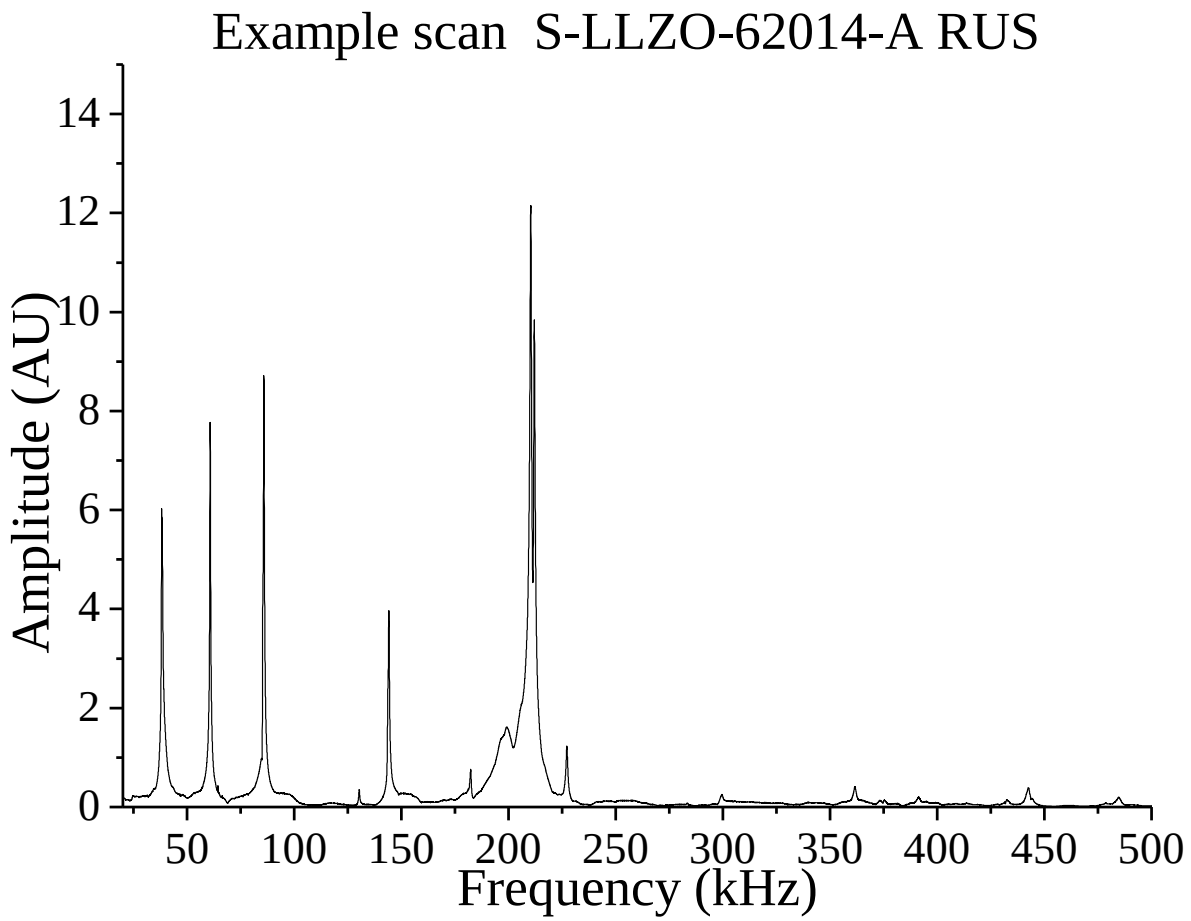

Figure 2.3.2 RUS scan from an unlithiated LLZO specimen S-LLZO-62014-A. The actual scan was taken from 3 kHz to 503 kHz. Notice the higher frequencies have much smaller amplitudes, making them harder to identify and therefore less useful in the RUS analysis of the elastic moduli. (AU stands for arbitrary units).

2.3.2 Initial Prediction

The spectrum is a bit like a finger print from which the properties of the Young's modulus (E), shear modulus (G) and Poisson's ratio (ν) can be determined. To do so, the Quasar Galaxy RI2000 and RPModel software are used with Microsoft Excel. An initial guess for two of the three properties (E, G and ν) must be used. Using two of the three values (E, G and ν), it is possible to calculate the elastic stiffness constants, C11, C12 and C44. Only C11 and C44 are independent for isotropic materials, where E, G and ν can be determined. The initial guesses for the elastic moduli has to be relatively close to the actual properties to avoid divergence and to minimize calculating time in the model [Zadler 2004]. Dimensions and mass of the specimen being analyzed were also needed.

All of the LLZO specimens analyzed in this study are assumed to be cubic crystal structures where it is assumed that there is no preferential orientation of grains (no texturing), thus the specimens are assumed to be isotropic.

A search of literature can sometimes generate a sufficient starting point (an adequate initial guess for the elastic moduli). In the case of LLZO, elastic modulus values obtained for LLZO by Ni et al.[Ni 2012] provided a starting point for LLZO specimens included in this study. In all cases, the elastic moduli are a function of specimen porosity, P, which can be determined by finding the density of the specimen, ρ, and comparing it to the theoretical density of 100% dense LLZO, ρ_{theo}=5.107g/cm^3 [Ni 2012]

$$P = \frac{\rho_{\text{theo}} - \rho}{\rho_{\text{theo}}} \qquad 2.3.1$$

Values determined by Ni et al. [Ni 2012] are available in Table 2.3.1.

Table 2.3.1 Values of elastic moduli at select porosity values from Ni et al.[Ni 2012]

	Porosity	E (GPa)	E (GPa) uncertainty	G (GPa)	G (GPa) uncertainty
LLZO-01a	3.0%	149.8	± 0.4	59.6	± 0.1
LLZO-02a	6.0%	132.6	± 0.2	52.1	± 0.04

Table 2.3.1 leaves some uncertainty for samples that have porosity other than the samples listed in Table 2.3.1. Initially whichever value was closer to the measured specimen porosity was used as the starting point for a RUS analysis. As more results from analyzing specimens were obtained, better starting estimates could be obtained, this will be discussed further in Section 3.2.1.

2.3.3 RUS Analysis

Two different models can be used to analyze the specimens depending on their dimensions. For thin cylinder or disk specimens, CylModel (Quasar International) is used, and for a rectangular parallelepiped the RPModel (Quasar International) is used. Once the initial guesses for elastic moduli and the dimensions and mass are entered into the Quasar Galaxy software, the software will predict the set of resonant frequencies for the specimen, as shown in Figure 2.3.3. The amplitude of the peaks are in arbitrary units [Fan 2013b]

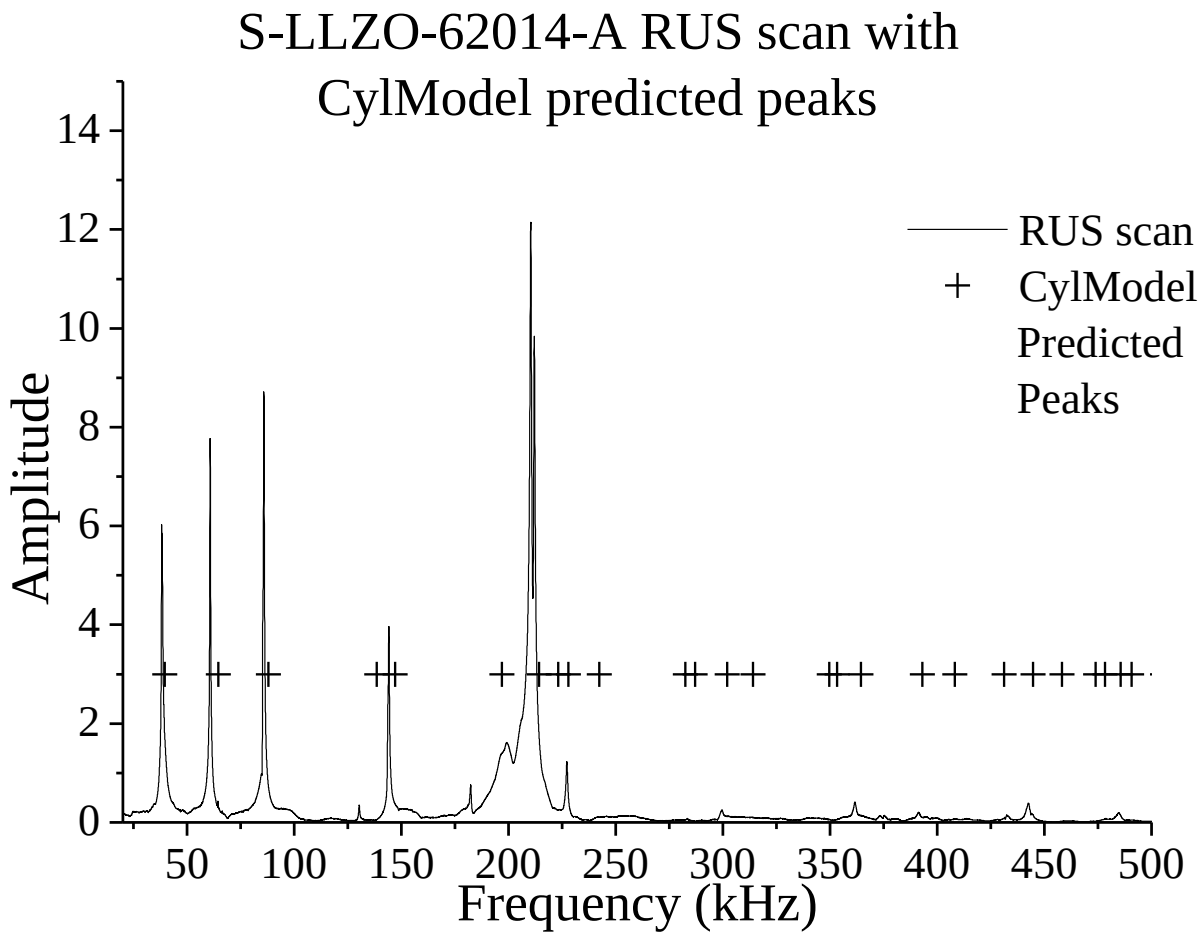

Figure 2.3.3 Same scan of S-LLZO-6-2014-A as Figure 2.3.2 but with the CylModel predicted resonance peaks. The black line represents the RUS scan. The sharp peaks on the black line represent a frequency from the driver transducer that resonates with the specimen. The black crosses (+) represent the CylModel software's calculation for the frequency at which resonance is predicted to occur. The predicted frequencies are displayed here at an amplitude of 3 so they can be distinguished clearly from the scan (AU stands for arbitrary units).

The user then matches the predicted peaks to the RUS peaks, and then the software recalculates. This is repeated several times until all the peaks that can be matched have been entered. Figure 2.3.4 shows the same scan as Figure 2.3.2 and Figure 2.3.3 but with the peaks that were reported to the CylModel marked with red squares.

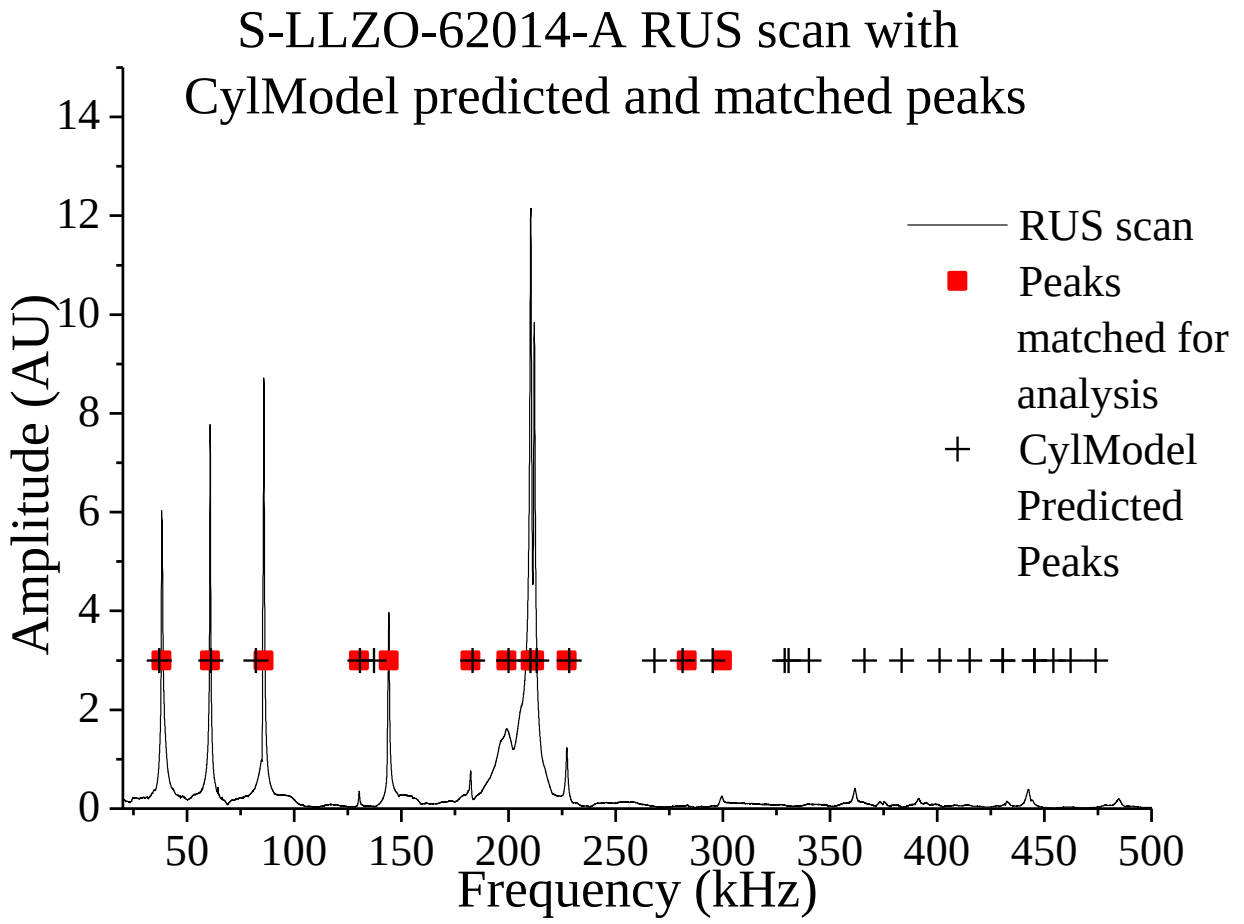

Figure 2.3.4 The RUS scan of S-LLZO-62014-A with CylModel predicted peaks as black crosses (+) and peaks that were reported to the CylModel as red squares. The black line represents the RUS scan. Notice the predicted peaks (+) have shifted from their location in Figure 2.3.3. (AU stands for arbitrary units).

Figure 2.3.4 is a RUS scan with indicators for the CylModel analysis. As previously stated, the CylModel predicts where the resonance frequencies are, which are plotted with the RUS scan in Figure 2.3.3 and Figure 2.3.4. The red squares in Figure 2.3.4 identifies the actual frequency from the RUS scan that the predicted peak correlates to. As the user matches the peaks, typically the lowest peaks are matched first. Lower frequencies tend to make more distinct peaks, as seen in RUS scan in Figure 2.3.4. Matching the lower frequency predicted peaks by the CylModel to the actual peaks in the RUS scan adjust the predicted peaks and helps to identify matches between the prediction and the actual scan at higher frequencies. It can also

be observed in Figure 2.3.4 that higher frequencies (above about 250 kHz in this case) are lower in amplitude, when the amplitude is very low, it is obscured by the background noise. Sometimes there will be high frequency peaks that have high amplitudes but if several peaks before it are not identifiable, it cannot be certain if the predicted peak and a RUS peak with similar frequency are actually correlated. This emphasizes the necessity for matching peaks at low frequencies and gradually working up to high frequencies.

After the user matches the predicted peak with the actual peak on the RUS scan, the CylModel will recalculate and change the frequencies of the predicted plots. Initially a set of values for E, G and ν were used to begin the RUS analysis. This set of elastic moduli values, in conjunction with the mass and volume of the specimen, produced a set of predicted peaks. As the predicted peaks were matched to the RUS peaks, the predicted peaks changed and so did the predicted values for the elastic moduli. It can be observed that the predicted peaks in Figure 2.3.3 are different than the predicted peaks in Figure 2.3.4 due to the CylModel recalculating after the predicted peaks and actual peaks are matched. As the matching of the predicted peaks and RUS scan peaks improves, the root mean square error, RMS, will decrease. The RMS is a measure of how well experimental RUS results can be modeled [Ulrich 2002].

A good fit will have many peaks matched and a low RMS. There are several sources to help define what number of peaks and what value of RMS make a good fit for the RUS analysis. Migliori et al. [Migliori 1997] suggests a good fit between a model and a RUS scan should have an RMS less than 0.2% with 30 peaks fitted. Reports for inhomogeneous specimens suggest that RMS values greater than 1% represent errors in the RUS analysis that are too large to be regarded as valid data [Ulrich 2002]. One study by Ren et al.[Ren 2009] reported RMS values of 0.23% to 0.99% and peak count of 18 to 34. However, there is no

standardly accepted value for RMS or peak count that will validate or invalidate RUS results [Ulrich 2002].

3.0 Results and Discussion

Values for elastic moduli were obtained for various specimens of LLZO. The results were also quite varied. Many factors could have contributed to the variation in elastic moduli, which will be discussed here.

3.1 Tables of Results

Values for specimens analyzed over the course of this study are presented in Table 3.1.01 and Table 3.1.02.

Table 3.1.01 specimen label, dimensions, mass, density and date analyzed for specimens analyzed over the course of this study. For the dimensions, if two dimensions are given, they are height by diameter, if three dimensions are given, it is the three dimensions of a parallelepiped.

Specimen Label	**dimensions** (mm)	**mass** (g)	**Density** (g/cm^3)	**Date analyzed**
LLZO-01a [Ni 2012]			4.97	
LLZO-02a [Ni 2012]			4.78	
S-LLZO-6314-1	1.158 x 12.720	0.729	4.95	6/11/2014
S-LLZO-6314-3	1.175 x 12.683	0.711	4.79	6/12/2014
S-LLZO-62014-A	1.200 x 12.735	0.7059	4.62	7/04/2014
S-LLZO-62014-C	1.253 x 10.758 x 4.860	0.3124	4.77	7/04/2014
S-LLZO-71014-A	1.097 x 12.709	0.6587	4.73	7/16/2014
S-LLZO-71014-B	0.673 x 12.663	0.4114	4.85	7/15/2014
S-LLZO-71014-C	1.147 x 12.663	0.7155	4.95	7/16/2014
S-LLZO-71014-D	1.196 x 12.664	0.7547	5.01	7/16/2014
S-LLZO-72914-A	1.524 x 6.212 x 9.484	0.4464	4.97	7/31/2014
S-LLZO-72914-B	1.276 x 12.664	0.8112	5.05	7/31/2014
S-LLZO-72914-C	1.238 x 12.659	0.7896	5.07	7/31/2014
S-LLZO-92314-A pre sanding	1.337 x 12.602	0.8336	5.00	10/3/2014
S-LLZO-92314-A post sanding	1.241 x 12.625	0.7699	4.96	10/3/2014
S-LLZO-92314-B pre sanding	1.495 x 12.613	0.9473	5.07	10/3/2014
S-LLZO-92314-B post sanding	1.390 x 12.628	0.8721	5.01	10/3/2014
S-LLZO-92314-C pre sanding	1.126 x 12.571	0.7022	5.03	10/7/2014
S-LLZO-92314-C post sanding	1.097 x 12.583	0.6840	5.01	10/7/2014
S-LLZO-92314-B.2 pre sanding	1.389 x 7.348 x 9.415	0.4844	5.04	10/21/2014
S-LLZO-92314-B.2 post sanding	1.320 x 7.350 x 9.417	0.4606	5.04	10/21/2014

Table 3.1.02 specimen label, porosity (P), Young's modulus (E), Poisson's ratio, the RMS of the RUS analysis using the CylModel or RPmodel software, and the number of peaks that were matched in the analysis for various specimens analyzed over the course of this study.

Specimen Label	P	E (GPa)	G (GPa)	Poisson's ratio	RMS	peaks
LLZO-01a [Ni 2012]	3.0%	149.8	59.60	0.257	N/A	
LLZO-02a [Ni 2012]	6.0%	132.6	52.10	0.274	N/A	
S-LLZO-6314-1	3.0%	107.4	40.68	0.320	0.435%	26
S-LLZO-6314-3	6.3%	95.4	36.35	0.312	0.215%	24
S-LLZO-62014-A	9.6%	116.5	45.07	0.293	0.690%	16
S-LLZO-62014-C	6.6%	129.0	50.65	0.274	0.262%	14
S-LLZO-71014-A	7.3%	114.5	44.02	0.300	0.661%	14
S-LLZO-71014-B	5.0%	117.2	45.00	0.302	0.829%	18
S-LLZO-71014-C	3.0%	118.9	46.22	0.286	0.734%	16
S-LLZO-71014-D	1.9%	116.0	44.24	0.311	0.399%	12
S-LLZO-72914-A	2.7%	101.0	38.36	0.317	0.578%	8
S-LLZO-72914-B	1.2%	99.7	37.52	0.329	0.667%	14
S-LLZO-72914-C	0.8%	96.3	35.97	0.339	0.552%	14
S-LLZO-92314- A pre sanding	2.1%	92.2	34.31	0.343	0.939%	16
S-LLZO-92314- A post sanding	2.9%	90.7	33.62	0.349	0.536%	18
S-LLZO-92314- B pre sanding	0.7%	96.7	35.76	0.353	0.654%	18
S-LLZO-92314- B post sanding	1.9%	94.0	34.91	0.346	0.610%	20
S-LLZO-92314- C pre sanding	1.6%	99.1	37.51	0.322	0.609%	16
S-LLZO-92314- C post sanding	1.8%	97.4	36.21	0.346	0.740%	16
S-LLZO-92314- B.2 pre sanding	1.3%	97.1	35.88	0.353	0.677%	10
S-LLZO-92314- B.2 post sanding	1.3%	94.5	34.94	0.352	0.324%	11

3.1.1 Specimens Received 6-3-14

The first values in Table 3.1.01 and Table 3.1.02 are the results from published work by Ni et al.[Ni 2012]. Both tables show results for specimens that were analyzed over the course of this study. Each set of specimens was compared to the values reported by Ni et al.

Samples from the billet received on 6/3/14 were labeled as S-LLZO-6314-A and S-LLZO-6314-C. The results from the RUS analysis were reported in Table 3.1.01 and Table 3.1.02. The specimens were cut (according to section 2.2.1) and sanded using the glass slide fixture (according to section 2.2.2). The specimens were sanded to reduce the variation in height across the specimen, where the height variation was initially about 0.4 mm and was reduced to about 0.04 mm or less for the two specimens via sanding. Both specimens were disks, and although they were cut from the same billet, they had different densities. This demonstrates that the processing used for LLZO specimens induced a density gradient axially through the billet. The density gradient was most likely due to porosity which will be discussed further in section 3.2.1) A density gradient was observed in each successive billet received and analyzed. A low RMS and a good number of peaks were achieved from the RUS analysis (see section 2.3.3 for discussion on what defines a "good fit"). A third specimen from the same billet was analyzed, but the results were not included because the RMS (0.650%) was much higher than either of the other specimens.

The results for the elastic moduli of specimens S-LLZO-6314-1 and S-LLZO-6314-3 were lower than the results reported in Ni et al. [Ni 2012] which had similar porosities (see Table 3.1.02). S-LLZO-6314-1 had a porosity of 3%, E= 107.4 GPa and G= 40.68 GPa, where Ni et al. [Ni 2012] reported E= 149.8 GPa and G= 59.6 GPa at the same porosity of 3%. S-LLZO-6314-3 had E= 95.4 GPa and G= 36.35 GPa and LLZO-02a from Ni et al.[Ni 2012] had

E= 132.6 GPa and G= 52.10 GPa, and both specimens a porosity of approximately 6%. Some of the possible causes for why the values for S-LLZO-6314-1 and S-LLZO-6314-3 were lower than those reported in Ni are discussed in section 3.2.2, section 3.25 and section 3.2.4.

3.1.2 Specimens Received 6-20-14

The next specimens to be analyzed were S-LLZO-62014-A and S-LLZO-62014-C. Initially the sample was cut into three specimens and analyzed. The initial results were questionable because few peaks could be matched, and the RMS was higher than previous specimens (see Table 3.1.03).

Table 3.1.03 specimen label, Young's modulus (E), Poisson's ratio (ν), the RMS of the RUS analysis using the CylModel or RPmodel software, the number of peaks that were matched, as well as mass, dimensions, density and porosity (P) of the initial measurements for specimens S-LLZO-62014

(Units)	**E** (GPa)	**G** (GPa)	**ν**	**RMS**	**peak count**	**mass** (g)	**Dimensions** (mm)	**density** (g/cm^3)	**P**
A- disk	121.99	48.91	0.247	0.654%	11	1.03	12.75 x 1.75	4.62	9.6%
B- disk	104.69	43.85	0.194	1.202%	13	0.89	12.71 x 1.50	4.70	8.0%
C- disk	130.05	51.07	0.273	0.399%	14	0.77	12.67 x 1.27	4.85	5.1%

After the results in Table 3.1.03 were obtained the specimens were further processed in an attempt to get better results from another RUS scan. Specimen S-LLZO-62014-A was sanded from a thickness 1.75 mm to 1.20 mm. The thinner specimen attenuated the RUS vibrations less, which allowed more peaks to be fitted, making the results more reliable. Specimen S-LLZO-62014-C was cut from a disk 1.25 mm thick and 12.7 mm in diameter to a rectangular parallelpiped 10.7 mm long and 4.86 mm wide, with the same thickness as before it was cut, 1.27 mm. Making this specimen smaller reduced the material, which made the

specimen more uniform. This method also helped improve the RUS scan by reducing the RMS, as shown in Table 3.1.04.

Table 3.1.04 specimen label, Young's modulus (E), Poisson's ratio (ν), the RMS of the RUS analysis using the CylModel or RPmodel software, the number of peaks that were matched, as well as mass dimensions density and porosity (P) of specimens S-LLZO-62014-A and S-LLZO-62014-C

(Units)	**E** (GPa)	**G** (GPa)	**ν**	**RMS**	**peak count**	**mass** (g)	**Dimensions** (mm)	**density** (g/cm^3)	**P**
S-LLZO-62014-A	116.52	45.07	0.293	0.690%	16	0.710	12.75 x 1.20	4.617	9.59%
S-LLZO-62014-C	129.01	50.65	0.274	0.260%	14	0.312	1.27 x 10.76 x 4.86	4.769	6.62%

The initial porosity of sample C, when cut into a disk, was 5.1% (Table 3.1.03), but when it was cut into a parallelpiped the porosity was 6.6% (Table 3.1.04). This indicates there is also a radial density gradient in the sample. Thus, from the density measurements, it was apparent that there was a density gradient in both the axial and radial directions.

The RUS analysis was difficult since only a few resonant peaks were available for each specimen. However, once the samples were further processed (made thinner by sanding or being cut into a smaller rectangular parallelpiped) the RUS analysis improved, that is, additional RUS peaks could be matched which in turn leads to more reliable determination of the elastic modulus. Sanding sample A allowed 16 peaks to be fitted, as opposed to 11 before the specimen was sanded. Sample C still had 14 peaks fitted after it was cut into a rectangular parallelepiped, but the RMS dropped from 0.399% to 0.262%. The first five peaks for the cylinder model for sample S-LLZO-62014-A were obvious, but over 250 kHz, the amplitude of the resonance peaks dropped off. Some of the peaks over 250 kHz were still readable, but matching the peaks of the model to the RUS scan was increasingly difficult above 250 kHz

because the amplitude of the peaks was very small and of a similar magnitude as the noise floor. No peaks over 300 kHz could be matched for specimen S-LLZO-62014-A.

In general, for RUS analysis, Poisson's ratio is much more sensitive to an erroneous analysis than either the Young's modulus or shear modulus. For specimens A and C, the values for elastic modulus, E, and shear modulus, G, in Table 3.1.04 agree well with the results from Ni et al. [Ni 2012]. In addition, the modulus versus porosity behavior of specimens A and C agrees well with that of the two specimens from the Ni et al. [Ni 2012]. Sample C of this study had a porosity of 6.6%, E=129.0 GPa and G= 50.7 GPa. In the study from Ni a specimen with a porosity of 6.0% had E= 132.6 GPa and 52.1 GPa. The Poisson's ratio for specimen C and the 6% porous specimen from et al. Ni et al. [Ni 2012]both had a Poisson's ratio of 0.274. The agreement between the Poisson's ratio for specimen S-LLZO-62014-C of this study and the Poisson's ratio from the study in Ni et al. [Ni 2012] indicates that, at least for specimen C, the results of the sample S-LLZO-62014 is in relatively good agreement with the Ni et al. [Ni 2012] study. Specimen A had a higher porosity, 9.59%, and lower elastic moduli values, and even though there was no sample from Ni et al. [Ni 2012] with similar porosity to compare it to, it did follow the trend of decreasing elastic moduli with increasing porosity, see Figure 3.1.01.

The four specimens in Figure 3.1.01 (specimens S-LLZO-62014-A and S-LLZO-62014-C from this study and the two specimens from Ni et al. [Ni 2012]) each had a different porosity. The Young's modulus and shear modulus of the four specimens are plotted versus porosity, (Figure 3.1.01.). A least squares fit of the four specimens is also plotted in Figure 3.1.01 (red line represents G and black line represents E) based on the relationship

$$R(P)=R_0*\exp(-B*P) \qquad 3.1.01$$

where R(P) is porosity dependent elastic modulus (either Young's modulus or shear modulus), R_0 is the elastic modulus property of the material at theoretical 100% density, P is the porosity of the specimen and B is a fitting parameter unique to the material.

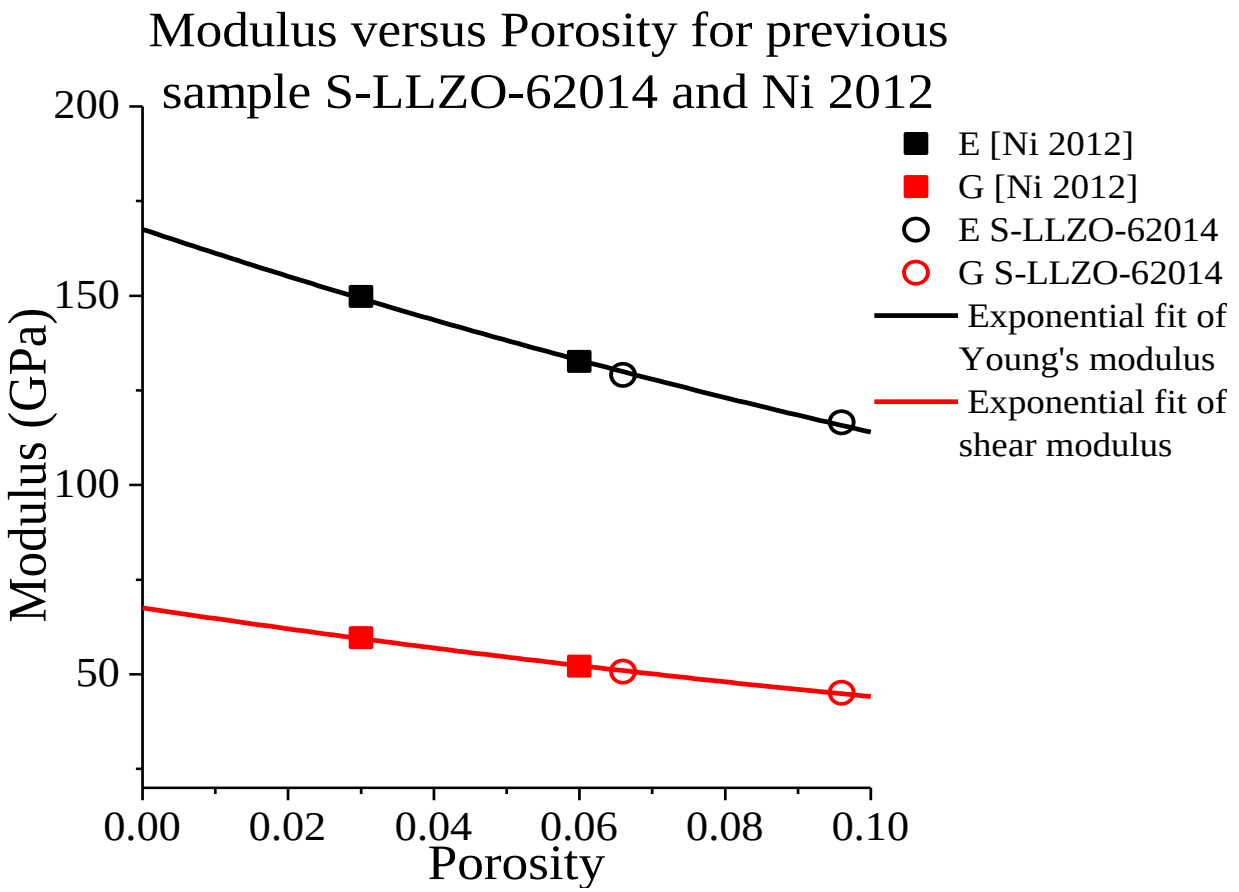

Figure 3.1.01 Porosity versus Young's modulus, E, and shear modulus G, for LLZO specimens S-LLZO-62014-A and S-LLZO-62014-C, cut from the billet S-LLZO-62014, compared to elasticity data from the study by Ni et al. [Ni 2012]. Squares are the values from Ni 2012 and the circles are the data from this study. The red line represents the least-squares fit of Equation 3.1.01 for shear modulus, G, and the black line represents the least-squares fit of Equation 3.1.01 for Young's modulus, E.

Analysis of S-LLZO-62014 yielded results for elastic moduli similar to values in literature Ni et al. [Ni 2012]. The data set in Figure 3.1.01 allowed one to estimate the elastic moduli for a given porosity, which will be discussed further in section 3.2.1.

The original intention was to cycle (and lithiated) a specimen after it was analyzed using the RUS and then analyze the specimen again post-lithiation. Unfortunately, that would not be possible for these specimens. The thermoplastic was washed off by setting the specimens into acetone. Furthermore, the specimens were stored in a way that allowed it to be exposed to air. Lithium is highly reactive and may react to moisture and carbon dioxide in the air. This was corrected for future specimens, acetone was no longer applied directly to the specimen and the specimens were stored in an argon filled glove box to prevent exposure to open atmosphere. However because of the exposure already incurred, the specimens S-LLZO-62014 were not lithiated and re-analyzed.

3.1.3 Specimens Received 7-10-14 and 7-29-14

Specimens received 7-10-14 and 7-29-14 underwent the same processing as one another, which was slightly different than the processing for previous specimens (S-LLZO-6314 and S-LLZO-62014). After each specimen was cut from the billet, they were washed with acetone. However, to avoid the acetone getting into the pores of the specimen, the acetone was only applied to the Kim wipes and no longer applied directly to the surface of the specimen. The specimens were taped down using double sided tape when they were sanded, instead of using thermoplastic to secure them in place. This allowed a second round of acetone washing to be avoided. Sample S-LLZO-72914-A was cut into a rectangular parallelepiped; all other specimens remained as cylindrical disks. S-LLZO-71014 was cut into 4 specimens, and S-LLZO-72914 was cut into 3 specimens. The most important change to the procedure was the specimens were stored in a glove box to minimize carbon dioxide and moisture exposure whenever they were not being processed or analyzed.

The results of the analyses for samples S-LLZO-71014 and S-LLZO-72914 are displayed in Table 3.1.01 and Table 3.1.02. The elastic modulus results versus porosity are plotted in Figure 3.1.02 for S-LLZO-62014, S-LLZO-71014 and S-LLZO-72914, as well as Ni et al. [Ni 2012] for comparison.

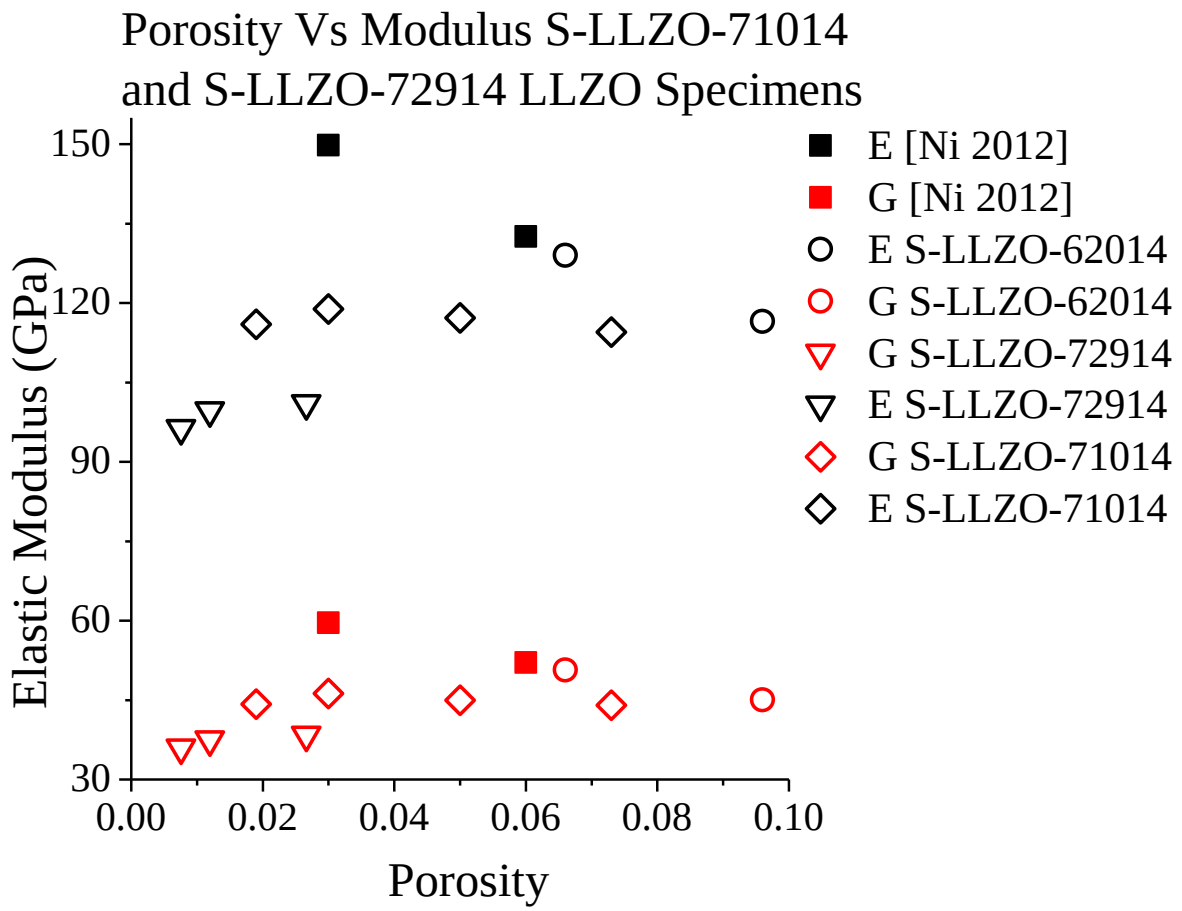

Figure 3.1.02 Porosity vs modulus for specimens received 7/10/14 and 7/29/14 as well as results from Ni et al. [Ni 2012] and S-LLZO-62014 for comparison. Young's modulus is in black, and shear modulus is in red. The filled symbols are from literature and the open symbols were tested in this study. E is Young's modulus and G is shear modulus.

For specimens received 7/10/14 and 7/29/14, the modulus results were noticeably lower than Ni et al. [Ni 2012], see Table 3.1.05. Each group of samples that were cut from a different billet seemed to follow its own trend, but there is no clear overall trend between all the specimens. At this point it was considered that some sort of defect may be forming in the material. This could be visible defects such as cracking or chipping, or defects that were

invisible to the naked eye, such as impurities or microcracks. If impurities were present in the specimen, it is possible that fewer peaks might be identified in the RUS scan. If the LLZO samples from S-LLZO-71014 and S-LLZO-72914 contained multiple phases or impurities, the elastic moduli of the specimen would be dependent on how much of each phase or impurity was present, and the elastic moduli of the impurity phases themselves. Furthermore, if there was an impurity that formed a solid solution with LLZO, it could a more complicated effect on the elastic moduli. The effects of different phases, impurities and solid solutions will be discussed further in sections 3.2.

Table 3.1.05 specimen label, porosity (P), Young's modulus (E), Poisson's ratio, the RMS of the RUS analysis using the CylModel or RPmodel software, and the number of peaks that were matched in the analysis for samples S-LLZO-71014 and S-LLZO-72914 and specimens from Ni et al. [Ni 2012]

	Specimen Label	P	E (GPa)	G (GPa)	Poisson's ratio	RMS	peaks
1	**LLZO-01a** [Ni 2012]	3.0%	149.8	59.60	0.257	N/A	
2	**LLZO-02a** [Ni 2012]	6.0%	132.6	52.10	0.274	N/A	
3	**S-LLZO-71014-A**	7.3%	114.5	44.02	0.300	0.661%	14
4	**S-LLZO-71014-B**	5.0%	117.2	45.00	0.302	0.829%	18
5	**S-LLZO-71014-C**	3.0%	118.9	46.22	0.286	0.734%	16
6	**S-LLZO-71014-D**	1.9%	116.0	44.24	0.311	0.399%	12
7	**S-LLZO-72914-A**	2.7%	101.0	38.36	0.317	0.578%	8
8	**S-LLZO-72914-B**	1.2%	99.7	37.52	0.329	0.667%	14
9	**S-LLZO-72914-C**	0.8%	96.3	35.97	0.339	0.552%	14

Table 3.1.06 specimen label, porosity (P), Young's modulus (E), Poisson's ratio, the RMS of the RUS analysis using the CylModel or RPmodel software, and the number of peaks that were matched in the analysis for S-LLZO-71014 before and after it was lithiated

Specimen Label	dimensions (mm)	P	E (GPa)	G (GPa)	ν	RMS	peaks
S-LLZO-71014-C unlithiated	1.147 x 12.663	3.00%	118.90	46.22	0.286	0.734%	16
S-LLZO-71014-C lithiated	1.130 x 12.660	2.71%	122.64	47.63	0.287	0.775%	14

Specimen S-LLZO-71014-C was tested after being lithiated. This was the only specimen that was tested after lithiation, and the results are displayed in Table 3.1.06. Fewer peaks could be matched and the RMS was still high. As stated in section 2.3.3. Migliori et al. [Migliori 1997] suggests a good fit between a model and a RUS scan should have an RMS less than 0.2% with 30 peaks fitted. S-LLZO-72914-C before and after being lithiated did not meet these standards. The results for S-LLZO-72914-C lithiated and unlithiated (Table 3.1.06) are outside of the standard suggested by Migliori et al. [Migliori 1997]; The RMS of the specimen is 0.734% which is greater than the suggested 0.2%; and the peak count is 14 (lithiated) and 16 (unlithiated) which is less than the suggested 30. However, LLZO has been inhomogeneous in previous studies by Thompson et al.[Thompson 2014], in which case, the RMS is expected to be higher [Ulrich 2002]. The RMS from S-LLZO-72914-C RUS analysis is within the range reported by Ren et al. [Ren 2009] (0.23% to 0.99%) for a study on alumina and hydroxyapatite. The peaks count of S-LLZO-72914-C is close to the low end of the range of peak counts in the same study by Ren et al.(18-34 peaks). With all this in consideration, the results of S-LLZO-72914-C lithiated and unlithiated, are not "good". Without more specimens being analyzed using the RUS to determine elastic moduli before and after lithiation, it is difficult to draw decisive conclusions from the data in Table 3.1.05.

3.1.4 Specimens Received 9-23-14

The LLZO billet received on 9-23-14 was cut into three specimens and analyzed using resonance ultrasound spectroscopy (RUS) and CylModel software. The specimens were sanded to improve geometry then scanned using RUS. Then the specimens were sanded and scanned again to try to identify any impact sanding had on the specimens. The results are displayed Table 3.1.07 and can be compared to previous work in Table 3.1.01.

The specimens had a low Young's and shear modulus, 90 – 100 GPa and 33-38 GPa respectively, when compared to the previous work by Ni et al.[Ni 2012] (see Table 3.1.01).

Table 3.1.07 Results from the RUS analysis. Dimensions, porosity, Young's modulus, shear modulus, Poisson's ratio, RMS, peak count and unique peak count for the Samples A, B, C and B.2, each with before and after sanding results. P is porosity, E is Young's modulus, G is shear modulus and ν is the Poisson's ratio

Specimen Label	**dimensions**	**P**	**E**	**G**	**Poisson's ratio**	**RMS**	**Peak Count**
	mm		(GPa)	(GPa)			
sample A pre sanding	1.337 x 12.602	2.13%	92.17	34.31	0.343	0.939%	16
sample A post sanding	1.241 x 12.625	2.95%	90.72	33.62	0.349	0.536%	18
sample B pre sanding	1.495 x 12.613	0.69%	96.74	35.76	0.353	0.654%	18
sample B post sanding	1.390 x 12.628	1.87%	93.95	34.91	0.346	0.610%	20
Sample C pre sanding	1.126 x 12.570	1.56%	99.14	37.51	0.322	0.609%	16
Sample C post sanding	1.097 x 12.583	1.85%	97.45	36.21	0.346	0.740%	16
sample B.2 pre sanding	0.139 x 0.735 x 0.941	1.26%	97.13	35.88	0.353	0.677%	10
sample B.2 post sanding	0.132 x 0.735 x 0.942	1.32%	94.49	34.94	0.352	0.324%	11

3.1.4.1 Discussion of Processing

There were several issues to mention in terms of specimens preparation. Starting with the processing of the specimen, the cutting of the specimen resulted in cuts that were not parallel to the existing edges (see Figure 3.1.03). This was corrected in samples A and C (the outside specimens) by sanding down the interior edge, but could

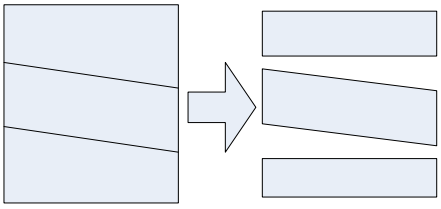

Figure 3.1.03 An exaggerated representation of how the samples were cut and sanded, sample B is in the center. Not drawn to scale or precise angle.

not be corrected in sample B without significant effort. Part of this issue arises from the "wobble" of the blade on the Buehler Low Speed Saw (Isomet Low Speed Saw, Buehler, Evanston, IL). There is a slight "wobble" or bend in the blade so when the specimen was aligned by eye, the blade may have been aligned to part of the blade that was not aligned with the rest of the blade. It is visible but not a large amount, but with a 5 mm thick specimen, a slight misalignment can be problematic.

User error cannot be dismissed either. If the glass slide slipped while it was being secured to the cutting arm, the specimen may become misaligned with the cutting blade. The wobble in the blade also makes the meticulous measurements for each cut less precise. Furthermore the micrometer on the blade arm is ruled in inches, but typically all other measurements for this study are metric so the conversation introduces opportunity for user error. The difference in thickness from specimen to specimen was not intentional.

Specimen C had less material removed between "Pre-Sanding" and "Post Sanding" RUS scans, as shown in Table 3.1.08. This was because the specimen was the thinnest to begin with and if the same amount was removed as was removed from sample A or B, it may have become too thin to re-sand and cycle.

Table 3.1.08 Thickness and changes in thickness for specimens A, B and C. For sample B, both sides were from the inside, cut edges. The surfaces of B appeared identical and could not be determined which side originally corresponded to sample A or sample C.

	sand paper grit	**A mm**	**B mm**	**C mm**
Pre-Sanding thickness		1.337	1.495	1.117
removed from outside (original billet surface)	240	0.047	N/A	0.004
removed from inside (cut side)	240	0.024	0.038/ 0.043	0.006
removed final polishing (both sides total)	600	0.026	0.025	0.010
total removed		0.096	0.105	0.019
Post Sanding thickness		1.241	1.390	1.097

Sample B had a chip missing and it was also not an ordinary circular cylinder shape, but an elliptic cylinder (see Figure 3.1.03). The volume was calculated as a regular circular cylinder so it may have had some error.

3.1.4.2 Discussion of Results

Each specimen increased in porosity after sanding as shown in Table 3.1.08. In Figure 3.1.04 each sample of S-LLZO-92314 has two data points for E and two data points for G and it can be seen that each pair shows an increase in porosity and a decrease in modulus. This shows each sample had a decreased in both density and elastic moduli after sanding.

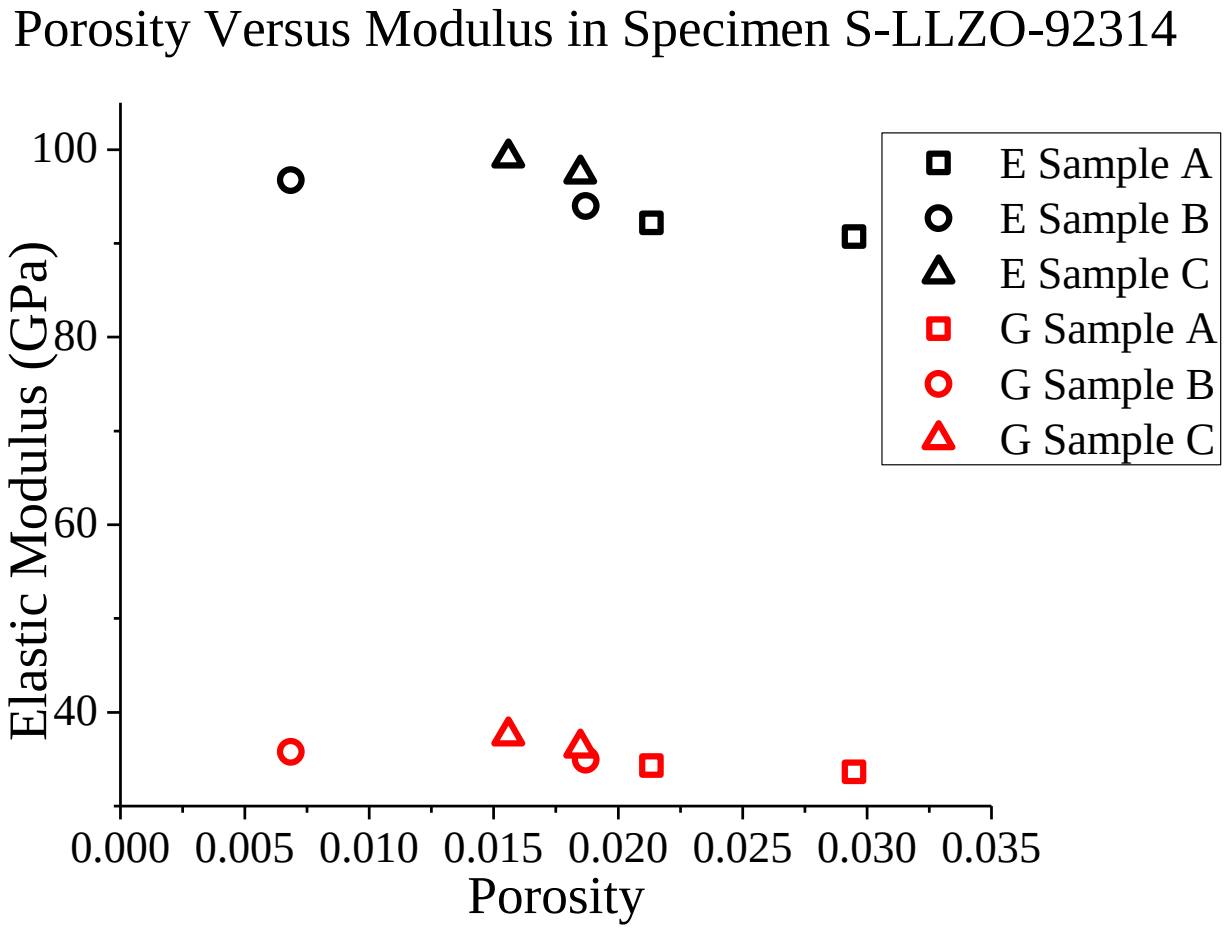

Figure 3.1.04 Young's modulus, black symbols, and shear modulus, red symbols, versus porosity for S-LLZO-92314. Each pair of data points shows a decrease in modulus and an increase in porosity after sanding.

There was a density gradient in the material, as shown in Table 3.1.07, which was denser at the side sample C was cut from. However, this is not likely the reason for the decreasing elastic moduli between sanding stages because both sides of each specimen were sanded, so the specimen should still have the same average density.

It is possible a reaction was occurring with the air that could be forming a reacted layer on the surface. If exposure to the laboratory atmosphere caused the decrease in modulus and increase porosity, the reaction rate would be an important factor. There was some variability to how long each of the specimens was in open air; therefore the impact of exposure would be a function of time. Without further analysis it is hard to determine what in particular caused the

decreased in modulus and increase in porosity. However, it can clearly be observed that in this sample, sanding and scanning the specimen using the RUS in open air corresponds with a decrease in modulus and an increase in porosity.

The most important matter to be discussed is the low modulus. The specimen is quite dense, which is good, but this specimen had the lowest modulus of any LLZO sample tested so far (see Table 3.1.01 of all the LLZO specimens tested so far). As to what is causing the low modulus there are many possible factors. There is some possibility that multiple phases or side products are forming that could reduce the elastic moduli, such as tetragonal LLZO, $LaAlO_3$ or Al_2O_3 [Thompson 2014; Geiger 2011; Rangasamy 2012], but authors often mention great care is taken to avoid multiple phases and further analysis is typically done to make sure no major side product have formed [Wolfenstine 2012b; Geiger 2011; Rangasamy 2012; Shimonishi 2011]. If multiple phases are present, and the material is heterogeneous, this would hinder the RUS scan making it harder to analyze. Solid solution systems can have a significant impact on elastic moduli properties, see section 3.2.5. These are possible explanations not just for S-LLZO-92314 but for the rest of the LLZO specimens that were analyzed in this study. Therefore more discussion will be devoted to these topics in section 3.2.

3.1.4.3 Discussion of RUS Scans S-LLZO-92314

Figure 3.1.05 shows three RUS scans, (a) the scan of sample S-LLZO-62014-A from early in the study with high elastic modulus, (b) is the scan of the specimen S-LLZO-92314-A Post sanding and (c) is a scan of an aluminum disk, as a reference. The frequency on the x-axis refers to the driving frequency. When the driving frequency is equal to a natural frequency in the material, it will resonate and cause a rise in amplitude, measured on the y-axis. The red squares are where the CylModel predicted the resonance frequencies would occur. Comparing

(a) to (b) in Figure 3.1.05, it can be observed that the first three major peaks are distinct in both scans and occur at higher frequencies in (a). Sample S-LLZO-62014-A in figure (a) had a higher Young's modulus, 116.5 GPa, and a higher porosity, 9.6%, than Sample S-LLZO-92314-A post sanding in figure (b). Increasing porosity is known to cause a decrease in Young's modulus as seen in Figure 3.1.06, but even with the higher porosity in S-LLZO-62014-A, it was still higher in modulus than S-LLZO-92314-A.

The materials in (a) and (b) of Figure 3.1.05 have similar composition so they should have similar scans. However, S-LLZO-62014 in (a) of Figure 3.1.05 and S-LLZO-92314 in (b) of Figure 3.1.05 are composed of the same precursors but underwent different processing techniques (S-LLZO-62014 used hydrogel and S-LLZO-92314 used solid state synthesis) therefore it is uncertain if the specimens are exactly the same or if the samples formed different impurities or different phases as one another. The specimens may be slightly different because a material with a higher Young's modulus should have peaks occurring at higher frequencies. Also, making a specimen thinner, by sanding for example, will make the peaks occur at lower frequencies without significantly altering the Young's modulus (as previously discussed, sanding the S-LLZO-92314 sample increased porosity and decreased Young's modulus which can be observed in Figure 3.1.01 and Figure 3.1.02, but there is no indication that sanding in which the porosity is not changed should decrease the Young's modulus). S-LLZO-62014-A was only slightly thinner than S-LLZO-92314-A post sanding, therefore Figure 3.1.05 (a) and (c) should be similar but they are noticeably different. There is a difference in porosity, but if that only affects elastic moduli, it should only shift the RUS frequencies of the resonant peaks scan, not add or remove resonant frequencies, and therefore peaks, altogether.

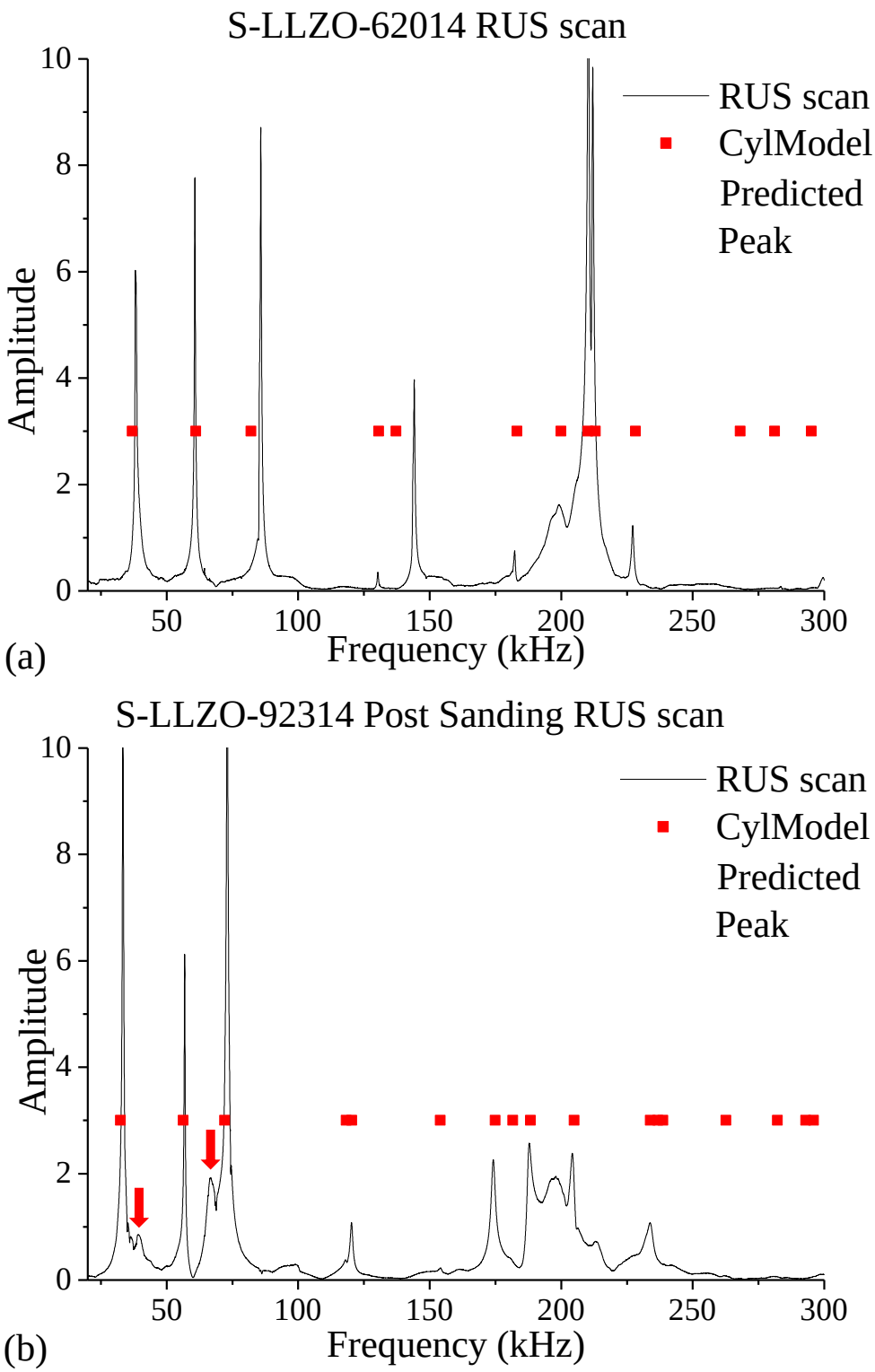

Figure 3.1.05 RUS scans of (a) sample S-LLZO-62014 from previous work, (b) S-LLZO-92314-A Post sanding from this study and (c) aluminum as a reference.

Figure 3.1.05 (cont'd)

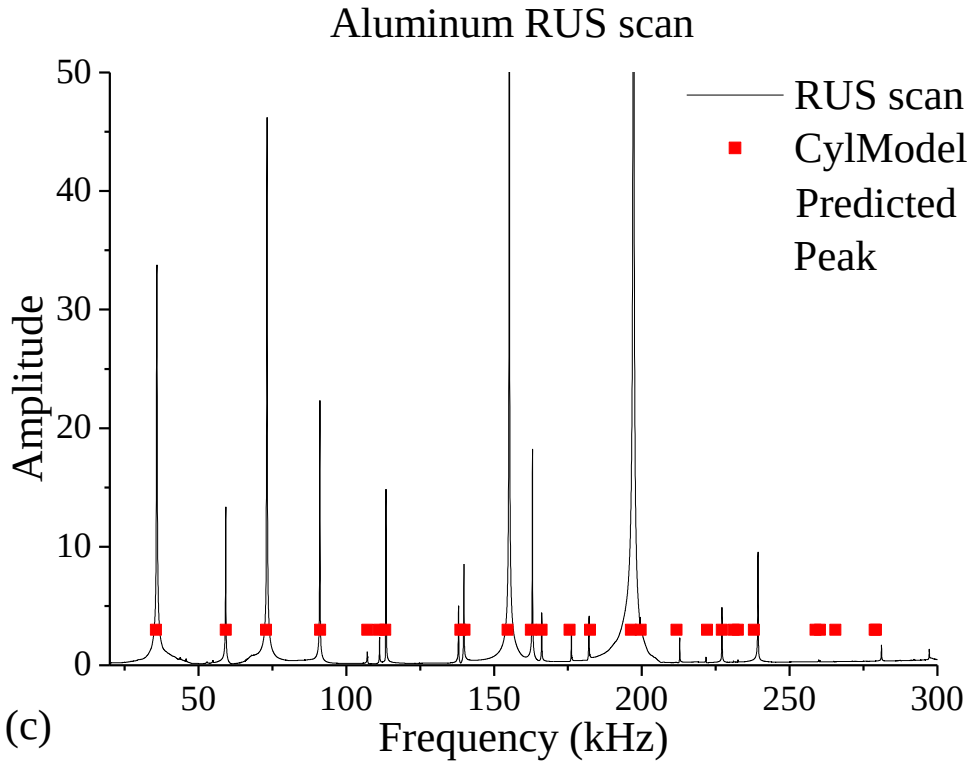

An important observation of Figure 3.1.05 is the unusual satellite peaks indicated by the red arrows in Figure 3.1.05 (b). Ideally, a RUS scan has sharp, distinct peaks that occur at the predicted frequencies; Figure 3.1.05 (c) is a good example of an ideal RUS scan of an aluminum disk. Several of the peaks in Figure 3.1.05 (b) occur close to where the model predicts they would, but there are several small, wide peaks that are unaccounted for by the model. Some of these small peaks occur near larger peaks like the first and third peak in Figure 3.1.05 (b). This may indicate a layer of another phase, possibly a reaction with the open air, but this is not seen as clearly in samples B and C. The satellite peaks may be an indicator of defects in the case of cylindrical specimens [ASTM standard E 2001-98 1999], which S-LLZO-92314-A was. For axisymmetric specimens, such as a cylindrical disc, some of the vibrational modes are degenerate, which means that two or more vibrational modes have the same frequency. However, if there is a defect in a axisymmetric specimen the redundant frequency may begin to

split and the RUS scan will show two close peaks where the model will predict one peak (for two distinct modes) [ASTM standard E 2001-98 1999].

3.1.4.4 Further Processing of S-LLZO-92314-B

Specimen S-LLZO-92314-B was cut and sanded again, this time as a rectangular parallelpiped, to provide a rough means of verifying the data in Figure 3.1.04 and Table 3.1.06. Analyzing a different geometry of the same specimen prevents the user from using the same pattern to match the peaks of the scan to the peaks of the model. Specimen S-LLZO-92314-B was also scanned using RUS after it was sanded a second time. The results of the RUS analysis seem to agree with the RUS analysis of the other specimens from the S-LLZO-92314 billet. The results are shown in Table 3.1.07 (last two items) and Figure 3.1.06 (S-LLZO-92314-B.2 is represented by X symbols).

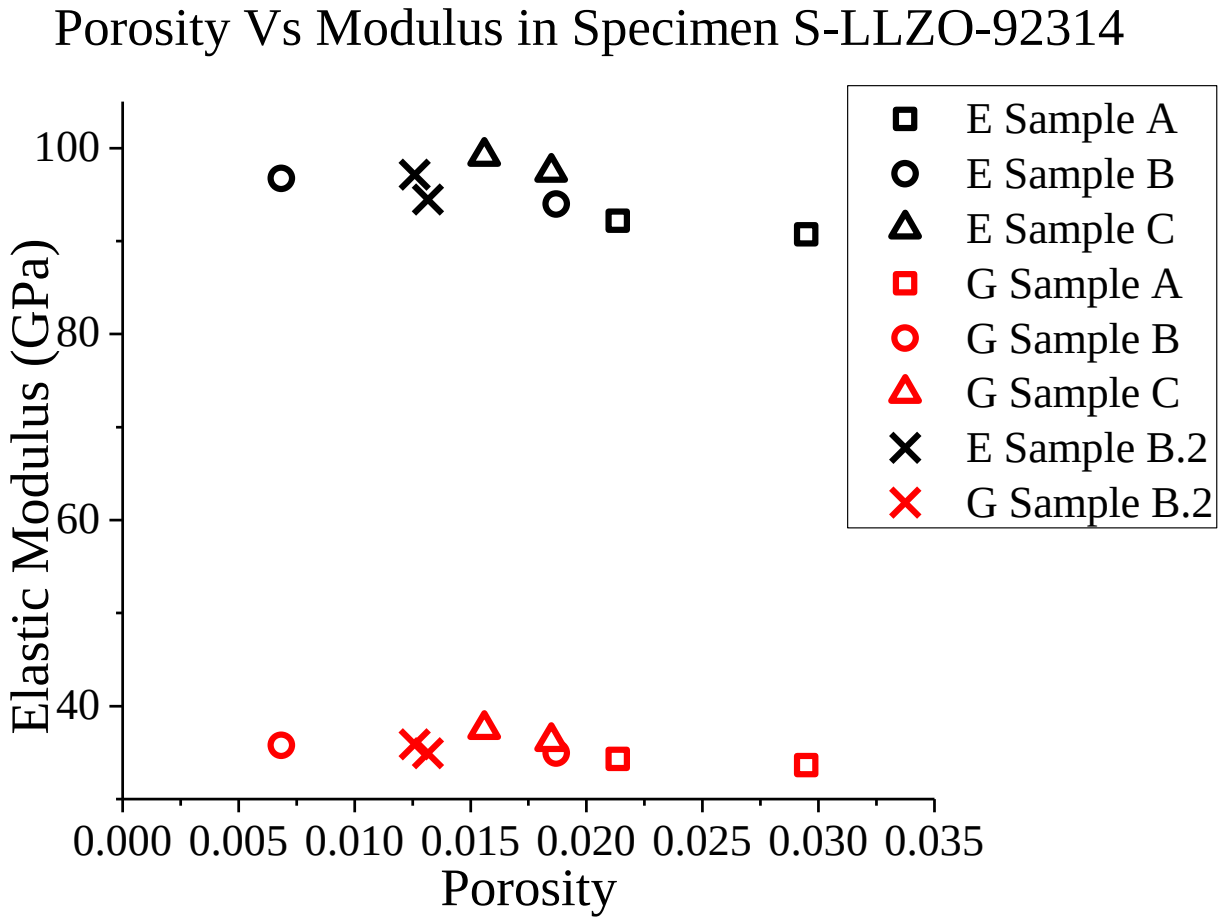

Figure 3.1.06 Young's modulus, black symbols, and shear modulus, red symbols, versus porosity for S-LLZO-92314. Each pair of data points shows a decrease in modulus and an increase in porosity after sanding.

The results of the RUS analysis on the rectangular parallelepiped (RP) were fairly consistent with the previous analysis. Table 3.1.09 and Table 3.1.10 show the difference between sample S-LLZO-92314 as a disk and as a RP, and compares before and after sanding specimens.

Table 3.1.09 Porosity (P) Young's modulus (E), shear modulus (G), Poisson's ratio (ν) RMS, peak count and geometry of sample S-LLZO-92314-B before being sanded as a disk and as a rectangular parallelepiped (RP)

	P	**E(GPa)**	**G(GPa)**	**ν**	**RMS**	**peaks**	**Geometry**
sample B pre sanding	0.007	96.74	35.76	0.353	0.65%	18	Disk
sample B.2 pre sanding	0.013	97.13	35.88	0.353	0.68%	10	RP
Percent difference		0.4%	0.3%	0.0%			

Table 3.1.10 Porosity (P) Young's modulus (E), shear modulus (G), Poisson's ratio (ν) RMS, peak count and geometry of S-LLZO-92314-B after being sanded as a disk and as a rectangular parallelepiped (RP)

	P	**E(GPa)**	**G(GPa)**	**ν**	**RMS**	**peaks**	**Geometry**
sample B post sanding	0.019	93.95	34.91	0.346	0.61%	20	Disk
sample B.2 post sanding	0.013	94.49	34.94	0.352	0.32%	11	RP
Percent difference		0.6%	0.1%	1.7%			

Table 3.1.09 shows less than 1 percent difference between the E, G and ν for the disk geometry and RP geometry of S-LLZO-92314-B before it was sanded. Table 3.1.10 shows for both the disk and the rectangular parallelepiped (RP) geometry, the elastic modulus dropped from the pre-sanding values in Table 3.1.09 after the specimen was sanded, and almost to the same values. Table 3.1.10 shows the post sanding E and G values for the RP and disk geometry were less than 1% different and the ν was only 1.7% different.

After sanding, the elastic moduli dropped and the porosity increased. The porosity of S-LLZO-92314-B.2 was constant at 1.3% before and after sanding. This value was between the before and after results of specimen S-LLZO-92314-B that it was cut from (7% and 1.9% porosity respectively). This may be due to the fact that the dimensions could be measured more accurately on a rectangular sample compared to the semi-oval shape of S-LLZO-92314-B (see Figure 3.1.03).

Higher grit sandpaper, which has a smaller grit size, was used to polish the surface of sample B.2, 1200 for sample B.2 versus 600 for samples A, B and C. The result of the RUS

analysis was not significantly different between sample B.2 and samples A, B and C (see Figure 3.1.06). Sanding the surface with higher grit (smaller grit size) sandpaper seemed to make higher frequency peaks identifiable, in the range of 200 to 270 kHz. This allowed the lowest frequency peak with the highest individual RMS to be removed from the model to improve the RMS of the overall model. Therefore, the analysis of S-LLZO-92314-B.2 that was sanded with 1200 grit sand paper, had the lowest RMS of any analysis of an S-LLZO-92314 sample, see Table 3.1.07. Sanding with a higher grit sandpaper to produce more identifiable peaks, as was done with sample S-LLZO-92314-B.2, could possibly be a means of improving RUS scans and would be worth exploring.

After the 1200 grit sanding, the 3 peaks with the highest frequency could be identified, but before sanding, the same peaks could not be identified (see Figure 3.1.07). The specimen was sanded with 600 and then 1200 grit sandpaper for the post sanding, whereas the pre sanding specimen was only sanded with 600 grit sandpaper. In Figure 3.1.07, the post sanding scan of S-LLZO-92314-B.2 has similar peaks as the pre sanding scan, except shifted to the left; this is because the sanding made the specimen smaller and therefore the resonance peaks would occur at lower frequencies. It is important to note that after the large peaks around 200 kHz in both scans of Figure 3.1.07, the amplitude drops. Figure 3.1.07 shows a few peaks over 200 kHz for the post sanding scan. Therefore, using 1200 grit sandpaper, instead of 600 grit sandpaper, allowed three more peaks to be identified.

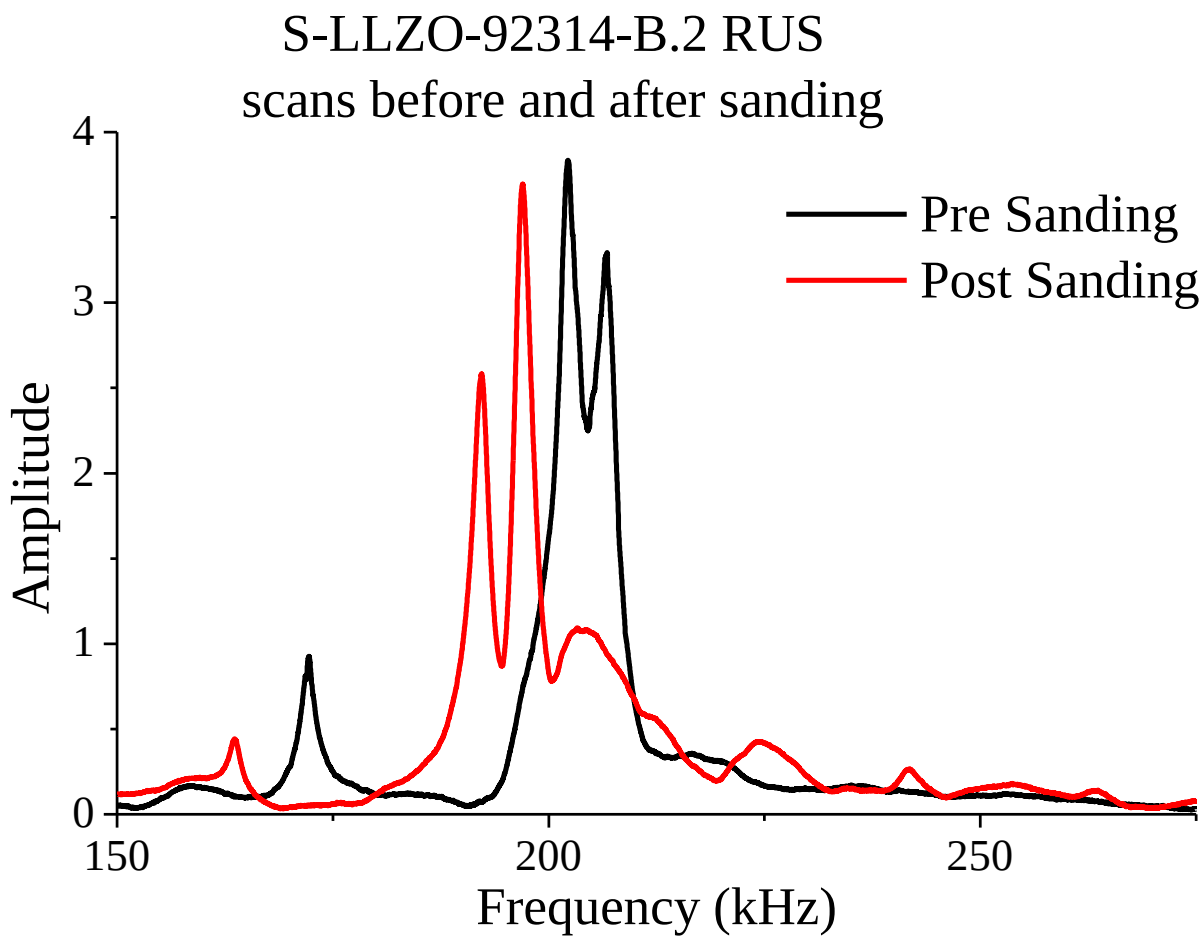

Figure 3.1.07 Sample S-LLZO-92314-B.2 RUS scans before and after it was sanded. The post sanding had a smoother surface because it was sanded with 1200 grit sandpaper, but because it was a smaller specimen, comparable peaks between the two scans will appear at lower frequencies.

Though the results of the RUS analysis of sample S-LLZO-92314-B.2 agree with the results of the RUS analysis of S-LLZO-92314-A, B and C, They are both lower in elastic moduli than what is expected for LLZO, namely the results found in Ni et al. [Ni 2012]. Ni reports E and G of 149.8 GPa and 59.6 GPa, respectively, for a sample with 3% porosity [Ni 2012]. There are many possible explanations as to why the current results are lower than the results reported in Ni et al. [Ni 2012]. Each will be discussed in detail in section 3.2.

3.2 Effects on Young's modulus by Various Mechanisms

3.2.1 Young's Modulus as a Function of Porosity

As stated in section 2.3.1, a starting guess for the RUS analysis could be obtained from Ni et al. [Ni 2012], but a closer estimate could be made with more experimental data. Ni et al. [Ni 2012] reports Young's and shear modulus of LLZO specimens at 3% and 6% porosity, which are listed in Table 2.3.1, but this leaves some uncertainty for samples that have porosity other than the samples listed in Table 2.3.1. As more results from analyzing specimens were obtained, a starting guess would be based on Equation 3.1.01 from Barsoum [Schmidt 2014; Rice 1998; Barsoum 1997c]:

$$R(P)=R_0*\exp(-B*P) \qquad 3.1.01$$

where R(P) is porosity dependent elastic modulus property, R_0 is an elastic modulus property of the material at theoretical 100% density, P is the porosity of the specimen and B is a fitting parameter unique to the material [Schmidt 2014]. Estimates for R_0 and B could be found from the data available in Ni et al. [Ni 2012], and values that were obtained from sample S-LLZO-62014.

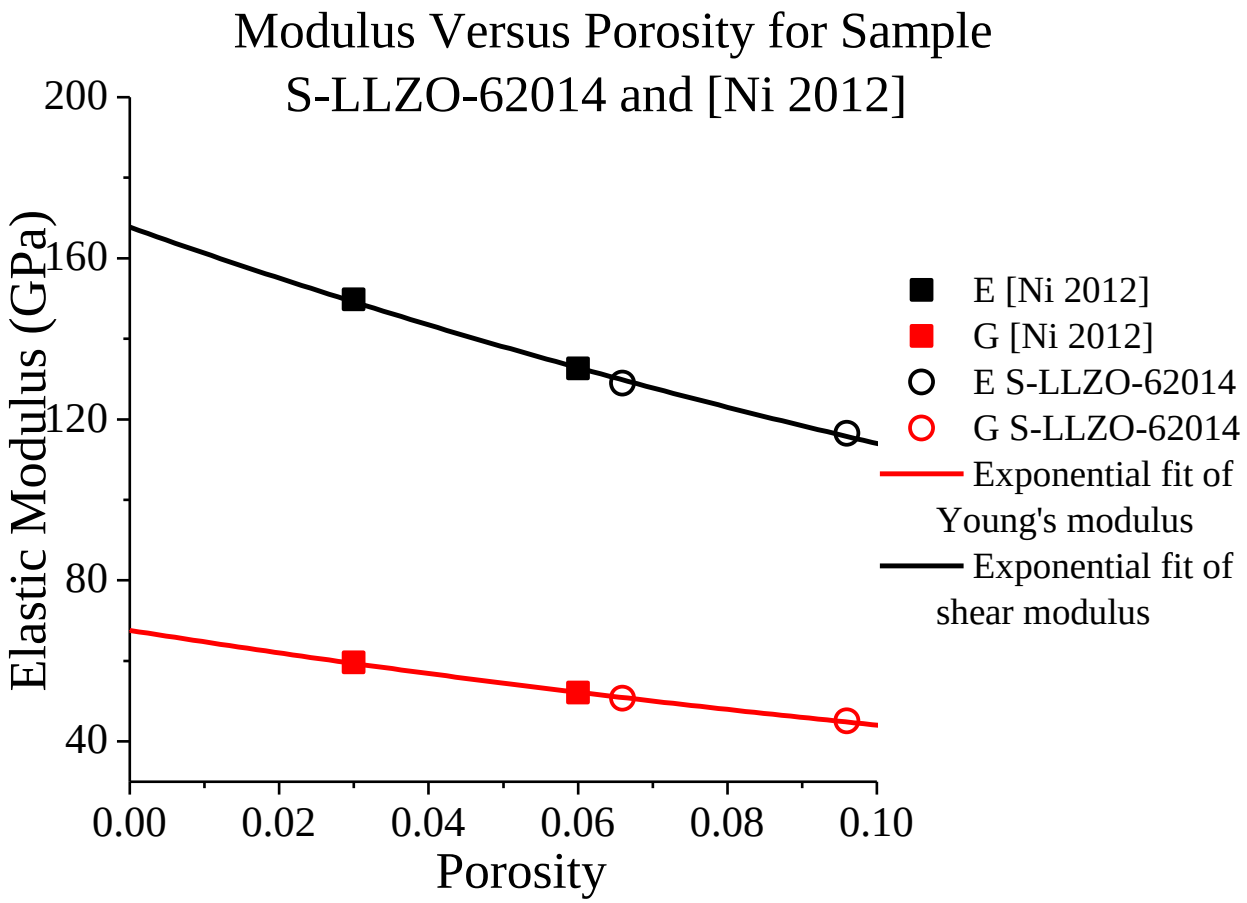

Figure 3.1.01 Young's modulus (E) and shear modulus (G) as plotted versus porosity for Ni et al. [Ni 2012] and S-LLZO-62014. The line is an exponential fit of Equation 3.1.01. The black line and symbols are Young's modulus and the red line and symbols are shear modulus

Table 3.2.01 Values of the exponential fit in Figure 3.1.01 according to Equation 3.1.01

	A_0	B	R^2
Young's modulus	167.16	3.816	0.997
shear modulus	67.40	4.236	0.998

The values listed in Table 3.2.01 and can be substituted into Equation 3.1.01 in place of A_0 and B to find initial guesses for the porosity dependent Young's modulus and shear, which yield

$$E(P)=167.16*\exp(-3.816*P) \quad (3.2.01)$$

$$G(P)=67.40*\exp(-4.236*P) \quad (3.2.02)$$

The porosity was easily measured, so one or both of these Equations were used to obtain starting values for the RUS analysis. The exponential fit in Figure 3.1.01 and Table 3.1.01, show a strong relationship between samples cut from a billet received on 6-20-14 (and labeled S-LLZO-62014-A and S-LLZO-62014-C) and the values published in Ni et al. [Ni 2012]. Therefore, Equations 3.2.01 and 3.2.02 were used in subsequent RUS analysis to obtain starting points. Unfortunately the elastic moduli of specimens S-LLZO-71014, S-LLZO-72914 and S-LLZO-92314 were much lower and did not fit the relationship of Equation 3.2.01 and Equation 3.2.02, shown in Figure 3.2.01.

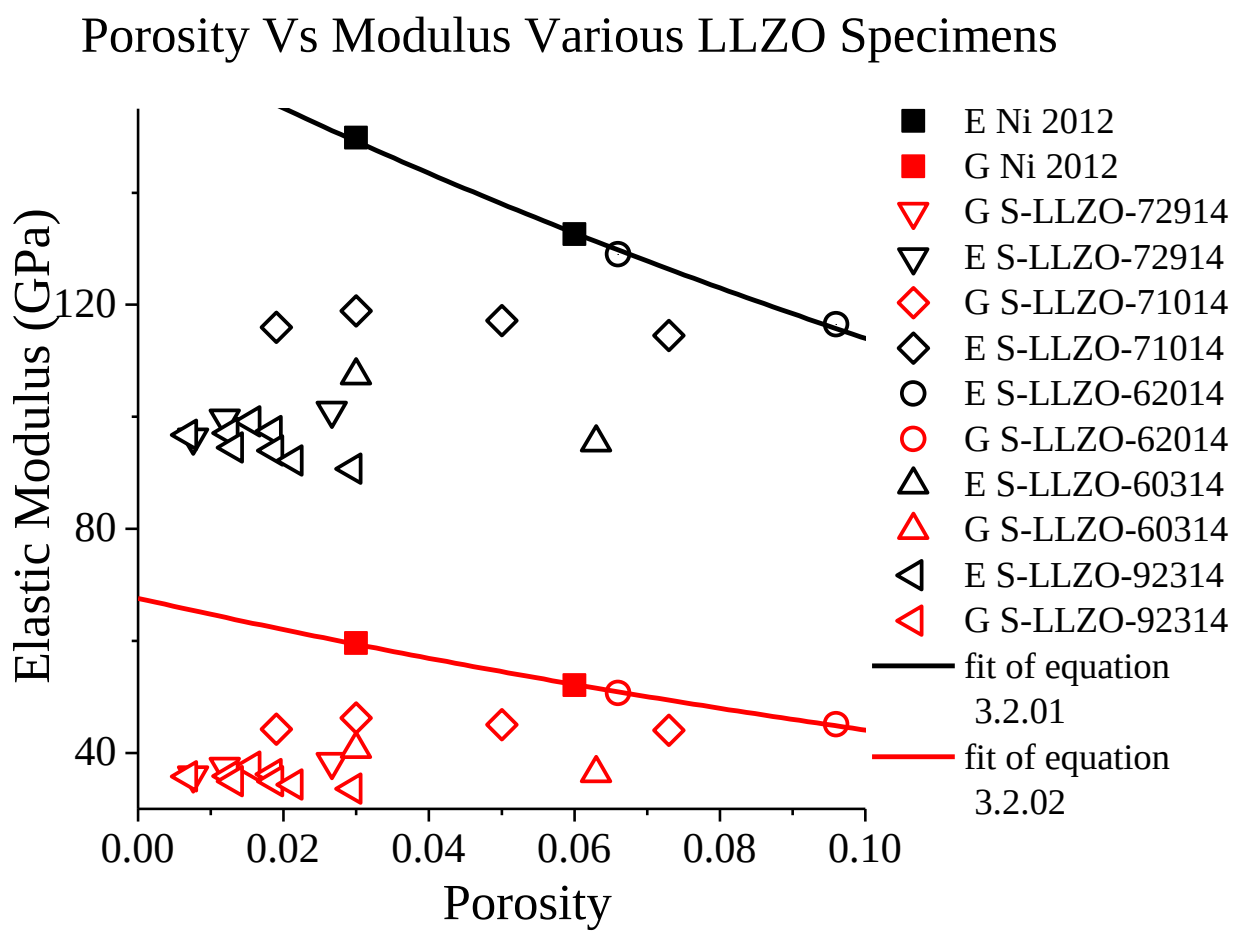

Figure 3.2.01 Young's modulus and shear modulus for all specimens in the study that could be analyzed, plotted against porosity. Filled squares represent Ni et al. [Ni 2012] data and opened symbols were experimentally determined during this study. Red symbols are shear modulus and black symbols are Young's modulus. The black and red line represents the least squares fit to Equations 3.2.01 and 3.2.02 respectively.

As shown in Figure 3.2.01, most of the specimens did not follow the relationships of Equations 3.2.01 and Equation 3.2.02 shown in figure 3.1.01. This limited the utility of the Equations for estimating initial guesses for the RUS analysis. Fortunately, when the first three peaks of the RUS scan were matched to the model the CylModel software recalculated the predicted peaks, which shifted the model down in frequency so that the model was in line with the RUS scan (see section 2.3.3 for more details).

Clearly the porosity can have a strong effect on the elastic moduli of the LLZO specimens.

3.2.2 Effects on Young's Modulus of Fiber Loading in Composite Materials

3.2.2.1 Models for Young's Modulus of Fiber Containing Composites

Dendrite formation inside a solid electrolyte may be fiber like. There are many models available to analyze a fiber/matrix composite. Most of the models in the literature were constructed with the intention of analyzing a matrix with reinforcement fibers that would enhance the elastic moduli. The scenario of lithium dendrites forming in LLZO is the opposite; the fibers have lower elastic modulus values and diminish elastic modulus values in the composite. Several models of elastic modulus for isotropic matrices with fiber inclusions, or a fiber/matrix composite, will be discussed here.

Table 3.2.02 Table of Equations to determine Young's modulus for a fiber/matrix composite

Name	Equation	Assumptions	Source
Rule of mixtures	$E_{CU} = V_m E_m + V_f E_f$	Assumes fibers are parallel to applied stress, This is an upper bound for an estimate	[Kingery 1976a]
Inverse Rule of mixtures	$\frac{1}{E_{CL}} = \frac{V_m}{E_m} + \frac{V_f}{E_f}$	Assumes fibers are perpendicular to applied stress, This is a lower bound for an estimate	[Kingery 1976a]
Christensen	$E_C = \frac{V_f}{6} E_f + (1 + (1 + \nu_m) V_f) E_m$	V_f <0.2 $G_f > G_m$ Poisson's ratio must be known	[Christensen 1972]
Manera	$E_C = V_f \left(\frac{16}{45} E_f + 2E_m\right) + \frac{8}{9} E_m$	Fibers are much longer than they are thick, 2 GPa<E_m<4 GPa, 0.1<V_f<0.4	[Manera 1977]
Curtis	$E_C = x * V_f E_f + V_m E_m$	*x* =1 if the fibers are perfectly aligned	[Curtis 1978]
Pan	$E_C = E_f \frac{V_f}{2\pi} + E_m \left(1 - \frac{V_f}{2\pi}\right)$	Assume: all fibers are same length, uniform fiber distribution, both materials behave elastically, fiber-fiber interaction is negligible	[Pan 1996]
Modified Halpin-Tsai with constant shape factor	$E_C = \frac{1 + C\eta V_f}{1 - \eta V_f} E_m \quad \eta = \frac{\alpha \frac{E_f}{E_m} - 1}{\alpha \frac{E_f}{E_m} + C}$ $C = \frac{2\lambda}{d}$	Assumes random fiber orientation	[Yeh 2006; Tai 2008]

E_c= Young's modulus of the fiber/matrix composite, E_m= Young's modulus of the matrix, E_f= Young's modulus of the fiber, V_m= Volume fraction of the matrix, V_f= Volume fraction of the fiber, *x*= orientation constant(*x* =1 when the fibers are parallel to the applied stress), ν_m= Poisson's ratio of the matrix, λ= length of fiber, d=thickness of fiber and α=1/3 if fibers are longer than the thickness of the test specimen or 1/6 if the fibers are shorter than the thickness of the test specimen

The rule of mixtures (ROM) and the inverse rule of mixtures (IROM) have been discussed in section 1.6.2. Together they serve as upper and lower bounds, respectively, of the Young's modulus of a fiber/matrix composite. Shear modulus can be found using the same Equations by replacing E_f and E_m with G_f and G_m, respectively.

Christensen developed his model to analyze commodity plastics that were enhanced with low cost fibers [Christensen 1972]. Through a detailed derivation with several assumptions, the Christensen Equation is derived

$$E_C = \frac{V_f}{6} E_f \ + (1 + (1 + \nu_m) V_f) E_m \qquad 3.2.03$$

where V_f is the volume fraction of the fiber, E_f is the Young's modulus of the fiber, V_m is the volume fraction of the matrix, E_m is the Young's modulus of the matrix and E_c is the Young's modulus of the composite. The Christensen Equation only applies when V_f is less than 0.2 and if the shear modulus of the fiber is greater than the shear modulus of the matrix [Christensen 1972].

To obtain Equation 3.2.03, Christensen assumes the shear modulus of the fiber is greater than the shear modulus of the matrix. In the case of the present study, lithium has a much lower shear modulus than LLZO, so the Christensen model is not applicable to the system with LLZO as the matrix and Li fibers (dendrites). Furthermore, the model is always increasing even if the fiber being added has significantly lower elastic modulus values.

The Manera model was developed to be simple but still very accurate [Manera 1977].

$$E_C = V_f \left(\frac{16}{45} E_f + 2E_m \right) + \frac{8}{9} E_m \qquad 3.2.04$$

where V_f is the volume fraction of the fiber, E_f is the Young's modulus of the fiber, V_m is the volume fraction of the matrix, E_m is the Young's modulus of the matrix and E_c is the Young's modulus of the composite.

The Manera model has several limitations as well. First it is assumed that the material in question has randomly oriented fibers, and that a material with fibers randomly oriented in three dimensions acts similar to a block made of layers with fibers randomly oriented in two-dimensions. Next, the fibers are much longer than they are thick. Lastly, the Young's modulus of the matrix is between 2 and 4 GPa and the volume fraction of the fiber must be between 0.1 and 0.4. The assumptions of Young's modulus of the matrix below 4 GPa also makes this model unsuitable for the present study.

The Curtis model can be explained as the rule of mixtures with an orientation constant added to the fiber term, as shown in Equation 3.2.05

$$E_C = x * V_f E_f + V_m E_m \qquad 3.2.05$$

where V_f is the volume fraction of the fiber, E_f is the Young's modulus of the fiber, V_m is the volume fraction of the matrix, E_m is the Young's modulus of the matrix, x is the orientation constant and E_c is the Young's modulus of the composite.

In their study, Curtis et al. physically tested carbon fiber in thermoplastic materials with destructive tests. As the stress is increased, cracks will start to form at the tips of the fibers, first in the fibers that aligned in the direction of the stress, then to more randomly aligned fibers [Curtis 1978]. As these cracks form, the fibers contribute less to the load bearing and other fibers, without cracks, will have to bear more of the applied stress [Curtis 1978]. The cracks will also grow as stress continues to be applied, but as the cracks progress further away from

the tip of the fiber, there will be less force acting to propagate the cracks, and the cracks will eventually reach a maximum [Curtis 1978].

Curtis et al. found that if the fibers are being added to reinforce the material, longer fibers will enhance the mechanical properties more than short fibers [Curtis 1978]. When all the fibers are parallel to the applied stress, x =1, which reduces the Equation to the rule of mixtures. Thus, the modulus of the composite reaches a maximum when all the fibers are parallel to the applied force [Curtis 1978]. x can be experimentally determined after results are obtained, but Curtis does not offer a first principles method for solving for x.

Sandler [Sandler 2002] offers a similar expression to Equation 3.2.05 called the Krenchel expression

$$E_C = \eta_l \eta_o * V_f E_f + V_m E_m \qquad 3.2.06$$

where η_l and η_o are the length correction factor and the orientation efficiency factor, and can be represented by the Equations [Hull 1981]

3.2.07 $$\eta_l = \left(\frac{2G_m}{E_f r^2 \ln\left(\frac{R}{r}\right)} \right) \quad \text{and} \quad \eta_o = \sum \Delta a_f cos\cos^4(\varphi) / a_f \qquad 3.2.08$$

where G_m is the shear modulus of the matrix, E_f so the Young's modulus of the fiber, r is the radius of the fiber, R is half of the inter fiber spacing, φ is the angle between the fiber and the direction of the applied load, a_f is the cross sectional area of a fiber and Δa_f is the total cross section area of a group of fibers with the same radius.

The complexity of the Krenchell Equation quickly diminishes the simplicity of the Curtis model. However, values for η_l and η_o have been determined for certain cases. If it can be

assumed that $\eta_l * \eta_o$ in Equation 3.2.06 is equal to *x* in Equation 3.2.05, Table 3.2.03 can be used [Hull 1981; Sandler 2002]

Table 3.2.03 values of *x* for the Curtis model based on η_l and η_o from the Krenchell expression [Hull 1981; Sandler 2002]

			η_l		
		aspect ratio	1000	100	10
		value of η_l	1	0.9	0.2
fiber orientation	**value of η_o**	**values for x**			
aligned	1		1	0.9	0.2
random 2D	0.375		0.375	0.3375	0.075
random 3D	0.2		0.2	0.18	0.04

η_o

Table 3.2.03 shows that *x* in the Curtis model (Equation 3.2.05) is a function of fiber orientation and aspect ratio of the fiber.

The Pan model is also similar to the rule of mixtures [Pan 1996].

$$E_C = E_f \frac{V_f}{2\pi} + E_m \left(1 - \frac{V_f}{2\pi}\right) \qquad 3.2.09$$

where V_f is the volume fraction of the fiber, E_f is the Young's modulus of the fiber, V_m is the volume fraction of the matrix, E_m is the Young's modulus of the matrix and E_c is the Young's modulus of the composite.

The assumptions for this form of the Pan model are: all fibers are uniform length; there is a uniform fiber distribution; fiber to fiber interaction is negligible; and both the fiber and the matrix materials must behave elastically. This model is applicable for Poisson's ratio by replacing E_c with ν_c, E_m with ν_m and E_f with ν_f. To find shear modulus of an isotropic material using the Pan model, Young's modulus and Poisson's ratio must first be found, then Equation 3.2.10 can be used

$$G_C = \frac{E_c}{2(1+\nu_c)} \qquad 3.2.10$$

where G_c is the shear modulus of the composite, E_c is the Young's modulus of the composite and ν_c is the Poisson's ratio of the composite phase.

There are several forms of the Halpin-Tsai Equation that can be used to predict the elastic moduli, a particularly useful form is the modified Halpin-Tsai model with a constant shape factor [Yeh 2006; Tai 2008]

$$E_C = \frac{1+C\eta V_f}{1-\eta V_f}E_m \quad \eta = \frac{\alpha\frac{E_f}{E_m}-1}{\alpha\frac{E_f}{E_m}+C} \quad C = \frac{2\lambda}{d} \qquad 3.2.11$$

where E_C is the Young's modulus of the composite, E_m is the Young's modulus of the original matrix, E_f the is Young's modulus of the fiber phase, V_f is the volume fraction of the fiber phase, V_m is the volume fraction of the original matrix phase, λ is the length of the fiber, d is the thickness or diameter of the fiber.

Despite how the complicated the structure of Equation 3.2.11 is, it is actual a rather general Equation. As *C* becomes very large, Equation 3.2.11 reduces to the rule of mixtures (Equation 1.6.05) and if *C* approaches zero, Equation 3.2.11 reduces to the inverse rule of mixtures (Equation 1.6.06) [Islam 2011]. Still, the modified Halpin-Tsai model with a constant shape factor Equation is useful for an estimate of elastic moduli of a fiber loaded material.

The α term in Equation 3.2.11 will have one of two values: 1/3 if the fibers are longer than the specimen is thick or 1/6 if the fibers length fits within the thickness of the specimen. The addition of the α term is one of the features that makes the modified Halpin-Tsai model different from the Halpin-Tsai model, however the main difference is the shape factor [Tai 2008]. Equation 3.2.11 has a constant shape factor, *C*. The modified Halpin-Tsai could have an

exponential shape factor, ξ, which has fitting parameters based on experimental data. However the fitting parameters are unique to the set of data being analyzed, rather than being based on first principles. Therefore ξ for the modified Halpin-Tsai model will not be used here. Instead the constant shape factor will be used, because it can be physically measured from the length and width of the fibers. Measuring the length and width of the fibers is not an easy task, but it is possible. The constant shape factor, C, will cause less and less change to the elastic moduli as it increases, see Figure 3.2.02.

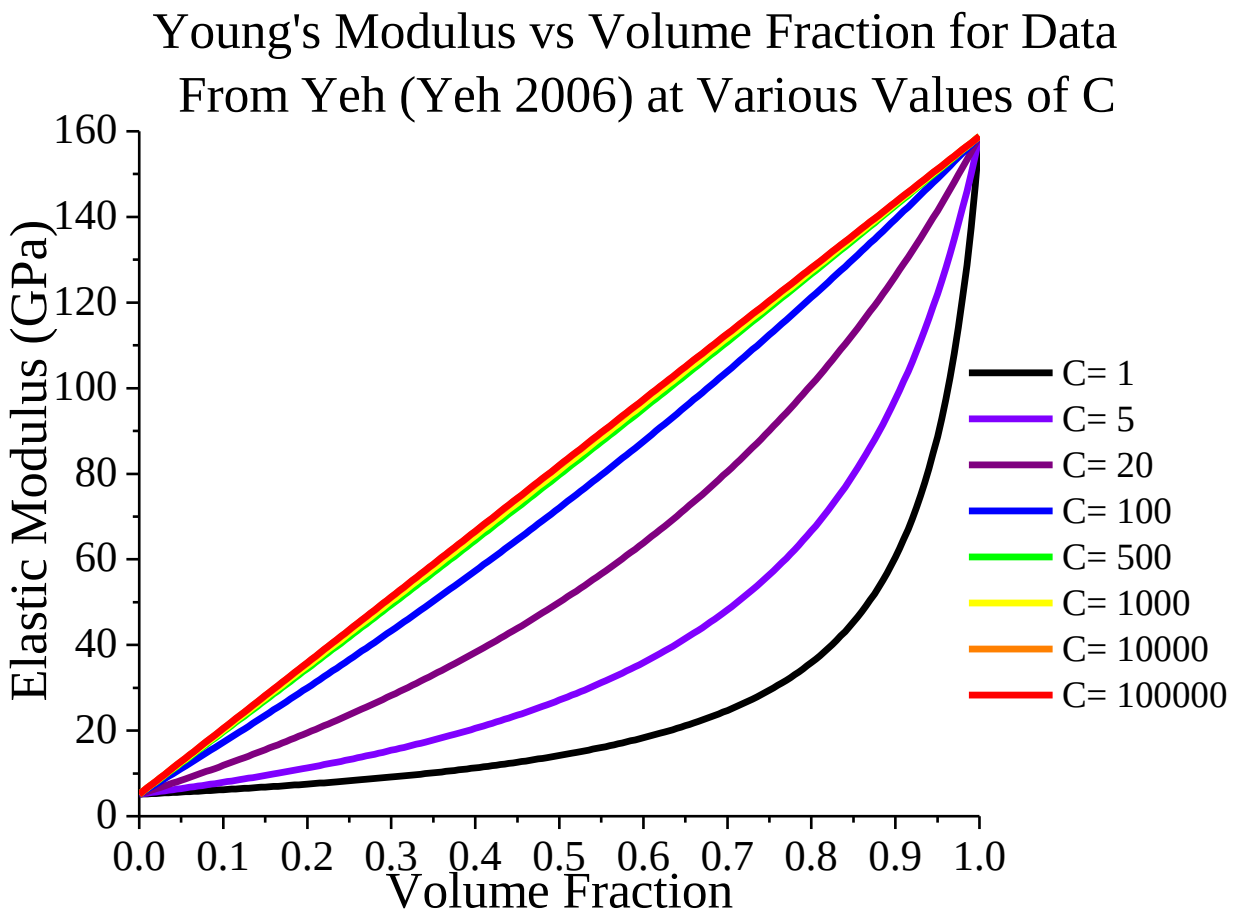

Figure 3.2.02 Experimental data from Yeh [Yeh 2006] plotted using different *C* values, where *C* is twice the ratio of length over width of a fiber.

In Equation 3.2.11 as the ratio of the length to width of a fiber increases, so does the value of the constant shape factor, C. Figure 3.2.02 plots Young's modulus versus volume

fraction for Yeh [Yeh 2006] using Equation 3.2.11. When all other factors are held constant, if *C* increases, the relationship becomes more linear, as shown in Figure 3.2.02. For *C* greater than 500, the slope is almost exactly the same [Yeh 2006], especially at volume fractions below 0.10.

Figure 3.2.02 is plotted according to Equation 3.2.11 and using data from Table 3.2.04. Each plot in Figure 3.2.02 uses the same values except the value of C.

Table 3.2.04 data and assumptions used to plot Figure 3.2.02

Parameter	**Value/assumption used**
composite description	phenolic epoxy reinforced with multi-walled carbon nanotubes [Yeh 2006]
Young's modulus of matrix (E_m) (GPa)	5.13 [Yeh 2006]
Young's modulus of fiber (E_f) (GPa)	953 [Yeh 2006]
Matrix Possion's ratio (ν_m)	N/A
Fiber alignment	Random orientation [Yeh 2006]

3.2.2.2 Plots for Young's Modulus of Fiber Containing Composites

The models in Table 3.2.02 were chosen because they are applicable to the analysis of fiber/matrix composite systems, and therefore may be applicable to dendrites in LLZO. Some of the discussed models are displayed in Figure 3.2.03. The data was taken from Yeh [Yeh 2006]. The matrix was a phenolic epoxy with a Young's modulus of 5.13 GPa, and the fibers were multi-walled carbon nanotubes with an estimated Young's modulus of 953 GPa. It was assumed that the fibers were dispersed and oriented in all directions [Yeh 2006]. The mean length of the fibers was 17.57 micrometers and the mean diameter was 23.63 nanometers [Yeh 2006], thus a length to width ratio of over 744. A summary of the data used in Figure 3.2.03 is available in Table 3.2.05.

The values on the x-axis were originally given in weight percent, but could be converted to volume fraction using the formula provide in Yeh [Yeh 2006]

$$V_f = \frac{\rho_f W_f}{\rho_f - \rho_f W_f + \rho_m W_f} \qquad 3.2.13$$

where W_f is the weight fraction of the fiber, V_f is the volume fraction of the fiber and ρ_f is the density of the fiber and ρ_m is the density of the matrix. Values for these variables can be found in Yeh [Yeh 2006].

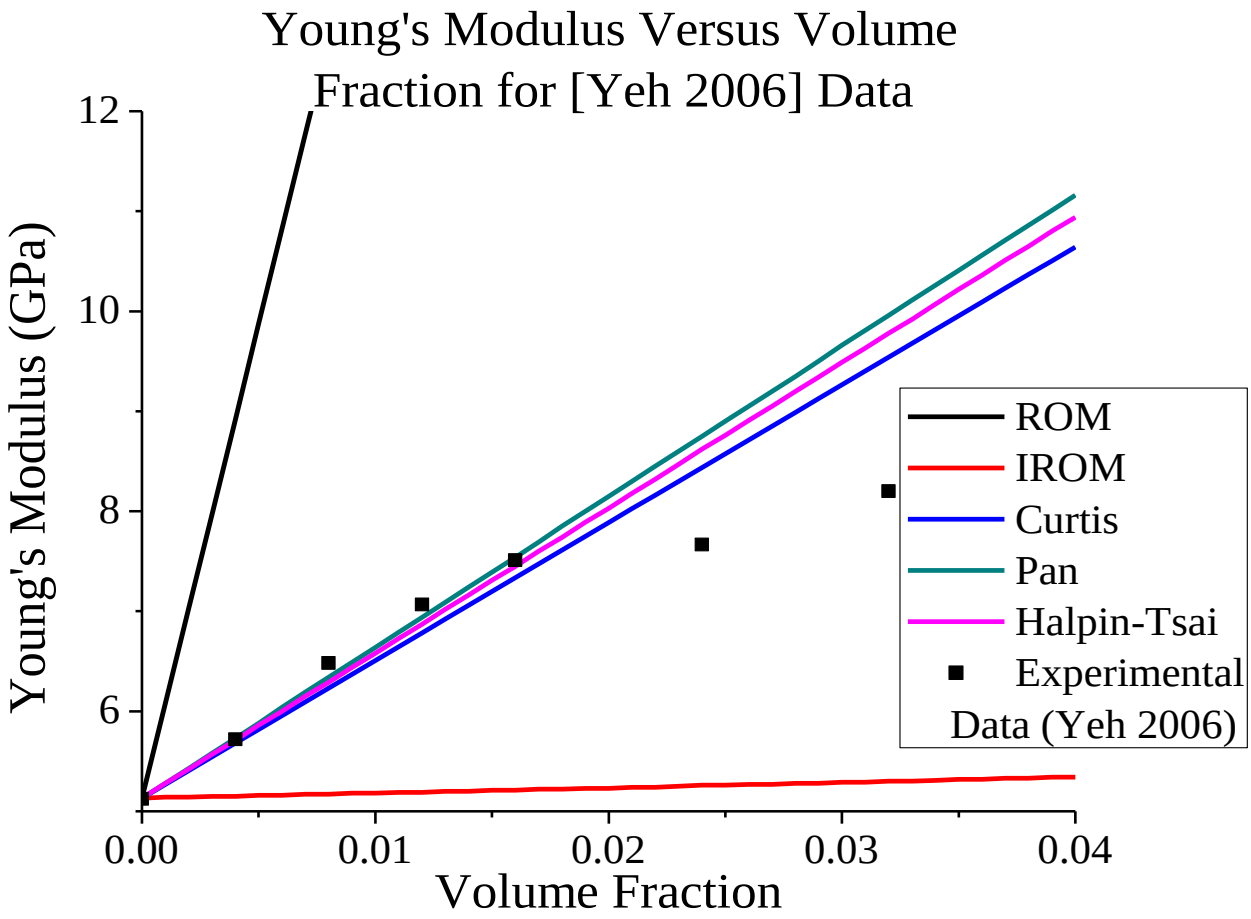

Figure 3.2.03 Young's modulus versus fiber volume. The experimental data is from [Yeh 2006] ROM is the rule of mixtures model and IROM is the inverse rule of mixtures model.

Table 3.2.05 Data and assumptions used to plot Figure 3.2.03. This table is similar to table 3.2.04, but now considers aspect ratio, and therefore *C* to be constant.

Parameter	**Value/assumption used**
composite description	phenolic epoxy reinforced with multi-walled carbon nanotubes [Yeh 2006]
Young's modulus of matrix (E_m) (GPa)	5.13 [Yeh 2006]
Young's modulus of fiber (E_f) (GPa)	953 [Yeh 2006]
Matrix Possion's ratio (ν_m)	N/A
Fiber alignment	Random orientation [Yeh 2006]
Fiber aspect ratio	Average ~744 [Yeh 2006]

The Curtis model requires a value for the orientation constant. Using Equation 3.2.14

$$x = (E_c - E_m V_m)/(E_f V_f) \qquad 3.2.14$$

x was calculated for each data point. When *x*= 1, all fibers are perfectly aligned in the direction of the applied stress. The average *x* for the data points in Figure 3.2.03 was 0.15, meaning there was little alignment of the fibers. The average value of *x* was used in the Curtis model.

The modified Halpin-Tsai model in Figure 3.2.03 uses a *C* value of 1,487. The value of *C* is dependent on the ratio of length to width of the fiber, and *C* values of more than 500 do very little to alter the value of E_c [Yeh 2006]. α is known to be 1/6 for this data set [Yeh 2006].

Figure 3.2.2 shows a data set from Sandler [Sandler 2002] with the same models to compare the data.

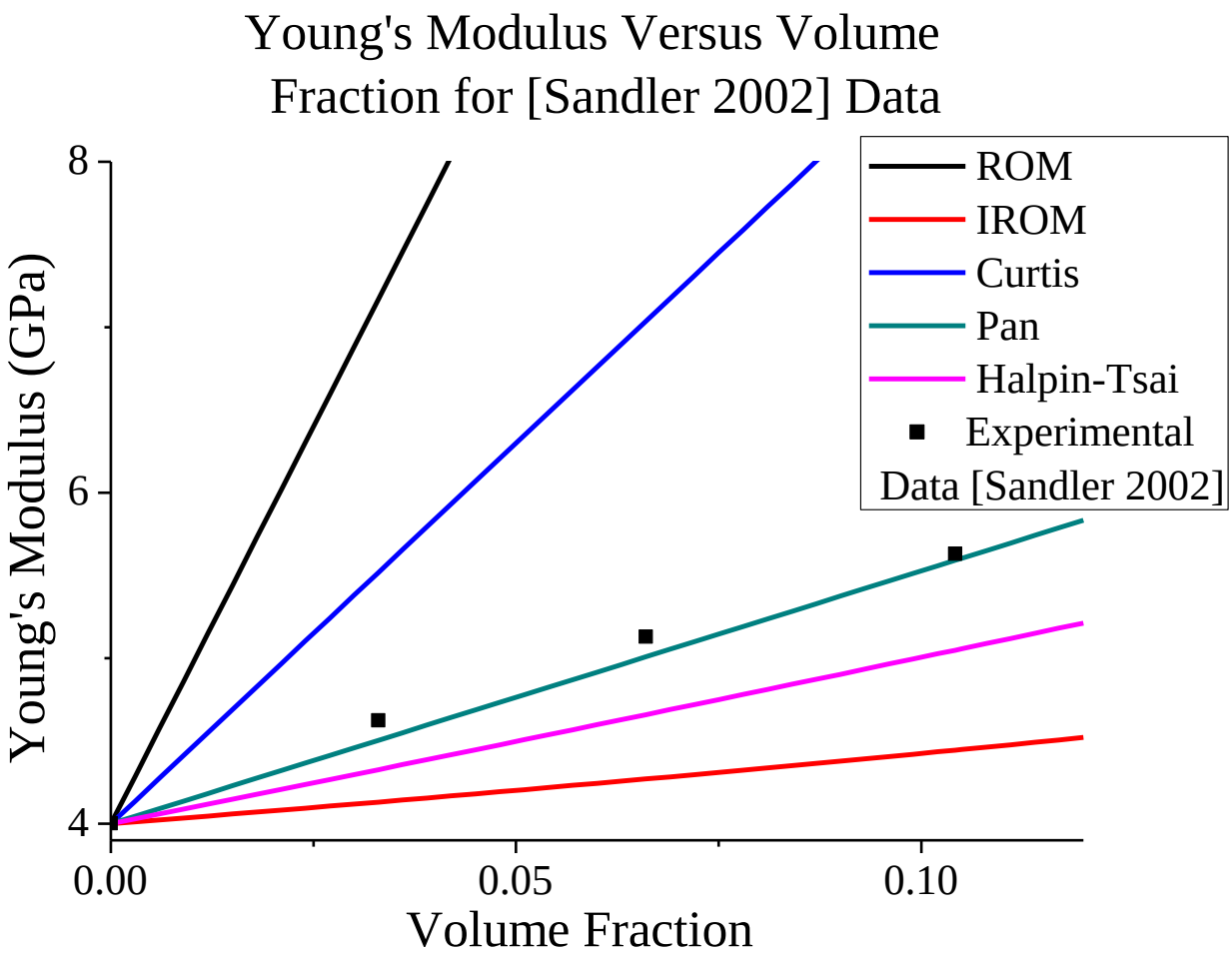

Figure 3.2.04 Young's modulus versus fiber volume fraction using data from Sandler [Sandler 2002]. ROM is the rule of mixtures model and IROM is the inverse rule of mixtures model.

Table 3.2.06 Data and assumptions used to plot Figure 3.2.04

Parameter	**Value/assumption used**
Composite description	poly(ether ether ketone) with carbon naonfiber reinforcement [Sandler 2002]
Young's modulus of matrix (E_m) (GPa)	4.0 [Sandler 2002]
Young's modulus of fiber (E_f) (GPa)	100 [Sandler 2002]
Matrix Possion's ratio (ν_m)	N/A
Fiber alignment	Mostly ordered with some random orientation [Sandler 2002]
Fiber aspect ratio	500 (not explicitly stated, fiber aspect ratio started around 10^3 but may have been shortened during processing [Sandler 2002])

In the Sandler study, the Young's modulus of the matrix with no fiber was 4.0 ±0.1 GPa, but the Young's modulus of the fiber was uncertain but estimated to be in the range 19 to 280 GPa but most likely around 100 GPa [Sandler 2002], so for the models in Figure 3.2.04 the Young's modulus was assumed to be 100 GPa. The fibers were mostly aligned in the direction of the tensile stress. In the injection moulding process most fibers are aligned in the direction of the extruder except in the center of the specimen where there is some misalignment [Sandler 2002]. However, Sandler did not estimate the degree of alignment of the fibers [Sandler 2002]. The lack of a specified degree of alignment creates some uncertainty for the Curtis model where an orientation factor is needed. Because no in-depth description of fiber orientation is offered in Sandler [Sandler 2002], an orientation factor of 0.5 was chosen. This would imply a moderate to high degree of alignment (see Table 3.2.03).

The aspect ratio of the as received fiber was around 10^3 [Sandler 2002].The effective load bearing aspect ratio could be as low 10, [Sandler 2002] but this could be due to low modulus of the fiber material or misoriented fibers. This leaves a lot of room for interpretation of what to use for the *C* value in the modified Halpin-Tsai model. Because carbon nanotubes have very high elastic modulus and are very small, it was assumed they would experience minimum degradation during the processing of the composite material. So a high value was chosen and because values over 500 do little to change the model, 500 was used for the value of *C* in the modified Halpin-Tsai model [Yeh 2006].

With the assumptions being stated, a discussion of the models in Figure 3.2.04 can begin. Again, the ROM and the IROM form upper and lower bounds for the other models in Figure 3.2.04. The best fit seems to be from the Pan model which doesn't require any assumptions or additional measurements beyond modulus and volume fraction of the matrix

and fiber material. The modified Halpin-Tsai model is lower than the experimental data. α and *C* could be changed so that the model would better fit the experimental data, but increasing α would imply the fibers are longer than the thickness of the test specimens, which was not the case [Sandler 2002], and increasing *C* even a hundred fold will only have negligible changes. The modified Halpin-Tsai model may still be correct if the Young's modulus of the fiber is higher than 100 GPa which was used in the prediction, but Sandler's estimate was around 100 GPa so that is what was used [Sandler 2002]. Lastly, the Curtis model is much too high. If *C* is set to 0.20, the line will be much closer to the experimental data.

A third data set is available from figure 5 in Manera [Manera 1977]. This data set is plotted in Figure 3.2.05 with several models. Table 3.2.07 list details of the composite and its components.

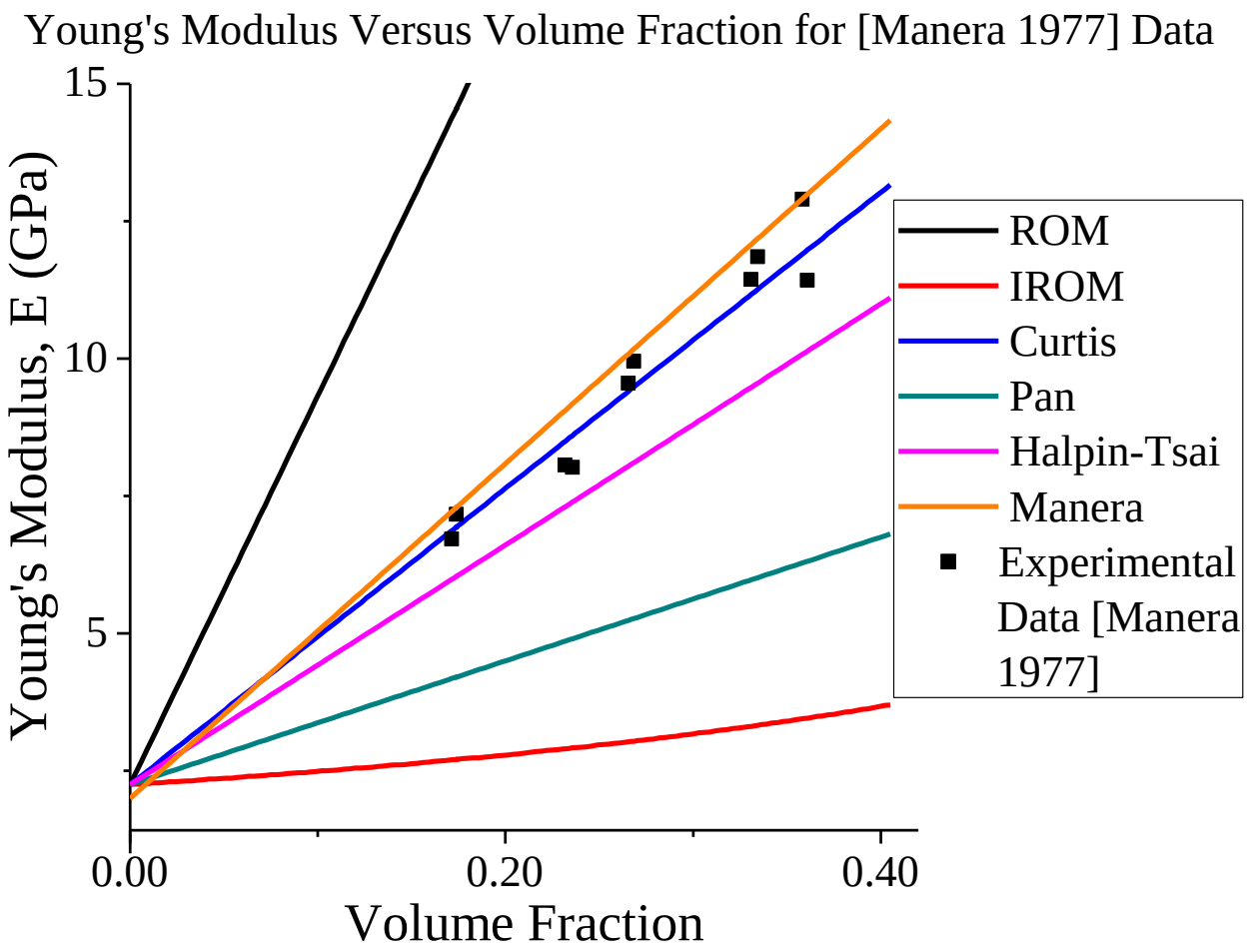

Figure 3.2.05 Young's modulus versus fiber volume fraction using data from Manera [Manera 1977]. ROM is the rule of mixtures model and IROM is the inverse rule of mixtures model.

Table 3.2.07 data and assumptions used to plot Figure 3.2.05

Parameter	**Value/assumption used**
composite description	Polyester resin with fiber glass reinforcement
Young's modulus of matrix (E_m) (GPa)	2.25 [Manera 1977]
Young's modulus of fiber (E_f) (GPa)	73 [Manera 1977]
Matrix Possion's ratio (ν_m)	0.4 [Manera 1977]
Fiber alignment	Random orientation [Manera 1977]
Fiber aspect ratio	Assumed to be greater than 300, with lengths ranging from 10 to 50 cm and widths ranging from 5 to 30 μm [Manera 1977]

The Young's modulus of the fiber is much higher than the Young's modulus of the matrix without any fiber added. The fibers are randomly oriented and assumed to be much longer than they are wide.

The ROM and IROM again provide upper and lower bounds for the data and the models. The Curtis model has the best fit, but this is by design. The Curtis model requires a value for the orientation constant which could, again, be found using Equation 3.2.14

$$x = (E_c - E_m V_m)/(E_f V_f) \qquad 3.2.14$$

Equation 3.2.14 results in an average *x* of 0.40. This value was used to plot the Curtis model in Figure 3.2.05 and that is why the Curtis model fits the best.

The Manera model has strict specifications for when the model can be applied. The data set plotted in Figure 3.2.05 fits these specifications, namely E_m must be between 2 and 4 GPa and the volume fraction of fiber, V_f, must be between 0.1 and 0.4. The Manera model is plotted in Figure 3.2.05 extends outside of these boundaries and it can be seen that the Manera model at V_f=0 does not equal the Young's modulus of the matrix. However, it can be clearly seen in Figure 3.2.05 the model fits fairly close to the data where the specifications are met.

The modified Halpin-Tsai model is also fairly close to the data set in Figure 3.2.05. One variable that needed to be assumed was the orientation factor, α.The orientation factor will be 1/3 when the fiber is longer than the thickness of the specimen and 1/6 when the fiber is shorter than the thickness of the specimen [Yeh 2006]. The fiber length is stated as 1 to 5 cm [Manera 1977]. The dimensions of the specimen for torsion testing were 3 cm diameter with a 3 mm thickness [Manera 1977]. If the specimens that were used to test elastic moduli were close to the 3 mm thickness, then α would be 1/3. Using α=1/3 makes the modified Halpin-Tsai model closer than if α=1/6 is used. It is ultimately an assumption that α=1/3 rather than 1/6, but it

seems to be a reasonable assumption given the fibers are greater than 1 cm in length and the specimen is 3 mm thick [Manera 1977].

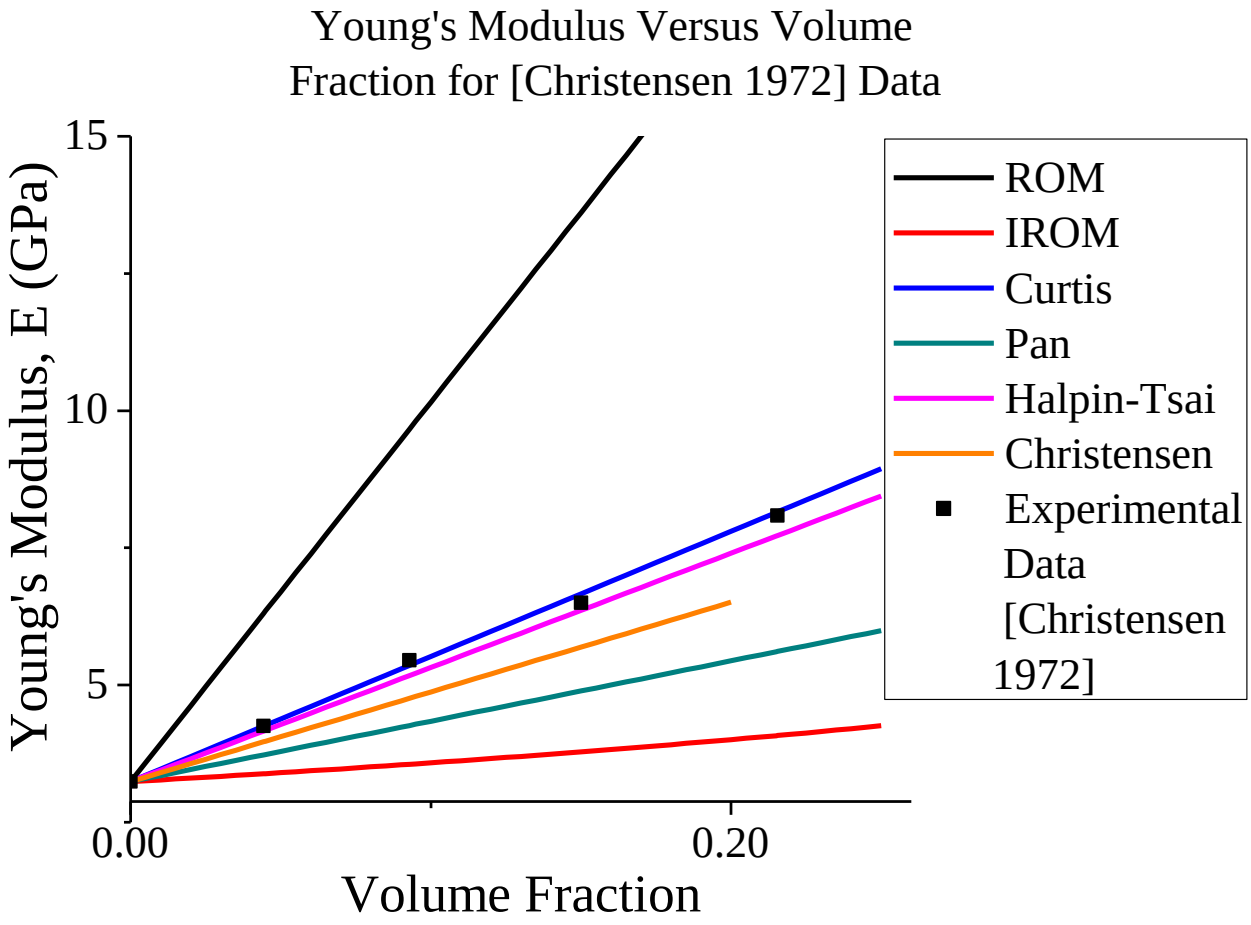

Figure 3.2.06 Young's modulus versus fiber volume fraction using data from Lee [Lee 1968]. ROM is the rule of mixtures model and IROM is the inverse rule of mixtures model. The Christensen formula stops where V_f =0.20 because the model is no longer valid above that

Table 3.2.08 data and assumptions used to plot Figure 3.2.06

Parameter	**Value/assumption used**
composite description	polystyrene with fiber glass addition
Young's modulus of matrix (E_m) (GPa)	3.2 [Lee 1968]
Young's modulus of fiber (E_f) (GPa)	72.4 [Lee 1968]
Matrix Poisson's ratio (ν_m)	0.32 [Lee 1968]
Fiber alignment	Random orientation [Lee 1968]
Fiber aspect ratio	675, Length of 1/4 inches and diameter of 0.00037 inches

Figure 3.2.06 shows a data set from Christensen [Christensen 1972], that was experimentally determined by Lee [Lee 1968]. The study done by Lee [Lee 1968] involved reinforcing polymer materials with fiber glass and the composite was tested for tensile and flexural strength. The composite's fiber would have a random orientation, which wouldn't be ideal for strength properties, but the material could be mass produced cheaper and faster than materials that had fibers all aligned in one direction [Lee 1968].

As in the previous figures, the ROM and IROM form the upper and lower bounds, respectively. The Curtis model's orientation factor, *x*, was chosen to be 0.36 because the average *x* calculated from the 4 non-zero data points in Figure 3.2.06 was 0.36. The Christensen model is included in Figure 3.2.06. The Christensen model has requirements that have made it unsuitable for the data sets in Figure 3.2.03 through Figure 3.2.05; namely the Poisson's ratio of the unaltered matrix must be known and the V_f must be less than 0.20. Because the volume fraction must be less than 0.20, the line plotting the Christensen model in Figure 3.2.06 ends at 0.20. For the modified Halpin-Tsai model, the aspect ratio was approximately 675 [Lee 1968]. The samples that were tested in the study were 3.12 mm thick, and because the fibers were twice this length, the orientation factor, α, for the modified Halpin-Tsai model was 1/3. The Pan model does not seem to fit well to this data. The Christensen, modified Halpin-Tsai and the Curtis model all fit rather well to the data set.

Two data sets were available from Kriz et al.[Kriz 1979]. The data was experimentally determined by Dean and Turner using ultrasonic transmission techniques [Dean 1973].

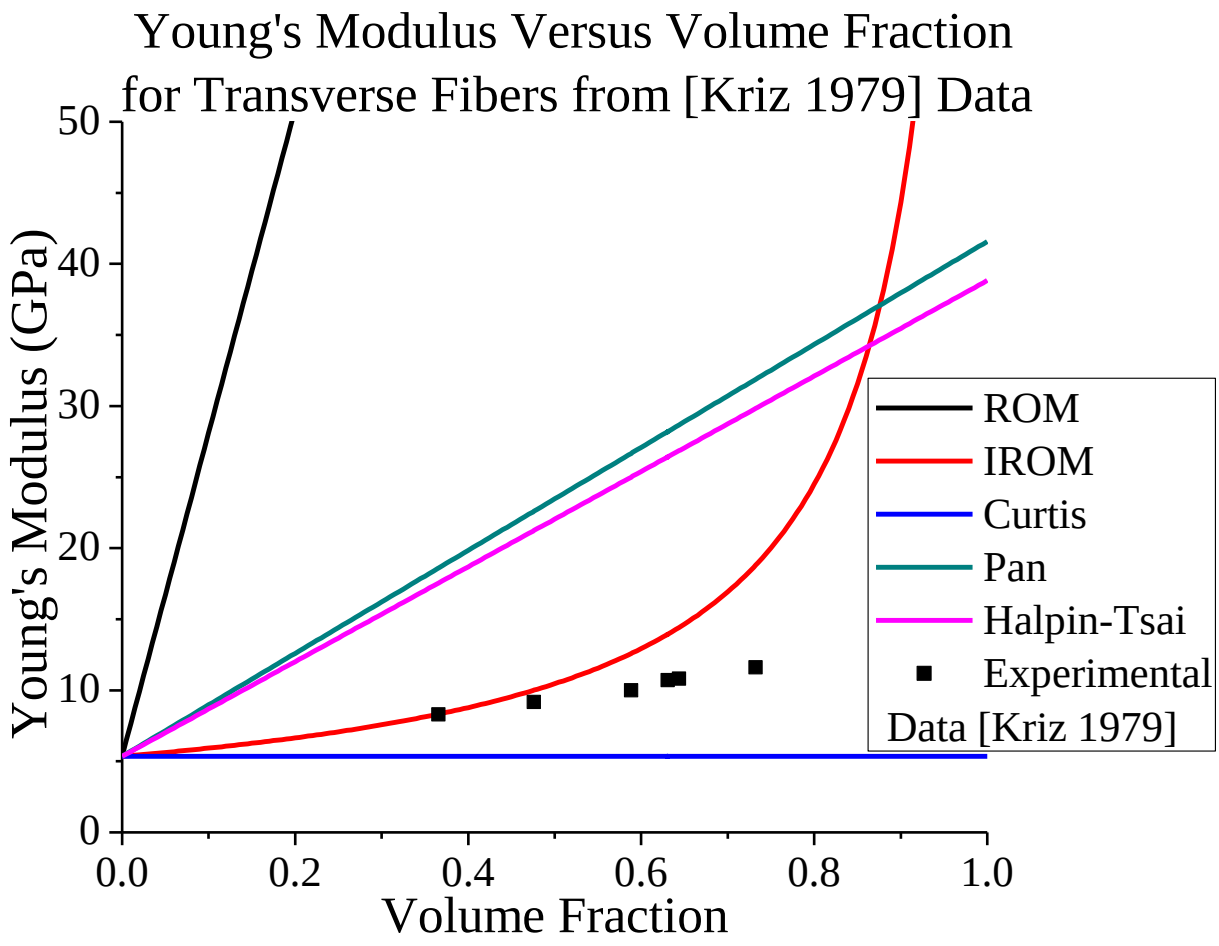

Figure 3.2.07 Young's modulus versus fiber volume fraction using data in Kriz [Kriz 1979] and Dean and Turner [Dean 1973]. ROM is the rule of mixtures model and IROM is the inverse rule of mixtures model.

The materials that were tested were a composite of epoxy with carbon fiber aligned uniformly in one direction of the material ranging from V_f equal to 0.3 to 0.7 V_f that were cut into specimens with dimensions of 10 mm by 40 mm by 2.5 mm [Dean 1973]. The first data set is plotted in Figure 3.2.07 with some details of the materials listed in Table 3.2.09.

Table 3.2.09 data and assumptions used to plot Figure 3.2.07 data originally from Dean and Turner [Dean 1973]

Parameter	**Value/assumption used**
composite description	Isotropic epoxy resin with graphite fibers (Ciba LY558 epoxy resin with modmor carbon fiber)[Dean 1973]
Young's modulus of matrix (E_m) (GPa)	5.35 [Kriz 1979]
Young's modulus of fiber (E_f) (GPa)	233 [Kriz 1979]
Matrix Possion's ratio (ν_m)	0.354 [Kriz 1979]
Fiber alignment	Measured transverse to fiber orientation [Kriz 1979]
Fiber aspect ratio	[Kriz 1979] not specified, assumed to be much longer than the diameter

The second data set from Kriz is plotted in Figure 3.2.08 with further details of the materials listed in Table 3.2.10. The main difference of the two data sets in the orientation of the fibers; Figure 3.2.07 is measured in the longitudinal direction of the fiber and Figure 3.2.08 is measured in the transverse direction of the fiber.

Figure 3.2.07 has fibers oriented in the transverse direction [Kriz 1979]. The Young's modulus of the composite is noticeably lower in the transverse direction (Figure 3.2.07) than in the longitudinal direction (Figure 3.2.08). In Figure 3.2.07 and Figure 3.2.08, the ROM and IROM form upper and lower bounds for the models, except the Curtis model in Figure 3.2.07, but not bounds for the data. The ROM, IROM, Pan and modified Halpin-Tsai models are the same for Figure 3.2.07 and Figure 3.2.08. The aspect ratio of the fiber was not given in Dean and Turner[Dean 1973] or Kriz [Kriz 1979], but because the aspect ratio of fibers discussed so far have been large, it was assumed the aspect ratio of these fibers was also very large. The orientation factor,α, for the modified Halpin-Tsai model was assumed to be 1/6 implying the fibers were shorter than the thickness of the specimen[Yeh 2006] which was given as 2.5 mm [Dean 1973]. The only model that can explicitly include more than one fiber orientation is the Curtis model. In Figure 3.2.07 the Curtis model is given the minimum value of *x* it can have

without having a negative slope for E_c versus V_f. This minimum value of *x* is $E_m/E_{f,}$ which reduces the Equation to $E_c = E_{m.}$ In Figure 3.2.08 the Curtis model, is given a value of 0.95, because *x* is equal to one when the fibers are all aligned in one direction like in this data set, but then it would simply be equal to the ROM, so it was set to be slightly less so both models would be visible in the figure.

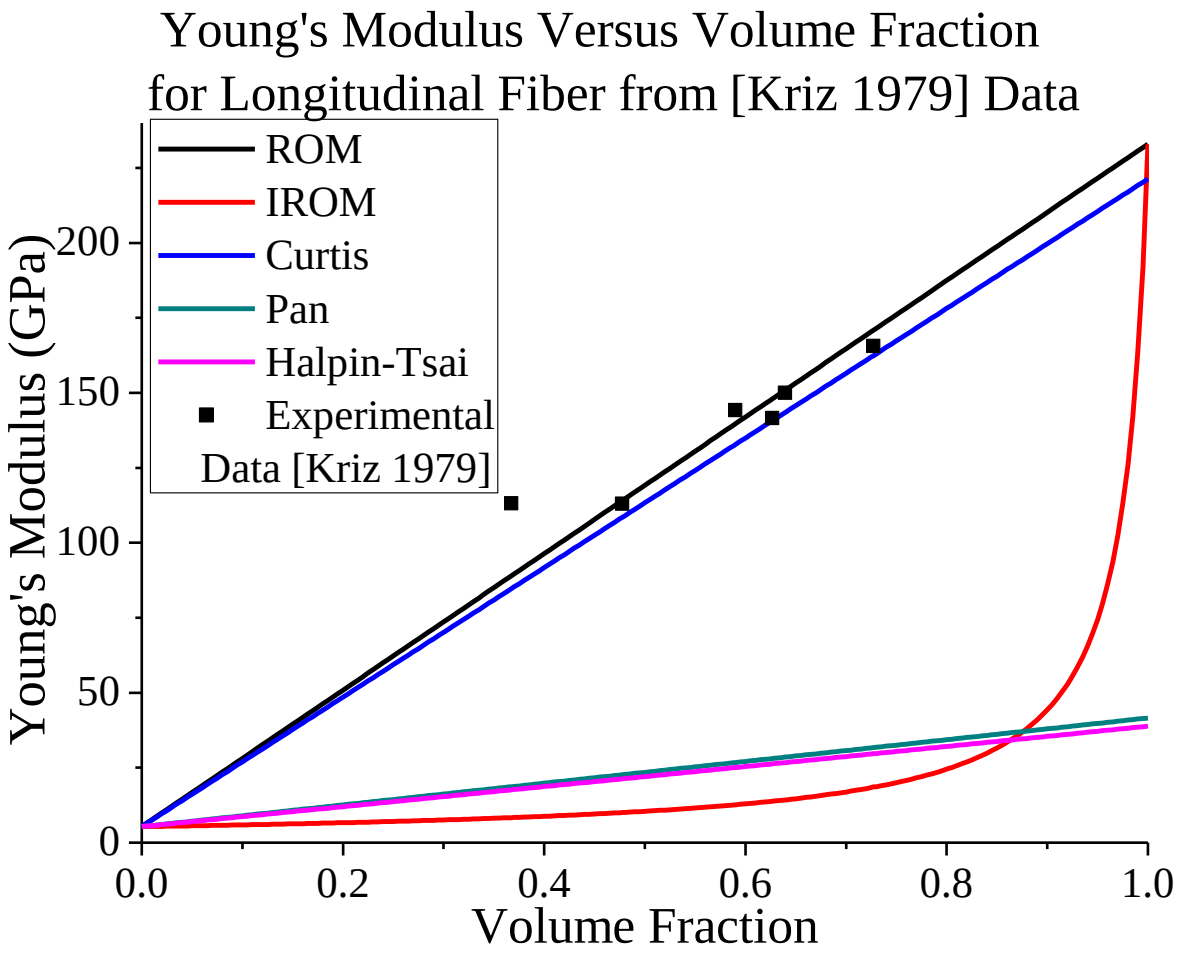

Figure 3.2.08 Young's modulus versus fiber volume fraction using data in Kriz[Kriz 1979] and Dean and Turner [Dean 1973]. ROM is the rule of mixtures model and IROM is the inverse rule of mixtures model.

Table 3.2.10 data and assumptions used to plot Figure 3.2.08 data originally from Dean and Turner [Dean 1973]

Parameter	**Value/assumption used**
composite description	Isotropic epoxy resin with graphite fibers (Ciba LY558 epoxy resin with modmor carbon fiber)[Dean 1973]
Young's modulus of matrix (E_m) (GPa)	5.35 [Kriz 1979]
Young's modulus of fiber (E_f) (GPa)	233 [Kriz 1979]
Matrix Possion's ratio (ν_m)	0.354 [Kriz 1979]
Fiber alignment	measured along length of fiber [Kriz 1979]
Fiber aspect ratio	[Kriz 1979] not specified, assumed to be much longer than the diameter

As seen in Figure 3.2.08 the ROM can be rather accurate for a composite material with fiber orientation in the longitudinal direction, but as seen in Figure 3.2.07 the IROM is not as close of an approximation for fiber composite materials in the transverse direction. The closest model for the data set in Figure 3.2.08 is the ROM model because the actual experiment fits very closely to the assumption that the fibers are aligned in the direction of the test. The closest model for Figure 3.2.07 is more difficult. The IROM model has an exponential curve. The data set does not seem to follow the exponential curve and looks more linear. According to Equation 1.6.06

$$\frac{1}{E_{CL}} = \frac{V_m}{E_m} + \frac{V_r}{E_r} \qquad 1.6.06$$

In Equation 1.6.06, if the V_f is equal to 1, the material should be completely made out of the fiber material and no matrix material. Therefore E_c at V_f equal to 1 should be equal to E_m. The data set in Figure 3.2.08 does not seem to follow Equation 1.6.06 and even appears to have a linear trend.

The data sets in Figure 3.2.07 and Figure 3.2.08 are the extremes of fiber orientation and show the limitations of the models. The exact aspect ratio and orientation factor for the modified Halpin-Tsai Equation are not critical to the discussion because the model is intended

for random oriented fibers [Yeh 2006], making it is unsuitable for data sets and experiments involving uniformly transverse or longitudinal alignment. So even if α and the aspect ratio were changed the modified Halpin-Tsai model would still be inaccurate in Figure 3.2.07 and Figure 3.2.08. The Pan model is also meant for composites with random fiber orientation so the model has similar results as the modified Halpin-Tsai and is also unsuitable for uniformly aligned fiber composites [Pan 1996].

The various data sets in Figure 3.2.03 through Figure 3.2.08 are quite different from one another, but it is worth comparing them in order to compare the effect fiber orientation has on the Young's modulus of a composite. Each data set for Figure 3.2.03 through Figure 3.2.08 has been roughly normalized using Equation 3.2.15 and plotted versus the volume fraction, V_f, in Figure 3.2.09.

$$E_N = \frac{(E_C - E_m)}{(E_f - E_m)} \qquad 3.2.15$$

where E_N is the normalized Young's modulus of the composite, which is unitless.

To obtain this normalization, first consider the rule of mixtures,

$$E_C = V_m E_m + V_f E_f \quad \text{(Rule of mixtures)} \qquad 1.6.05$$

Which can written as

$$E_C = (1 - V_f) E_m + V_f E_f \quad \text{(Rule of mixtures)} \qquad 1.6.05\text{ a}$$

The slope of the changes in Young's modulus of the composite versus volume fraction of fibers will be the partial derivative of Equation 1.6.05 a, with respect to volume fraction, V_f,

$$\frac{\partial E_C}{\partial V_f} = \frac{\partial}{\partial V_f}(E_m) - \frac{\partial}{\partial V_f}(V_f * E_m) + \frac{\partial}{\partial V_f}(V_f * E_f) = -E_m + E_f \qquad 3.2.16$$

Derivatives of the various models are listed in Table 3.2.13. A linear Equation has the form y=mx+b where m is the slope and b is the y-intercept. As seen in Figure 3.2.03 through

Figure 3.2.08,each model besides the IROM shows a linear relationship between the volume fraction and Young's modulus of the composite. In the case of the rule of mixtures model, the linear relationship can be expressed as

$$E_C = (E_f - E_m)V_f + E_m$$

when V_f=0, E_c equals E_m, therefore E_m is the y-intercept. The Equation can then be rearanged by subtracting the intercept from both sides, which is the translation of the coordinate axis

$$E_C - E_m = (E_f - E_m)V_f$$

Then divide both sides by the slope $(E_f\text{-}E_m)$

$$\frac{E_C - E_m}{E_f - E_m} = V_f$$

Which is equal to the normalization factor

$$\frac{E_C - E_m}{E_f - E_m} = E_N = V_f \qquad 3.2.18$$

These results seem to suggest that the normalization facor will be equal to the volume fraction for all specimens. However, Figure 3.2.09, which shows three distinct slopes for each of the three orientations, random, transverse and longitudinal. Therefore, V_f in Equation 3.2.18 would be multiplied by an orientation dependent factor, *M*, and Equation 3.2.18 can be more accurately expressed as

$$\frac{E_C - E_m}{E_f - E_m} = E_N = V_f * M \qquad 3.2.19$$

the orientation dependent factor, *M*, would be equal to the slope of each line Figure 3.2.09, see Table 3.2.11.

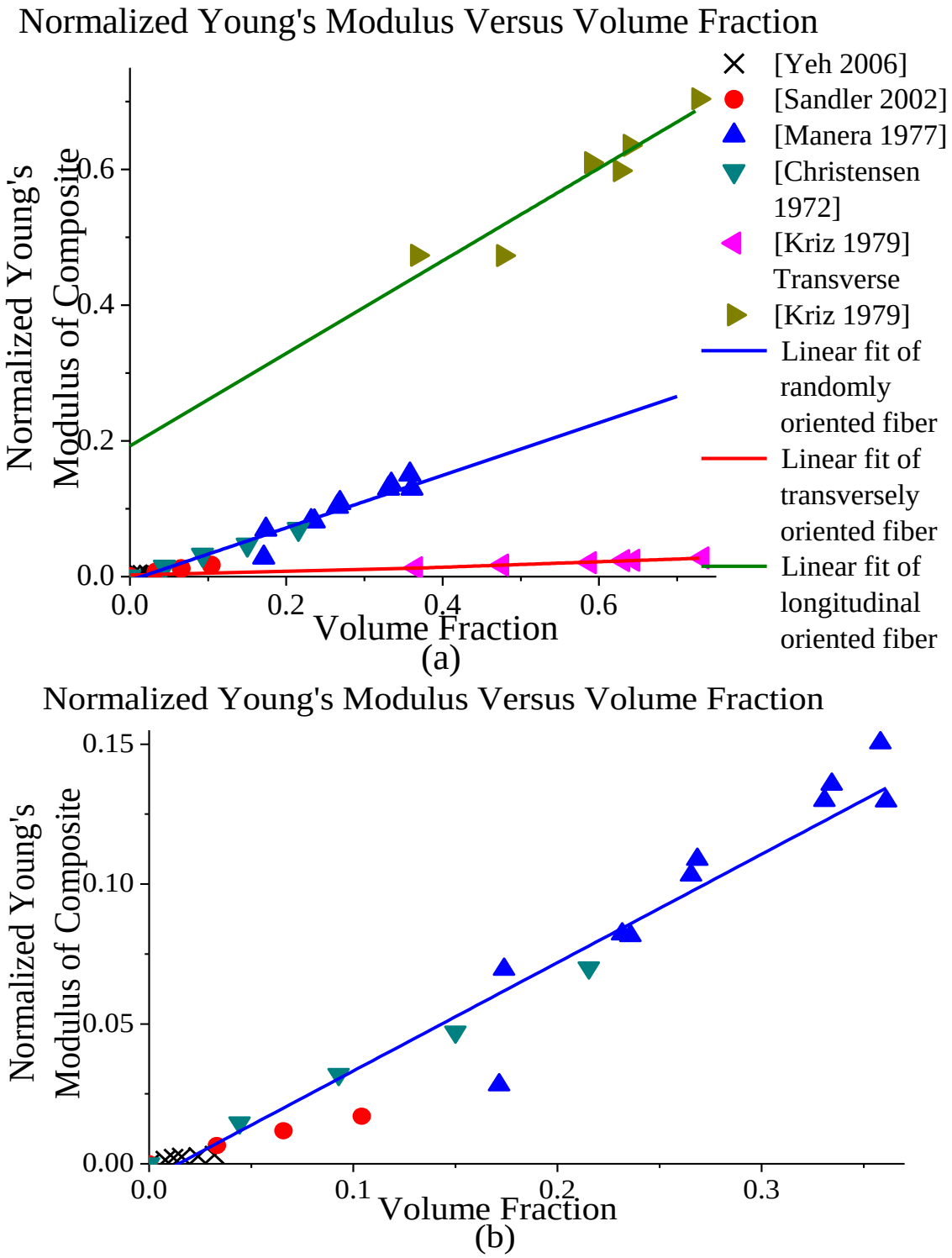

Figure 3.2.09 Normalized data sets from Figures 3.2.03 through 3.2.08. (a) Longitudinally oriented fibers data and their linear fit line are green, the transversely oriented data and linear fit line are red and the randomly oriented fiber data and the corresponding linear fit line are blue. (b) an expanded view of the plot in (a), the same legend applies to both

Table 3.2.11 Slope, intercept and coefficient of determination, R^2, of linear fit lines in Figure 3.2.09 (a) and (b)

Fiber Alignment	Slope	Intercept	R^2
Random Orientation	0.388	-0.006	0.980
Transverse	0.040	-0.002	0.985
Longitudinal	0.683	0.192	0.884

The roughly normalized data sets are plotted against their volume fraction of fiber in Figure 3.2.09. The data sets from Yeh, Sandler, Manera and Christensen [Yeh 2006; Sandler 2002; Manera 1977; Christensen 1972] all contain randomly oriented fiber and had V_f values below 0.40. A linear fit of the randomly oriented fiber data sets was plotted in blue and most points fall fairly close to this line, R^2=0.98. A linear fit was also plotted for the longitudinal and transverse data sets as well, which are green and red respectively. The linear fit for the longitudinally aligned fibers has a slope of 0.683. The slope for transverse oriented fibers is nearly flat, and the slope of randomly oriented fiber is between the two. This shows that the maximum Young's modulus enhancement will come from fibers oriented in the longitudinal direction.

The y-intercept, as shown in Table 3.2.11, is not equal to zero. For the randomly oriented fiber and transverly oriented fiber, it is quite close. For longitudinally oriented fiber, it is is noticably high. This may just be attributed to the fact that there are few data points available for the data set. If the lowest volume fraction data point in the Kriz longitudinal data set [Kriz 1979] was removed, the plot would have a slope closer to one and an intercept closer to zero, which may indicate that the data point is an outlier, see Figure 3.2.10.

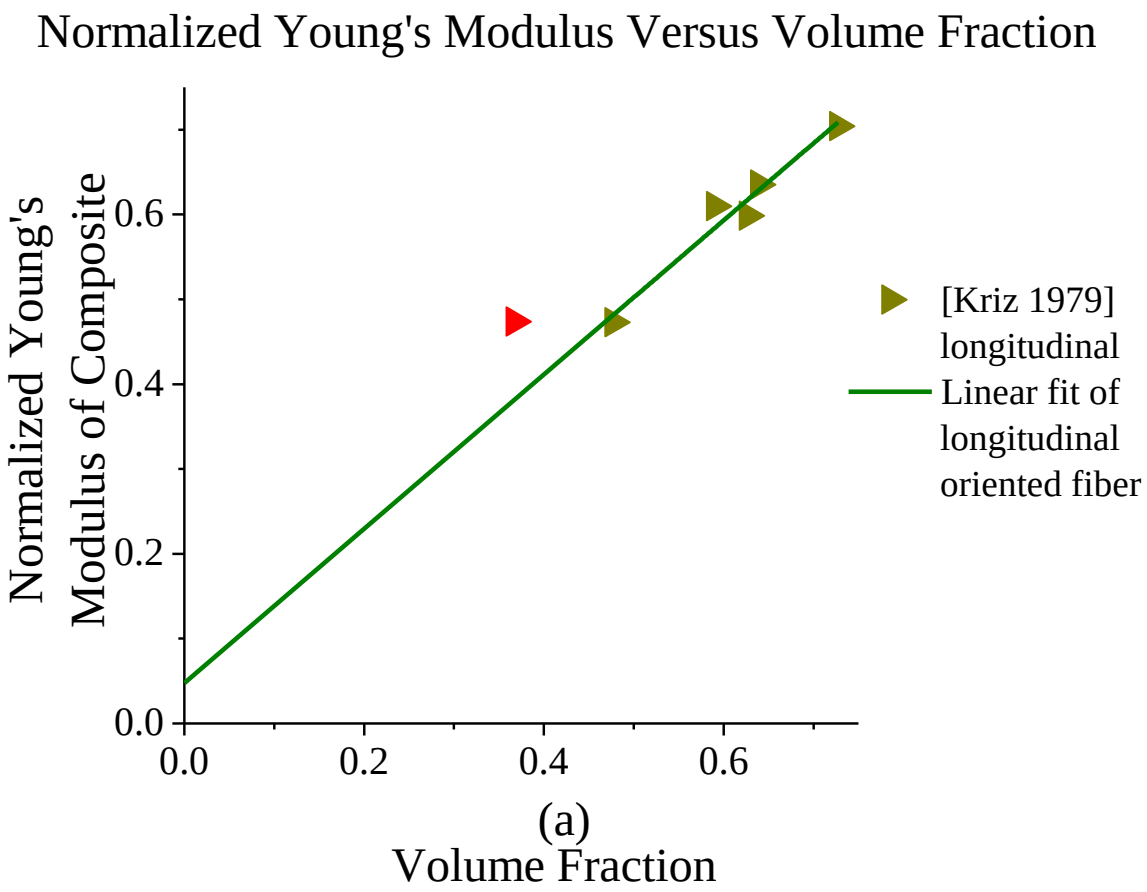

Figure 3.2.10 Elastic modulus versus volume fraction for Kriz [Kriz 1979] according to Equation 3.2.19 data set when the red data point is not included in the linear fit (green line).

Table 3.2.12 slope, intercept and linear coefficient of determination for Figure 3.2.10

Fiber Alignment	Slope	Intercept	R^2
Longitudinal	0.909	0.048	0.945

However, a data point cannot be ignored without good cause, so the linear fit shown in Figure 3.2.09 and Table 3.2.11 should be considered a more valid analysis of the data set in Kriz [Kriz 1979] than Figure 3.2.10 and Table 3.2.12. If there was much more data, a more exact slope and intercept could be determined for the longitudinally aligned fiber in Figure 3.2.09. However, it can still be observed that the longitudinally oriented fiber will have a greater slope than randomly oriented or transversely oriented fibers.

The normalization factor, Equation 3.2.15, used for Figure 3.2.09 and Table 3.2.11 is based on the rule of mixtures, but similar results could be obtained with the other models. The derivative, and therefore the slope, of each model is displayed in Table 3.2.13.

Table 3.2.13 the Equation for each model in Table 3.2.02 as well as the partial derivative with respect to volume fraction (V_f)

Name	Equation	Derivative
Rule of mixtures	$E_{CU} = V_m E_m + V_f E_f$	$\frac{\partial E_{CU}}{\partial V_f} = E_f - E_m$
Inverse Rule of mixtures	$\frac{1}{E_{CL}} = \frac{V_m}{E_m} + \frac{V_f}{E_f}$	$\frac{\partial (E_{CL})}{\partial V_f} = \frac{E_f * E_m (E_f - E_m)}{(E_f V_m - E_m V_f)^2}$
Christensen	$E_C = \frac{V_f}{6} E_f + (1 + (1 + \nu_m) V_f) E_m$	$\frac{\partial E_C}{\partial V_f} = \frac{E_f}{6} + E_m (1 + \nu_m)$
Manera	$E_C = V_f \left(\frac{16}{45} E_f + 2E_m\right) + \frac{8}{9} E_m$	$\frac{\partial E_C}{\partial V_f} = \frac{16}{45} E_f + 2E_m$
Curtis	$E_C = x * V_f E_f + V_m E_m$	$\frac{\partial E_C}{\partial V_f} = x E_f - E_m$
Pan	$E_C = E_f \frac{V_f}{2\pi} + E_m \left(1 - \frac{V_f}{2\pi}\right)$	$\frac{\partial E_C}{\partial V_f} = \frac{1}{2\pi} (E_f - E_m)$
Halpin-Tsai with constant shape factor	$E_C = \frac{1 + C\eta V_f}{1 - \eta V_f} E_m \quad \eta = \frac{\alpha \frac{E_f}{E_m} - 1}{\alpha \frac{E_f}{E_m} + C} \quad C = \frac{2\lambda}{d}$	$\frac{\partial E_C}{\partial V_f} = E_m \frac{\eta (1 + C)}{(1 - \eta V_f)^2}$

In a linear Equation using the Curtis or Pan model they would take a similar form as Equation 3.2.17, except with some constants attached to E_m and E_f, as shown in Equation 3.2.20

$$E_C = (A * E_f - B * E_m) V_f + E_m \qquad 3.2.20$$

where A and B are constants dependent on the coefficients of E_m and E_f from the derivative in Table 3.2.13.

For each of the two models, A and B will have different values causing *M*, the orientation dependent factor, to be slightly different, but they will still be similar. If E_f is much larger than E_m, the slope will be positive, that is to say, an increasing volume fraction will create a higher Young's modulus composite. If E_m is much larger than E_f, the slope will be negative or the composite will decrease in elastic modulus as volume fraction increase. The slope of the various models when either E_m or E_f is much larger than the other is displayed in Table 3.2.14.

Table 3.2.14 approximate slope of models from Table 3.2.02, found by taking the derivative of each Equation

Name	The slope of E_c with increasing V_f if $\mathbf{E_f >> E_m}$	The slope of E_c with increasing V_f if $\mathbf{E_m >> E_f}$
Rule of Mixtures	$\frac{\partial E_{CU}}{\partial V_f} \approx E_f$	$\frac{\partial E_{CU}}{\partial V_f} \approx -E_m$
Inverse Rule of Mixtures	$\frac{\partial (E_{CL})}{\partial V_f} \approx \frac{E_m}{{V_f}^2}$	$\frac{\partial (E_{CL})}{\partial V_f} \approx \frac{-E_f}{{V_f}^2}$
Christensen	$\frac{\partial E_C}{\partial V_f} \approx \frac{E_f}{6}$	$\frac{\partial E_C}{\partial V_f} \approx E_m(1+\nu_m)$
Manera	$\frac{\partial E_C}{\partial V_f} \approx \frac{16}{45}E_f$	$\frac{\partial E_C}{\partial V_f} \approx 2E_m$
Curtis	$\frac{\partial E_C}{\partial V_f} \approx xE_f$	$\frac{\partial E_C}{\partial V_f} \approx -E_m$
Pan	$\frac{\partial E_C}{\partial V_f} \approx \frac{E_f}{2\pi}$	$\frac{\partial E_C}{\partial V_f} \approx -\frac{E_m}{2\pi}$
Halpin-Tsai with constant shape factor	$\eta =$ positive the Equation for $\frac{\partial E_C}{\partial V_f}$ does not significantly reduce, but it will be positive	$\eta = n$egative, becomes very small as C increases $\frac{\partial E_C}{\partial V_f} \approx -E_m$

The Manera and Christensen models do not work very well when $E_m >> E_f$. In the derivatives of the Manera and Christensen models (Table 3.2.13) E_m and E_f of are summed together, meaning regardless of which is bigger, the slope will be positive and therefore Young's modulus will continue to increase as volume fraction increases. But the Young's modulus should decrease with increasing volume fraction if the fiber has a smaller Young's modulus than the matrix. Both of these models have restrictions for what volume fraction they

can apply to, and they seemingly have the restriction of only applying to systems that increase with fiber addition.

This leaves the inverse rule of mixtures (IROM) and the modified Halpin-Tsai model. Both of these Equations have V_f^2 in the denominator of their derivative (Table 3.2.13), making them the only two Equations that are not linear. In the IROM model, E_m and E_f are both in the denominator and the difference between the two is squared, so the greater the difference, the greater the bowing. The numerator of the IROM has $E_f - E_m$, so like the ROM, Curtis and Pan models, if E_f is much larger than E_m, the slope will be positive, and if E_m is much larger than E_f, the slope will be negative.

As for the modified Halpin-Tsai model, the complexity helps give it robustness. The derivative, according to Table 3.2.13 is positive unless one of its terms is negative. The only term that could be negative is η. If E_m is significantly larger than E_f, the denominator of η becomes negative, and therefore the slope is negative. The slope will be zero when $E_f/E_m = 1/\alpha$. If E_f is greater than E_m/α, η will be positive; and therefore the slope of E_c versus V_f will also be positive.

The reason for examining these models is to better understand the elastic moduli of LLZO and lithium at varying composition. Unlike the data sets previously discussed, if lithium dendrites act as fibers in LLZO, the matrix has a higher Young's modulus than the fiber being added. In fact, the E_m is higher than E_f by an order of magnitude [Ni 2012], see Figure 3.2.16. Table 3.2.15 shows what should happen when E_m is significantly higher in a fiber composite. The rule of mixture, the Curtis model and the modified Halpin-Tsai model all show the same relationship: the slope of the Young's modulus of the composite versus the volume fraction will be equal to $-E_m$. This is an interesting observation because the rule of mixtures is meant for the

case of longitudinally oriented fibers and the Curtis and modified Halpin-Tsai models are for randomly oriented fiber, but they yield the same slope. Therefore, in a composite where $E_m >> E_f$, as long as the fibers are either randomly oriented or oriented in the longitudinal direction, they will have a slope of $-E_m$. The pan model gives a slope of $-E_m/2\pi$, which is about 1/6 of the estimate made by the ROM, Curtis model and modified Halpin-Tsai model. The inverse rule of mixtures(IROM) predicts the slope will be much smaller but still negative. However, it is reasonable for the IROM to be much smaller because IROM is for the case of transversely aligned fibers, and is therefore used as a lower bounds for estimates of a composite material [Kingery 1976a]. Lastly, the Christensen and Manera models both predict a positive slope for E_c versus V_f even in the case of $E_m >> E_f$, see Table 3.2.14. The Christensen models are probably not applicable for the LLZO dendrite composite and this will be discussed more in section 3.2.2.3

3.2.2.3 Plot for Young's Modulus of LLZO Containing Dendrites

Figure 3.2.11 shows the discussed models applied to LLZO with lithium dendrites. The fiber/matrix composite is based on a sample from Ni et al. [Ni 2012] that had 3% porosity and Young's modulus of 149.8 GPa. The Young's modulus for lithium dendrites was assumed to be 10.35 GPa. This is the average of the Hashin and Shtrikman bounds at 25˚ C, which are 12.2 and 8.5 GPa, respectively [Trivisonno 1961]. The Poisson's ratio could also be found from the average of the Hashin and Shtrikman bounds found in Trivisonno and Smith [Trivisonno 1961].

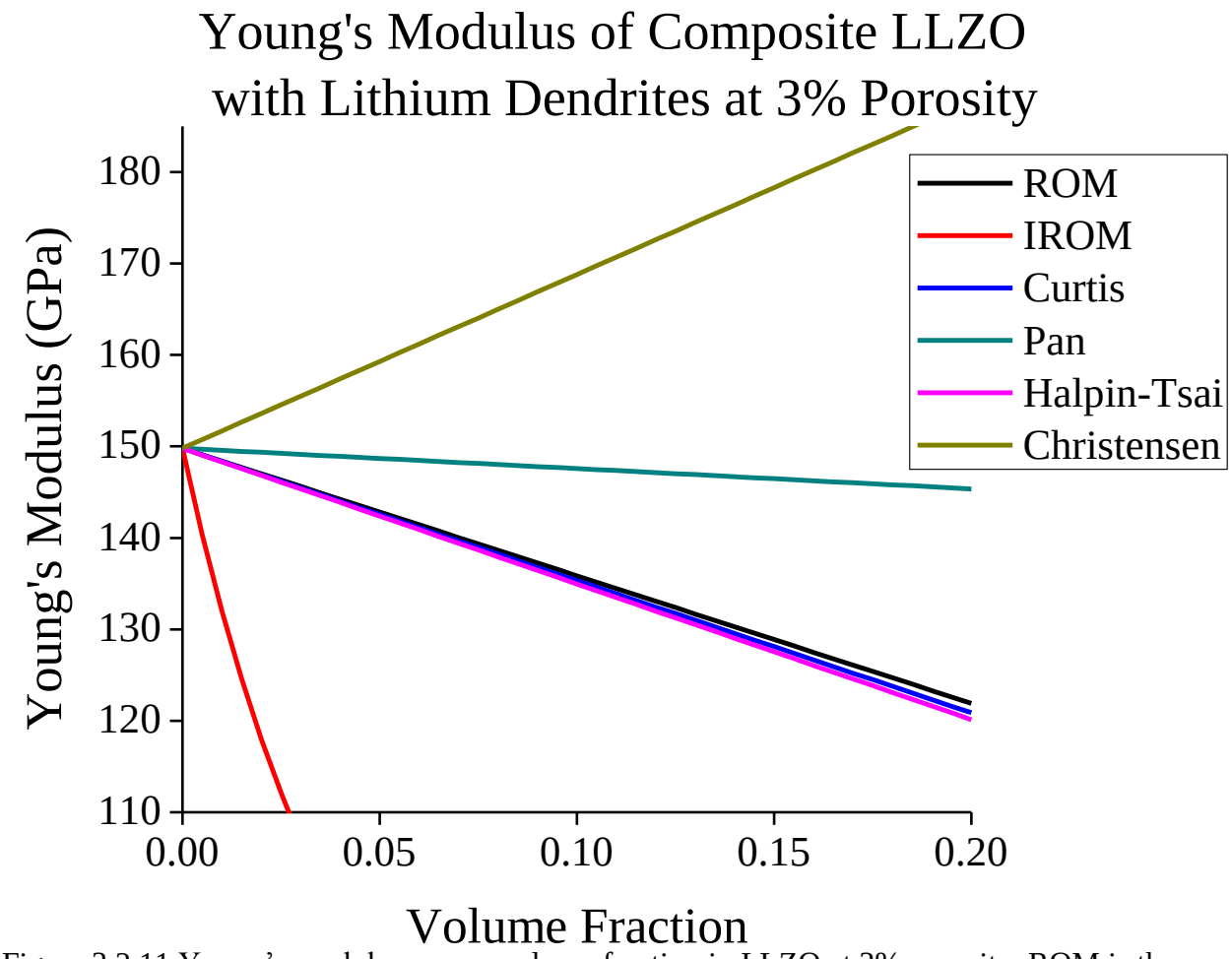

Figure 3.2.11 Young's modulus versus volume fraction in LLZO at 3% porosity. ROM is the rule of mixtures model and IROM is the inverse rule of mixtures model.

Table 3.2.15 data and assumptions used to plot Figure 3.2.11

Parameter	**Value/assumption used**
composite description	LLZO at 3% porosity with dendrites
Young's modulus of matrix (E_m) (GPa)	149.8 [Ni 2012]
Young's modulus of fiber (E_f) (GPa)	10.35 [Trivisonno 1961]
Matrix Possion's ratio (ν_m)	0.257 [Ni 2012]
Fiber alignment	Dendrites would align mostly in the direction between the electrodes, not exclusively [Rosso 2006; Dollé 2002]
Fiber aspect ratio	Assumed to be 500

Figure 3.2.11 shows the previously discussed models plotted for Lithium Lanthanum Zirconium Oxide (LLZO). For the terms in the models, the values could be found in the literature. At 25˚ C, LLZO has a Young's modulus of 10.35 GPa [Trivisonno 1961], this will

decrease as the temperature rises, and it is likely that the inside of a battery will increase in heat, but it serves as a start point. LLZO has been measured at various porosities [Ni 2012]. A fully dense LLZO specimen is desirable, but it is easier to make LLZO with some porosity so 3% porosity LLZO was chosen which has been measured to have a Young's modulus of 149.8 GPa and a Poisson's ratio of 0.257 [Ni 2012].

Some assumptions had to be made for the models in Figure 3.2.11. For the Modified Halpin-Tsai Equation, α was assumed to be 1/6 because it is likely the dendrites are shorter than the thickness of the electrolyte [Yeh 2006]. If the dendrites were longer than the thickness of the electrolyte, they would bridge the electrodes which would lead to catastrophic failure. The aspect ratio was assumed to be very large so the *C* term in the modified Halpin-Tsai Equation was assumed to be 500. This is a reasonable assumption because the dendrites are likely to be thin and grow in length faster than they grow in thickness[Rosso 2006; Dollé 2002], however the dendrites will start short so the aspect ratio will be somewhat dependent on how long the dendrites has been growing. The Curtis model presented some uncertainties. The orientation parameter *x* is equal to 1 when all the fibers are aligned in the direction parallel to the stress. For the case of LLZO, *x* is equal to 1 when all dendrites extend directly along the path the ions travel from the anode to the cathode. This is the ideal scenario, but in reality, lithium ions are more likely to travel a nonlinear path. Brissot et al. [Brissot 1999] observed dendrites growing through a polymer solid electrolyte by in-situ microscopy, and the images reveal a "zig-zag" path or a mostly linear path through the electrolyte. Therefore *x* was assumed to be 0.5. If $x = 1$ it will be the same value as the ROM.

The validity of the models in Figure 3.2.11 is yet to be proven, but should still be discussed. It is evident that the ROM and IROM models do not provide the bounds in Figure

3.2.11. The ROM model assumes all fibers are oriented longitudinally to the applied stress, the IROM model assumes the fibers are oriented transversely to the applied stress. The IROM model is the lower bound and experiences exponential decay which is hard to observe in Figure 3.2.11 because it drops so quickly. The Pan model is noticeably higher than the ROM model. This warrants a closer look at the Equation

$$E_C = E_f \frac{V_f}{2\pi} + E_m \left(1 - \frac{V_f}{2\pi}\right)$$

When V_f =0, $E_c = E_m$ and this boundary condition holds true. However, when $V_f = 1$, the modulus of the matrix should no longer contribute to the modulus of the composite, but in the Pan model it does. In fact, more than 80% of the matrix modulus value is still added to the fiber modulus at $V_f = 1$. In light of this, the Pan model seems better suited for a material where the added fiber has a higher modulus than the original matrix. Therefore, the ROM and IROM are likely to be the bounds for the data, or at least similar to Figure 3.2.07 and Figure 3.2.08, the ROM and IROM would be near the edge of the true bounds for the data.

The Christensen model makes an even more unreasonable model for the LLZO/dendrite system plotted in Figure 3.2.11. The Christensen model anticipates the composite Young's modulus, E_c, to increase as fiber is added. Increasing Young's modulus was the anticipated results in the data sets previously discussed, and indeed it was the reason the fiber was added in the first place [Yeh 2006; Sandler 2002; Manera 1977; Christensen 1972; Kriz 1979]. However, dendrites are not intentionally added, and the new inclusion has a lower Young's modulus than the existing matrix (see Table 3.2.15). This identifies the unintended assumption of the Christensen model: increasing V_f increases E_c.

$$E_C = \frac{V_f}{6} E_f \ + (1 + (1 + \nu_m) V_f) E_m \qquad 3.2.03$$

What further limits the Christensen model, Equation 3.2.03, is that it is only valid for V_f less than 0.20 [Christensen 1972]. This is a reasonable limitation, considering when V_f is equal to 1, E_c will include twice the value of E_m. Therefore, the Christensen model is unsuited for modeling the LLZO/dendrite composite.

In conclusion of these models, Figure 3.2.07 and Figure 3.2.08 show that the ROM and IROM provide good bounds for fiber containing composites, though in the most extreme situations the data points maybe outside of these bounds, they should still be fairly close. As seen in Figure 3.2.05, the Manera model is good when the required conditions are met, but this is limiting because the E_m and the V_f must both be within a certain range. The Christensen model is also useful when its conditions are met, which are less restrictive, but the model is also only suitable for composites whose fibers have a higher Young's modulus than the original matrix, which is not the case for LLZO. In the plots in section 3.2.2.2, the Pan model seemed to be a fairly useful to model randomly oriented fiber containing composites. However in Figure 3.2.11, it was shown that the model is clearly not intended for composites whose matrix has a higher Young's modulus than the fibers, which again is the case for LLZO and the Pan model is thus unsuitable. The Curtis model may or may not be close depending on the orientation factor *x*. Unfortunately it cannot be empirically determined from the material and ultimately comes down to being decided almost arbitrarily by the person using the Equation. Table 3.2.03 is based on studies by Hull et al. and Sandler [Hull 1981; Sandler 2002] and lists several *x* values based on specific aspect ratios and fiber orientations, but this is only helpful when the fiber/matrix composite has the one of the specific aspect ratios and fiber orientations. In the plots in section 3.2.2.2, it was more useful to use the Curtis model to calculate the orientation factor, *x*, from the experimental data which could give an idea of the overall orientation of the

fibers. Lastly is the modified Halpin-Tsai model, which is shown in Figure 3.2.03 through Figure 3.2.08 to be most applicable to randomly oriented fiber composites. Even so it still makes a reasonable model for the LLZO composite.

In conclusion, if lithium in LLZO forms dendrites, it can be modeled as a fiber/ matrix composite. Most models available for fiber/matrix composite have been used to model a system where adding fiber increases the elastic moduli of the composite. LLZO with lithium dendrites would be the opposite scenario, where dendrite addition decreases the elastic moduli of the composite. The modified Halpin-Tsai Equation was shown to be a good model for a fiber/matrix composite system, whether the fiber addition increases or decreases the composite's elastic moduli. And in either case, the ROM and IROM will provide upper and lower bounds for the composite, respectively. The ROM, Curtis model and modified Halpin-Tsai models all have approximately the same derivative with respect to the volume fraction of fibers. Therefore, for the case that $E_m >> E_f$ such as in the case of LLZO and lithium composite. This would mean that whether the fibers are aligned longitudinally or randomly oriented, they will follow a similar relationship for Young's modulus of the composite versus volume fraction of the fiber. Furthermore, when several data sets from the literature, that had different fiber and different matrix materials, were normalized (Figure 3.2.09) it could be seen that the normalized modulus depends on the fiber orientation. And therefore, the fiber orientation is major factor in the elastic moduli of the material.

3.2.3 Effects of Solid Solution on Elastic Modulus

As discussed in section 1.6.1, a solid solution is where two or more elements can mix completely over a certain composition range. This may be the case with lithium in LLZO. The

effects on the elastic moduli from the a solid solution of lithium in LLZO can be described by the Nordheim's rule

$$A = A_0 + (A_1 - A_0)X + kX(1 - X) \qquad 3.2.21$$

where X is the atomic fraction of the solute atom, A can be a a varity of properties, A_1 is the value of A when X=1, the pure solute, and A_0 is the value of A when X= 0, the pure solvent. When the bowing parameter k =0, the Nordheim's rule is the rule of mixtures. The parameter k is the bowing parameter, which is a measure of the departure from linearity and has the same units as variable A, A_0 and A_1 [Kasap 2007]. X can also be expressed in terms of weight fraction [Fan 2013a].

The Nordheim's relation is often simply refered to as a parabolic function when discussing elastic moduli or hardness [Darrow 1969; Schenk 1998b; Schenk 1998a; Shchennikov 2003; Ren 2007; Ravinder 2001; Fan 2013b]and refered to by name when discussing thermal conductivity [Terada 1997]or electrical resistivity [Mori 1996; Jen 1991]

For the elastic moduli in particular, a rough gauge of the dependence of elastic moduli on composition is the ratio of the maximum and minimum values of Young's modulus (E_{max}/E_{min}) or bulk modulus, B_{max}/B_{min} over a given range of composition [Ren 2007; Fan 2013a]. Furthermore, the composition dependence of a number of solid solution systems follows Equation 3.2.21 and can exhibit large changes in elastic moduli as a function of X. Experimental studies of solid solution systems show, for example, E_{max}/E_{min} = 2.3 for $Ni_{0.7}Zn_{0.3}Gd_xFe_{2-x}O_4$ (0.2 < x < 1) [Rao 2003], E_{max}/E_{min} = 2.4 and B_{max}/B_{min} = 1.9 for $Mn_{1-x}Cd_xFe_2O_4$ (0 < x < 1) [Ravinder 2001]. Also, B_{max}/B_{min} values range from 1.4 to 2.8 for theoretical bulk modulus studies of solid solution systems including $(Mg_{1-x}Be_x)_3N_2$ [Mokhtari 2004], BN_xP_{1-x} and BN_xAs_{1-x} [Hassan 2005],for 0 < x < 1 in each case. For a solid solution of

the naturally-occurring thermoelectric mineral tetrahedrite $Cu_{10}Zn_2As_4S_{13}$ and the synthetic compound $Cu_{12}Sb_4S_{13}$ Fan et al.[Fan 2013a] found E_{max}/E_{min} and B_{max}/B_{min} values of 1.9 and 1.7, respectively.

The Young's modulus of a solid solutions for $Cu_{10}Zn_2As_4S_{13}$ and $Cu_{12}Sb_4S_{13}$ is plotted in Figure 3.2.12 from data in Fan et al.[Fan 2013a]. It is important to note that the Nordheim's rule is an empirical relationship because the bowing parameter k is not determined by first principles. For example, Kasap [Kasap 2007] list various experimentally determined values for k for the resistivity of metal alloys.

Figure 3.2.12 plots both the rule of mixtures and Nordheim's rule for data from Fan et al. For the Nordheim's rule, k was found from a polynomial fit. Equation 3.2.21 can be rewritten more explicitly as a polynomial

$$A = A_0 + \big((A_1 - A_0) + k\big)X - kX^2 \qquad 3.2.21\ a$$

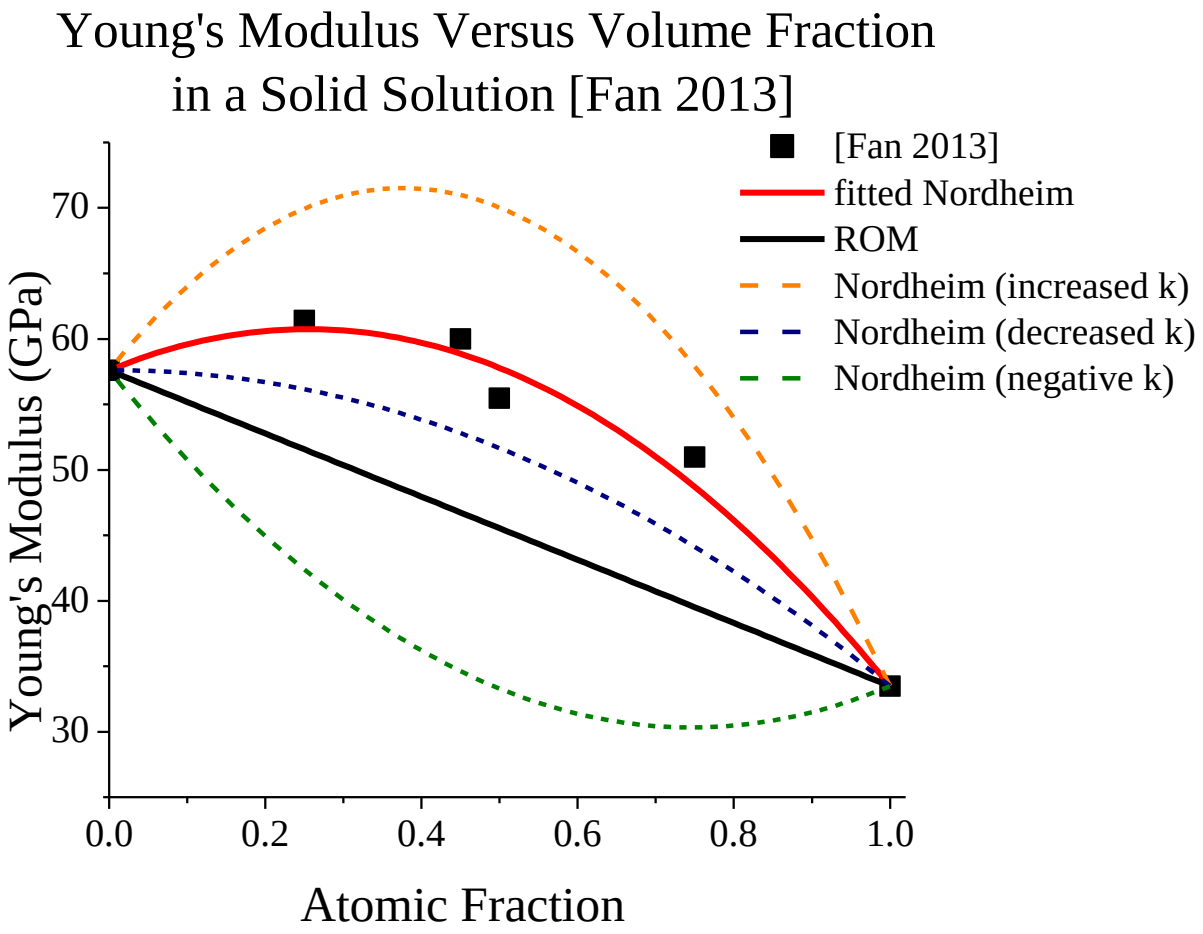

Figure 3.2.12 The modulus of $Cu_{10}Zn_2As_4S_{13}$ doped with $Cu_{12}Sb_4S_{13}$. Pure $Cu_{12}Sb_4S_{13}$ at weight fraction equal to 1 [Fan 2013a]. Together they form a solid solution, which follows closely to the Nordheim's rule. The solid red line represents least-squares fit of the Fan 2013a data to Nordheim's rule, whose constants are determined from a polynomial fit of the data. ROM is the rule of mixtures. The dashed lines represent the Nordheim's rule if only k changes.

Table 3.2.16 accompanying data for Figure 3.2.12 [Fan 2013a]

$E = E_0 + (E_1 - E_0 + k)X - kX^2$		
Material at x=0	$Cu_{9.7}Zn_{1.9}Fe_{0.4}As_4S_{13}$ natural [Fan 2013a]	
Material at x=1	$Cu_{12}Sb_4S_{13}$ synthetic [Fan 2013a]	
	Value	Error
E_0 (GPa)	57.597	1.847
E_1-E_0+k (GPa)	25.447	8.034
k (GPa)	48.977	7.580
R^2	0.964	

In Figure 3.2.12, the data is fitted to a polynomial in red, which takes the form

$a+bx+cx^2$ where a is equal to the E_0 of Equation 3.2.21, b is equal to E_1-E_0+k and c will be

equal to k, the bowing parameter. These values are listed in Table 3.2.16 with the accompanying error, as well as the materials that compose the solid solution. As mentioned previously, k must be determined experimentally and fitted from data. Once k was determined, Nordheim's rule was recalculated and replotted with various k values. The orange dashed line in Figure 3.2.12 labeled "Nordheim (increased k)" has a k value twice the calculated k value, that is to say k=97.954 GPa instead of 48.977 GPa. The blue dashed line in Figure 3.2.12 labeled "Nordheim (decreased k)" has a k value half the calculated k value, that is to say k=24.489 GPa instead of 48.977 GPa. The green line represents the k value multiplied by negative 1. The red line was the Nordheim relation that fit the data, but the other lines are added to elucidate how the bowing parameter can affect the modulus of a material. This bowing parameter is the most unique aspect of the Nordheim's relation. It demonstrates the fact that in a solid solution, the elastic moduli do not necessarily follow a linear relationship. Furthermore, in Figure 3.2.12 the Young's modulus of the doped material increased above the Young's modulus of both pure materials, a phenomenon that would not be expected by the composite models in section 3.2.2.

To further illustrate the changes in Young's modulus due to solid solution composition change, a second data set from Rao [Rao 2003] has been plotted in Figure 3.2.13. Table 3.2.17 has data for the fitted line as well as the materials that compose the solid solution material. Again, the k value for the orange dashed line is double the fitted k value, see Table 3.2.17, and the k blue dashed line has a k value half that of the fitted k value. The green line represents Nordheim's rule with –k.

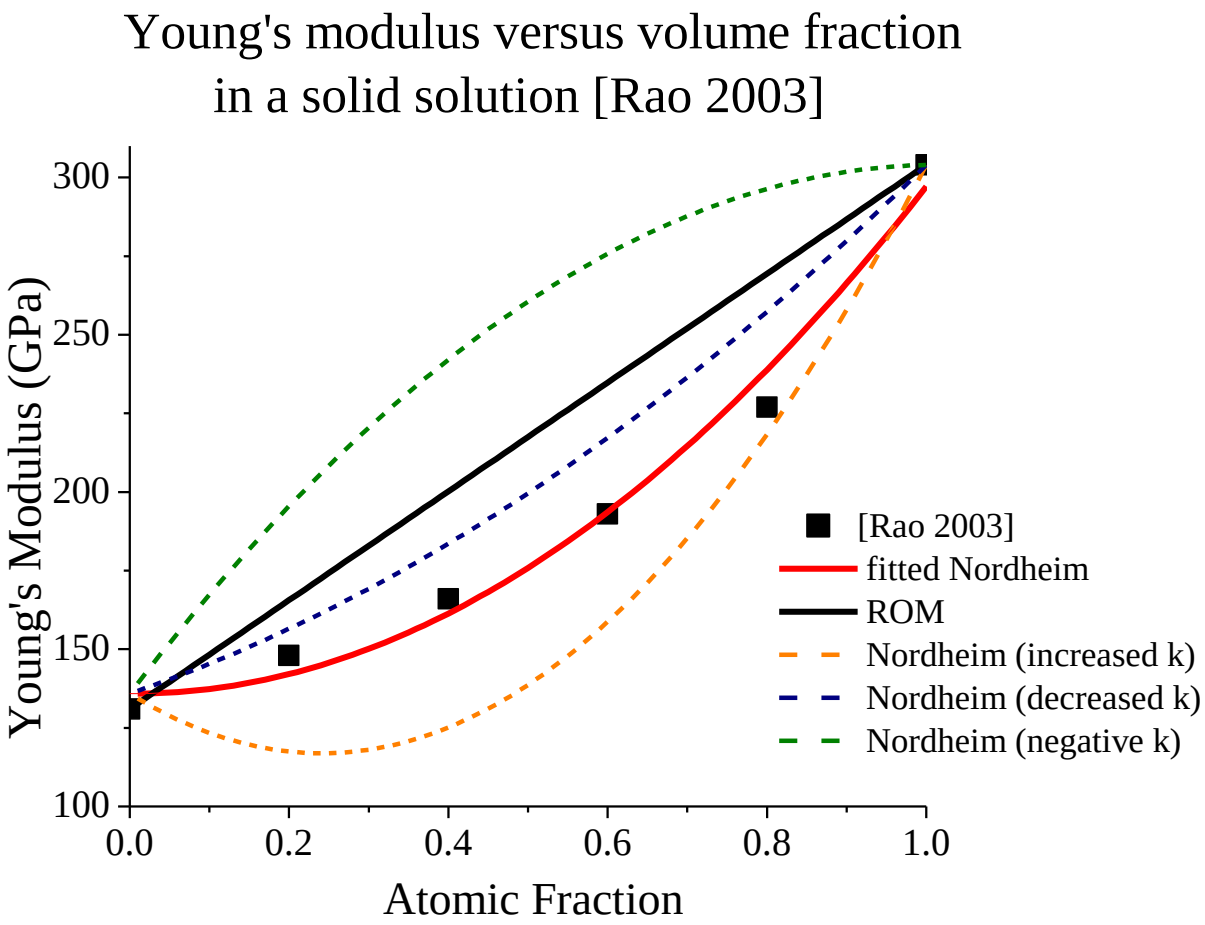

Figure 3.2.13 The modulus $MnFe_2O_4$ doped with various atomic fraction $CdFe_2O_4$[Rao 2003]. The solid red line represents a least-squares fit of the Rao 2003 data to Nordheim's rule whose constants are determined from a polynomial fit of the data. ROM is the rule of mixtures. The dashed lines represent the Nordheim's rule if only k changes.

Table 3.2.17 accompanying data for Figure 3.2.13 [Rao 2003]

$E = E_0 + (E_1 - E_0 + k)X - kX^2$		
Material at x=0	$MnFe_2O_4$ [Rao 2003]	
Material at x=1	$CdFe_2O_4$ [Rao 2003]	
	Value	Error
E_0	135.857	8.572
E_1-E_0+k	-1.214	40.314
k	-162.5	38.697
R^2	0.978	

In Figure 3.2.13, the modulus values obtained from Nordheim's rule are less than those obtained from the linear relationship. Therefore the solid solution may also result in lower Young's modulus than would be expected from the rule of mixtures or the other models used to for composites in section 3.2.2. The fitted polynomial results in Young's modulus between the two pure substances.

In both Figure 3.2.12 and 3.2.13, the dashed lines are based on Equation 3.2.21 a making them terminate at the first and last data point, but because the k value had to be calculated from the data, a polynomial fit had to be used. The E_0 and E_1 values calculated in the polynomial are slightly different than the E_0 and E_1 values that are plotted. For example, Rao[Rao 2003] provides E_0 as 131 GPa and E_1 as 304 GPa , but the values determined by the polynomial fit in Figure 3.2.13 were 135.857 GPa and 297.143 GPa. The error for each variable in the polynomial for Figure 3.2.13 (see Table 3.2.17) is much higher than the polynomial fit of the data in Figure 3.2.12 (see Table 3.2.16). The R^2 value for the polynomial fit in Figure 3.2.13 is of 0.978, so the polynomial is still a good fit.

No bowing parameter, k, is available from literature for LLZO with lithium, as no experiment has been done to determine elastic moduli of LLZO as a function of the concentration of any solute. Therefore, a curve cannot be made to generate the effects of lithium forming a solid solution with LLZO. However, it can be stated that as the LLZO specimens are doped (to enhance sinterability or electrochemical properties, for example) the modulus of the LLZO specimens can also change. For solid solutions, the moduli may even increase above the higher moduli material or decrease below the lower moduli material.

3.2.4 Microcracking

Microcracking can have a strong effect on the elastic moduli of a material. The extent to which microcracking affects the elastic moduli is a function of crack width, crack depth, crack length, force applied to generate a crack, temperature and the crack density [Case 1993; Kim 1993b; Fan 2012]. During this study, it was noticed that the elastic modulus for specimens of LLZO were decreasing after sanding (see Table 3.1.02 for values of Young's modulus, shear modulus and Poisson's ratio). Sanding may induce microcracking which can be detrimental to the elastic modulus of LLZO.

In the work by Case and Kim [Fan 2012; Case 1993]and by Fan et al. [Fan 2012], the microcrack damage layer was produced in either alumina [Fan 2012; Case 1993] or hydroxyapatite specimens Fan et al. [Fan 2012] via Vickers indentation. Thus, the number of cracks, crack length and crack depth could be measured and controlled. In contrast, if we apply these models to the microcrack damage layer produced by sanding, it is not straightforward to determine the number of cracks, crack length, crack depth and the applied load. The crack pattern from sanding is difficult to control, the loads on particular grit are not known, and the damage from sanding is much closer to that of a "sliding indentation" rather than a Vickers indentation. First, we shall discuss how the damage due to a sliding indentation differs from that of a Vickers indentation and then we shall discuss how the microcrack damage due the sliding indentation was estimated.

Vickers indentation is used to study brittle fracture and how cracks propagate in a material, and can be used to determine the hardness of the material[Bower 1994]. The Vickers hardness test use a pyramid shape "sharp" indenter that causes plastic deformation at the point of contact [Bower 1994]. Vickers indenters make a diamond shaped impression and the cracks

will propagate from the corners forming two median cracks [Swain 1979], see Figure 3.2.14 (c). The median cracks propagate from the plastically deformed region. Two types of cracks can occur from a Vickers indenter, half-penny (or semi-ellipse) or Palmqvist, see Figure 3.2.14 [Ponton 1989]. Systems that develop Palmqvist cracks at low loads may develop into half-penny cracks at increased loads, thus the half-penny system is considered a fully developed crack [Kim 1993a]. The depth of the half-penny crack, c, will be equal to half the distance of the surface diagonal crack.

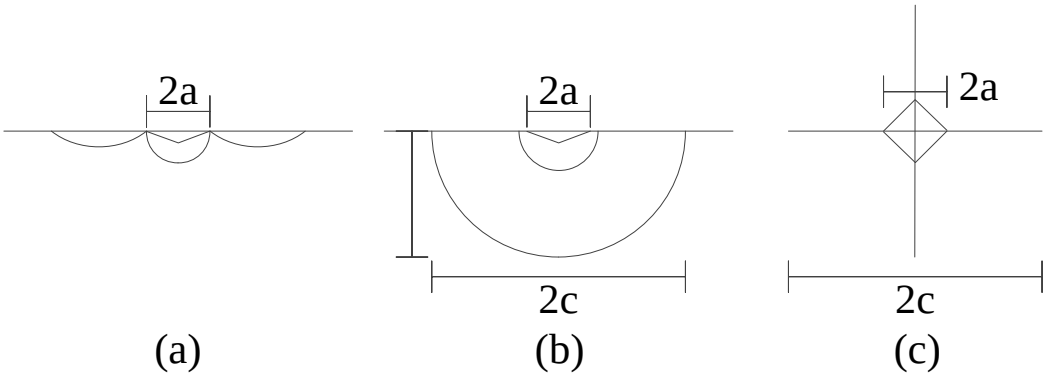

Figure 3.2.14 Palmqvist versus half-penny or modified half-ellipse radial-median crack system from Vickers indentation (a) side view of Palmqvist (b) side view of half penny crack (c) top view of indentation and cracks, which is the same whether the crack is Palmqvist or half-penny. The small circles below 2a in (a) and (b) are the plastically deformed regions. The larger circle in (b) represents the median crack and (c) shows that there are two median cracks perpendicular to one another in a typically Vickers indentation [Kim 1993a; Fan 2012]

Sliding indentation differs from Vickers indentation because of a tangential or shearing force is introduced perpendicular to the indentation force [Sharp 1993]. At the point of contact, sliding indentation is initially the same as in Vickers indentation, a plastic region of deformation is made, and diagonal cracks form either as Palmqvist or half-penny crack [Swain 1979]. As the indenter begins to slide and form a scratch on the materials surface, one of the cracks will continue to propagate in the direction of the sliding, whereas the other median crack will stay immobile at the initial site of contact [Swain 1979]. The curved edges of a half-penny crack will only be at the beginning and end of the crack, so over far enough an area, the crack

can be considered a slit crack (see Figure 1.6.01). The median crack below the scratch may move to the left and the right as the crack forms because the crack propagates mainly along the grain boundaries [Zarudi 1996]. Zarudi et al. found the area immediately connected to the scratch was plastically deformed and the median crack formed below the plastically deformed region of the scratch [Zarudi 1996]. Therefore there is a set of subsurface cracks generated by sliding indenters or by sanding/machining that extend into the specimen (from the plastically deformed surface) that are not visible by observing the specimen surface.

It is important to note Lateral cracks may also form in systems where loads are high enough that friction forces cause stick and slip to occur [Swain 1979]. These lateral cracks extend nearly parallel to the surface and can cause chipping or spalling near stationary cracks, or chipping in the case of surface abrasion. Also, Swain observed that at very low loads (<0.05 N) in a study using various glass samples and sapphire, no surface or subsurface cracks were detected and the track of the scratch was exclusively plastically deformed [Swain 1979]. This is believed to be the mechanism for sanding where scratches plastically deform the material and the plastically deformed region is removed without causing cracks [Swain 1979]. If the calculated loads are very low for the present study of LLZO, there is the possibility that microcracking does not form at all, but if this is the case, the calculated change due to microcracking would be very small as well. This is consistent with a crack "pop-in" threshold load that has been observed for Vickers indentation cracks.

3.2.4.1 Method and Model

To determine the change in Young's modulus for LLZO due to sanding, the specimen was first sanded using two different grades of sandpaper (600 and 1200), as these were used as the final polish for specimens during the study. Then the specimens were analyzed using

scanning electron microscopy (SEM). In order to avoid surface charging in the SEM, the specimens had to be coated with platinum, since the uncoated LLZO surface is non-conductive. The micrographs were used to view the scratches. As stated by Swain and Zarudi et al. [Swain 1979; Zarudi 1996], the microcracks form beneath the scratches. The number of scratches, length of the scratch and width of the scratch were directly observed from the micrographs. The number of scratches determines the number of cracks, and the length of the scratches would be the length of the cracks. The width of the scratch could help to estimate the applied load as described below.

For the subsurface cracks due to abrasion, the depth of the crack is difficult to estimate. Subsurface microcracks below the scratch do not have the same relationship with surface cracks that a typical Vickers indentation has, (see Figure 3.2.14) which allow the crack depth to be measure. However, an understanding of the material's fracture toughness and hardness can be used to estimate the load and crack depth based on the micrograph measurements of the crack width.

A model for the change in Young's modulus due to a surface damage layer has been given by Case and Kim and by Fan et al. [Fan 2012; Case 1993]

$$\frac{\Delta E}{E_0} = \frac{r^2 + 3}{(r+1)^2}\frac{r}{(\mathrm{r}+1)} * f * \varepsilon \qquad 3.2.22$$

where E_0 is the Young's modulus of the material with no microcracks, f is a function of the spatial orientation of the microcracks, ΔE is the change in Young's modulus due to microcracking, r is the depth of the microcrack layer divided by the depth of the microcrack free layer and ε is the crack damage parameter [Fan 2012].

For simplicity sake, R can be defined as

$$R = \frac{r^2 + 3}{(r+1)^2}\frac{r}{(\mathrm{r}+1)} \qquad 3.2.23$$

Which reduces Equation 3.2.22

$$\frac{\Delta E}{E_0} = \mathrm{R} * f * \varepsilon \qquad 3.2.22\ \mathrm{a}$$

f can be determined based on the type of crack that forms. For a slit crack

$$f = \pi^2(1 - \nu_0^2)/2 \qquad 3.2.24$$

where ν is the Poisson's ratio.

The crack damage parameter ε is defined by the Equation [Budiansky 1975; Hoenig 1979; Fan 2012]

$$\varepsilon = N_v * G = \frac{2N_v}{\pi}\frac{< A^2 >}{< P >} \qquad 3.2.25$$

where N_v is the crack number density, *G* is the microcrack geometry factor (not the shear modulus) and *A* and *P* are the area and perimeter of the microcrack respectively [Case 1993].

In order to use the technique used by Case et al. [Case 1993] to find the damage due to surface abrasion rather than Vickers indentation cracks, we need to estimate the applied load on the abrasive particle, the number of cracks, and the crack dimensions. Also, instead of a standard half-penny crack generated by Vickers indentation, we shall assume that the sanding-induced cracks are long slot cracks.

Equation 3.2.25 shows ε is a function of area and perimeter which will be a function of the crack depth; *r* is also a function of crack depth. The crack depth, *c*, can be determined from Equation 3.2.26 from Lawn and Cook [Lawn 2011; Schmidt 2014]

$$K_C = \frac{(E/H)^{0.5}F}{c^{\frac{3}{2}}} \qquad 3.2.26$$

which can be rearranged to solve for c

$$c = \left(0.016 * \left(\frac{E}{H}\right)^{0.5} \frac{F}{K_C}\right)^{\frac{2}{3}} \qquad 3.2.26\text{ a}$$

where K_c is the fracture toughness, E is the Young's modulus, F is the load on the microcrack and c is the crack depth [Schmidt 2014].

Assuming the width of the abrasion scratch is approximated by the indentation width 2a, the load, F, can be estimate using Equation 3.2.27 from Wachtman [Wachtman 2009]

$$H = \frac{1.8544F}{(2a)^2} \qquad 3.2.27$$

which can be rearranged to

$$F = \frac{H(2a)^2}{1.8544} \qquad 3.2.27\text{ a}$$

where H is the hardness, F is the load and 2a is the width of the scratch.

For the abrasion induced cracks, the mean crack area, A, and mean crack perimeter, P, are given by

3.2.28 $$A = c * \mathrm{L} \qquad \mathrm{P} = 2c + 2\mathrm{L} \qquad 3.2.29$$

assuming a rectangular crack of length L and depth c for the subsurface crack that is beneath the surface scratch and is induced by sanding.

After the specimens were processed, micrographs of the surfaces were analyzed using SEM. one specimen that was not sanded was analyzed under SEM, but it showed no clear signs of microcracking (Figure 3.2.15). The specimen was cut from the same larger sample, S-LLZO-92314-B, that the other specimens were cut from.

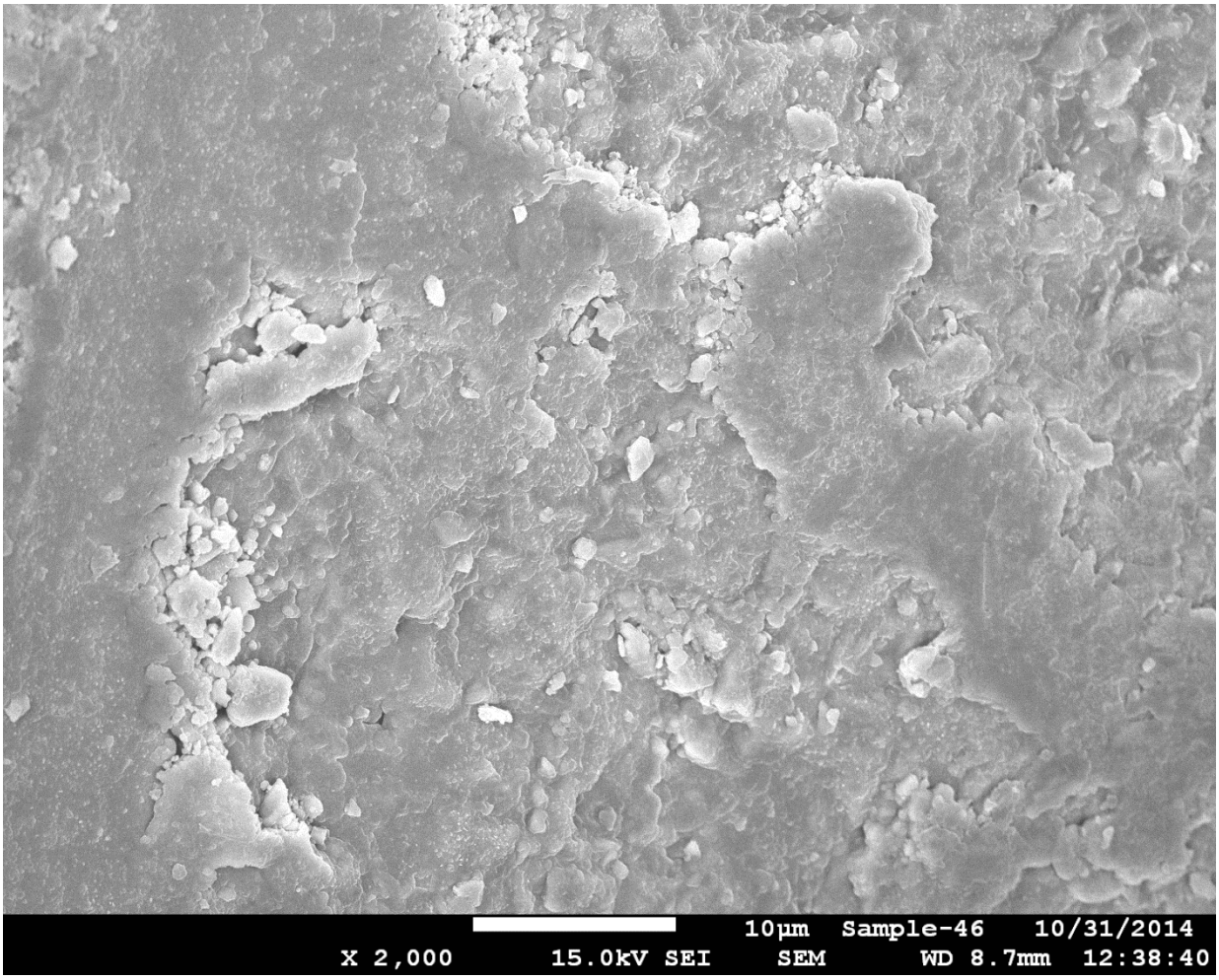

Figure 3.2.15 The cut surface of sample of S-LLZO-92314-B after being cut with the low speed diamond saw (viewed at 2000X magnification). No sanding was done to this specimen. The image shows no clear sign of cracking or scratches that may produce microcracking.

Figure 3.2.15 shows the cut surface of sample of S-LLZO-92314-B. No signs of scratches that would cause microcracking are visible.

Figure 3.2.16 and Figure 3.2.17 are micrographs of a different piece cut from S-LLZO-92314-B that were sanded using 1200 grit SiC sandpaper. Figure 3.2.16 shows magnification of 600X which was used to estimate crack number density, N_v, and crack length. Figure 3.2.17 shows the same area at a magnification of 1200X, which was used to estimate the width of the scratches.

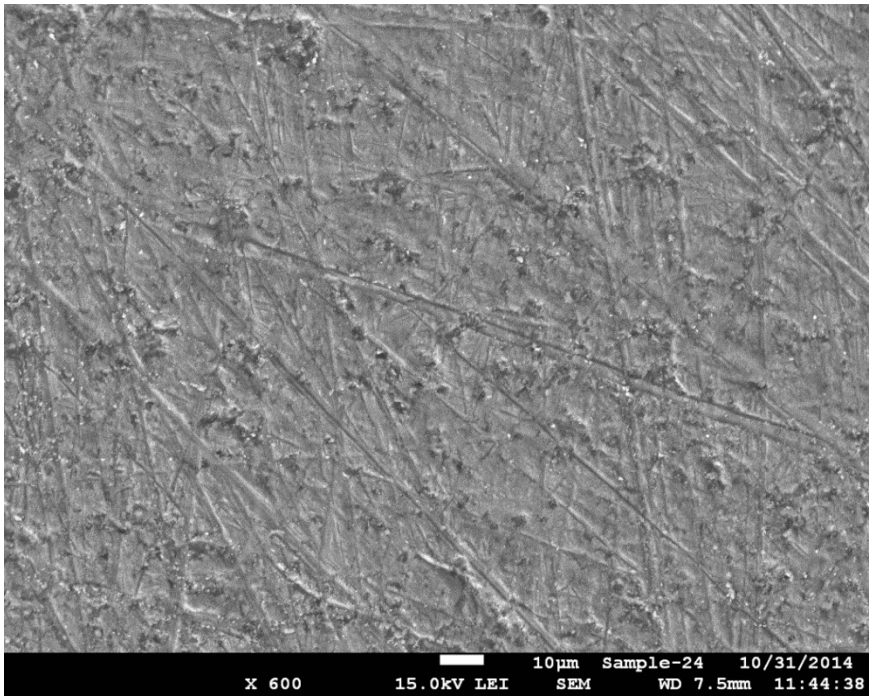

Figure 3.2.16 Sample of S-LLZO-92314-B after being sanded with 1200 grit SiC sandpaper at 600X magnification. The length and number of cracks were estimated from micrographs such as this.

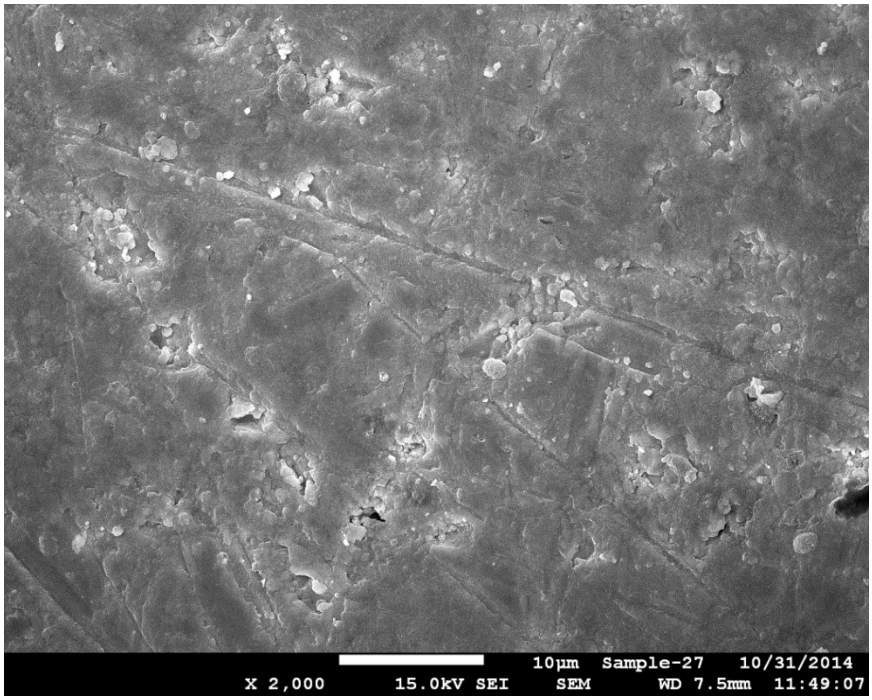

Figure 3.2.17 Sample of S-LLZO-92314-B after being sanded with 1200 grit SiC sandpaper at 2000X magnification. The width of the cracks could be estimated from micrographs such as this.

Figure 3.2.16 and Figure 3.2.17 show scratches from the sandpaper, which resembles sliding indentations. Microcracks form under the surface of the scratches, so the length of the microcrack can be assumed to be approximately the length of the scratch [Swain 1979]. From the micrographs of S-LLZO-92314-B, the average length of the scratch (and therefore of the cracks) was estimated as 263 μm and the width of the scratch was estimated to be 1.6 μm, see Table 3.2.18. Using this information, the impact of microcracking could be estimated for sample S-LLZO-92314-B.2. Values for S-LLZO-92314-B.2 post sanding were used because this specimen had the lowest RMS and was cut from S-LLZO-92314-B using the same low speed diamond saw procedure as was used to cut the LLZO pieces that were analyzed using the SEM. Furthermore, S-LLZO-92314-B.2 was sanded and thus could potentially have microcrack damage due to the sanding.

3.2.4.2 Tables and Figures for Microcracking

Table 3.2.18 lists the properties that had to be identified in order to estimate the change in Young's modulus due to microcracking for S-LLZO-92314-B.2. The thickness, Young's modulus and Poisson's ratio for S-LLZO-92314-B.2 are listed in Table 3.1.02. K_c and H are available in from Wolfenstine et al. [Wolfenstine 2013] and Ni et al. [Ni 2012], respectively. Measurements of H for specimens of the LLZO specimens with porosities of 3% and 6% were 6.3 GPa and 5.2 GPa respectively [Ni 2012]. S-LLZO-92314-B.2 post sanding had a porosity of 1.3%, and the Young's modulus was more than 30% less than 3% porous LLZO specimen in the study by Ni et al. [Ni 2012]. Nevertheless, the hardness values from Ni et al. [Ni 2012] were used to approximate H in this study. Also, the fracture toughness, K_c, determined by Wolfenstine et al. [Wolfenstine 2013] were used as an approximation here. Length and width of the crack as well as the number of cracks per volume were estimated by inspecting the SEM

micrographs. All of the other values (*f*, depth of crack, load per crack, average area of a crack, average perimeter per crack, crack damage parameter and *r*) were calculated.

Table 3.2.18 lists the estimated values for properties of specimens of S-LLZO-92314-B.2 post sanding after sanding with 600 grit sandpaper. The factor *f* is a function of the spatial orientation of the microcracks, *G* is the microcrack geometry factor, *r* is the depth of the microcrack layer divided by the depth of the microcrack free layer and ε is the crack damage parameter [Case 1993]

Property	**Description**	**value**	**units**	**Source**
T	Sample thickness	1320	μm	Table 3.1.02
E	Young's modulus	94.5	GPa	Table 3.1.02
ν	Poisson's ratio	0.352		Table 3.1.02
K_c (average)	Fracture toughness	1.25	MPa $*m^{1/2}$	[Wolfenstine 2013]
H	Hardness	6.3	GPa	[Ni 2012]
f (slit)		3.2		Equation 3.2.24
L	scratch length	263	μm	micrograph
2a	scratch width	1.6	μm	micrograph
a	Half of the scratch width	0.79	μm	micrograph
F	Load	8.5	mN	Equation 3.2.24
c	Depth	0.56	μm	Equation 3.2.26
A	Area	149	μm^2	Equation 3.2.28
P	Perimeter	528	μm	Equation 3.2.29
N_v (average)	Crack number density	468	$cracks/mm^3$	Micrographs
G		26.6	μm^3	Equation 1.6.14
r		0.00043		=c/(T-c)
ε		1.2×10^{-5}		Equation 3.2.25
$\Delta E/E_0$		5.1×10^{-8}		Equation 3.2.22

Table 3.2.18 includes an estimate of the $\Delta E/E_0$ in S-LLZO-92314-B.2 due to microcracks after sanding with 600 grit sandpaper. Specimen S-LLZO-92314-B.2 was sanded with 600 grit sandpaper and then sanded again with 1200 grit sandpaper. Table 3.2.19 includes the same properties and calculations that are displayed in Table 3.2.18 except with 1200 grit sandpaper being used instead of 600 grit. Calculations for Table 3.2.18 and Table 3.2.19 use the Young's modulus, specimen thickness and Poisson's ratio for S-LLZO-92314-B.2 post

sanding, thus the calculated difference in $\Delta E/E_0$ due to microcracking between Table 3.2.18 and Table 3.2.19 are due to the change in sandpaper grit.

Table 3.2.19 lists the estimated values for properties of specimens of S-LLZO-92314-B.2 post sanding after sanding with 1200 grit sandpaper. *f* is a function of the spatial orientation of the microcracks, *G* is the microcrack geometry factor, r is the depth of the microcrack layer divided by the depth of the microcrack-free layer and ε is the crack damage parameter

Property	**Description**	**value**	**units**	**Source**
T	Sample thickness	1320	μm	Table 3.1.02
E	Young's modulus	94.5	GPa	Table 3.1.02
ν	Poisson's ratio	0.352		Table 3.1.02
K_c (average)	Fracture toughness	1.25	MPa $*m^{1/2}$	[Wolfenstine 2013]
H	Hardness	6.3	GPa	[Ni 2012]
f (slit)		3.2		Equation 3.2.24
L	scratch length	174	μm	micrograph
2a	scratch width	0.72	μm	micrograph
a	Half of the scratch width	0.36	μm	micrograph
F	Load	1.74	mN	Equation 3.2.24
c	Depth	0.20	μm	Equation 3.2.26
A	Area	34	μm^2	Equation 3.2.28
P	Perimeter	349	μm	Equation 3.2.29
N_v (average)	Crack number density	540	$cracks/mm^3$	Micrographs
G		2.1	μm^3	Equation 1.6.14
r		0.00015		=c/(T-c)
ε		1.1×10^{-6}		Equation 3.2.25
$\Delta E/E_0$		1.6×10^{-9}		Equation 3.2.22

Table 3.2.18 and Table 3.2.19 include several different values for the selected crack damage model parameters. First, the scratch length and scratch width is larger in Table 3.2.18, also the scratch number is lower in Table 3.2.18. This is understandable as the 600 grit sandpaper that was used for Table 3.2.18 has a large particle size and fewer particles per unit area. Therefore the load at each sliding indentation would be higher in the 600 grit sandpaper than in the 1200 grit sandpaper because the same force is distributed over a smaller area (for the 600 grit), or fewer contact points, which accounts for the fewer microcracks. This would in

turn cause the scratches to penetrate deeper and wider, which accounts for the larger value for 2a in the Table 3.2.18 for sanding with 600 grit sandpaper.

Table 3.2.18 and Table 3.2.19 show $\Delta E/E_0$ is very small. Therefore the model used here predicts microcracking induced by sanding the specimen surface is not likely to have a significant effect on the Young's modulus of the S-LLZO-92314-B.2. Since many assumptions had to be made to determine the value of $\Delta E/E_0$ in Table 3.2.18 and Table 3.2.19, the value could be larger or smaller. Plotting Equation 3.2.22 can be quite useful to explore how changing the values of the parameters in Table 3.2.18 can affect the influence microcracking has on the Young's modulus. The crack damage parameter, ε is a function of N_v, and G. Figure 3.2.18 shows $\Delta E/E_0$ as a function of ε.

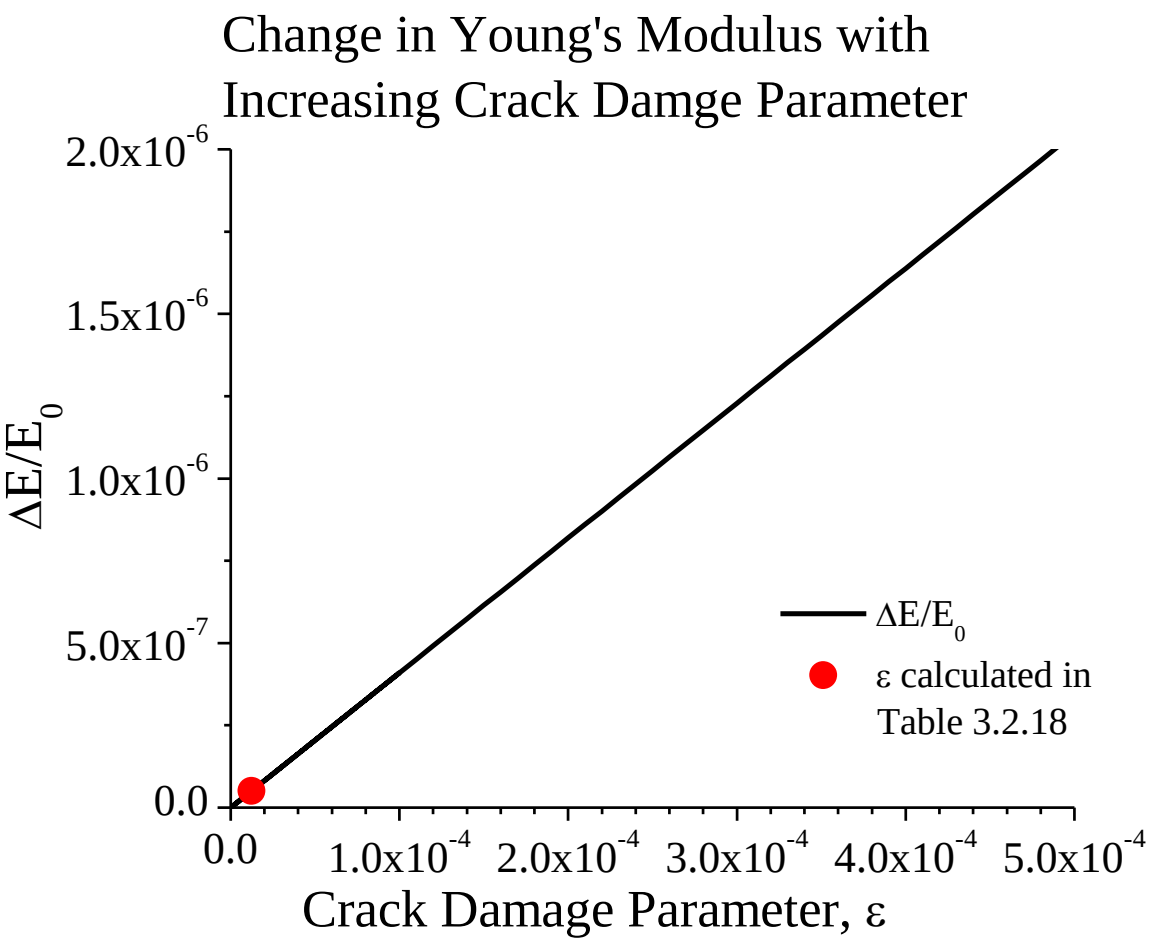

Figure 3.2.18 $\Delta E/E_0$ versus crack damage parameter using Equation 3.2.22 (black line) and using r and *f* values from Table 3.2.18.

Figure 3.2.18 shows the relationship between $\Delta E/E_0$ and the crack damage parameter, ε. For specimen S-LLZO-92314-B.2 post sanding using 600 grit sandpaper, ε is 1.1 X 10^{-5} which results in $\Delta E/E_0$ equal to 4.3 X 10^{-8}, as shown in Table 3.2.18. From Equation 3.2.22, the slope of the line is 3.87 X 10^{-3} which is a function of *r* and *f* as shown in Equation 3. 2-021

$$\frac{\Delta E}{E_0} = \frac{r^2+3}{(r+1)^2}\frac{r}{(r+1)} * f * \varepsilon = 3.87 * 10^{-3} * \varepsilon \qquad 3.2.30$$

where *f* is a function of the spatial orientation of the microcracks and r is the depth of the microcrack layer divided by the depth of the microcrack free layer.

It is important to compare the predictions from Figure 3.2.18, Table 3.2.18 and Table 3.2.19 with the E values of S-LLZO-92314 measured by RUS, because S-LLZO-92314 is a

specimen that was sanded and may have a reduced E due to microcracking. Table 3.2.20 shows the change in E before and after sanding as measured by RUS.

Table 3.2.20 Young's modulus before and after sanding for specimens of S-LLZO-92314 with the $\Delta E/E_0$, as measured by RUS

Specimen Label	Young's modulus (GPa)		$\Delta E/E_0$
	before sanding	after sanding	
S-LLZO-92314-A	92.2	90.7	1.6%
S-LLZO-92314-B	96.7	94.0	2.8%
S-LLZO-92314-C	99.1	97.4	1.7%
S-LLZO-92314-B.2	97.1	94.5	2.7%
S-LLZO-92314 average	96.3	94.2	2.2%

The average $\Delta E/E_0$ for specimens S-LLZO-92314 after sanding was 2.2%. According to Equation 3.2.30, in order for microcracking to be responsible for a 2.2% $\Delta E/E_0$, ε would have to be 5.69. This is larger than the calculated value in Table 3.2.18 by a factor of 5.1×10^5. Thus, if the difference between the "before" and "after" sanding Young's modulus values are due to microcracking in the specimen, then the measured change in E due to microcracking is much larger than the change predicted from Equation 3.2.22. If the change in Young's modulus in Table 3.2.20 is due to microcracking, ε (a function of N_v and G) would have to be larger than was calculated. So either N_v or G is larger than estimated, or the change in Young's modulus in Figure 3.2.20 is not due to microcracking. Increasing N_v shows the same relationship as ε, so the number of cracks would have to be several orders of magnitude larger than was calculated to explain $\Delta E/E_0$ in Figure 3.2.20. G is dependent on several parameters, as shown in Equation 3.2.26 and Equation 3.2.27. Plots based on crack length, crack depth, load, fracture toughness and hardness will be explored in order to understand the relationship between $\Delta E/E_0$ and each of these parameters.

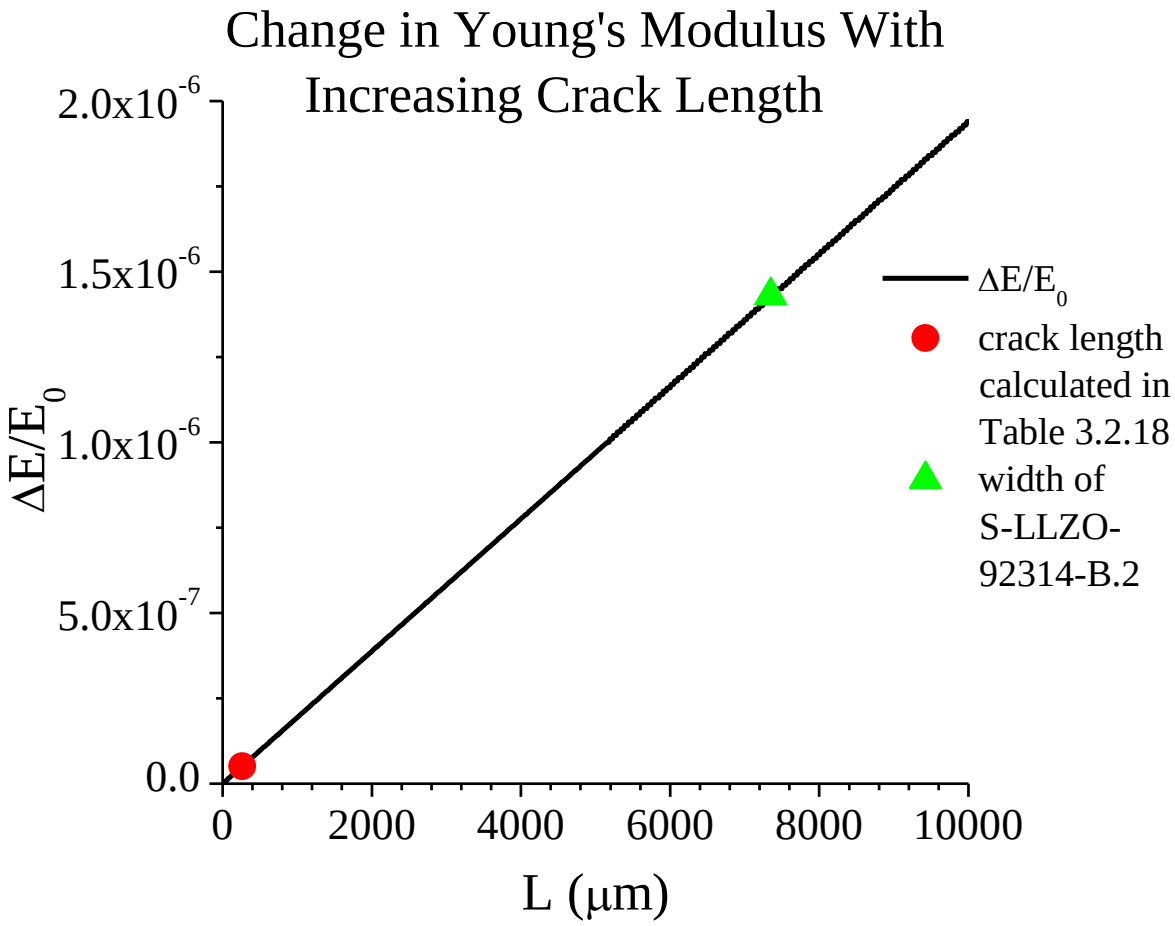

Figure 3.2.19 Change in Young's modulus versus the crack length, L, the red circle is the value of L calculated in Table 3.2.18. The green triangle is the crack length equal to the width of specimen S-LLZO-92314-B.2. The plotted line is obtained from Equation 3.2.22 c.

Figure 3.2.19 shows $\Delta E/E_0$ versus crack length. The relation between $\Delta E/E_0$ and L,

Equation 3.2.25 can be incorporated into Equation 3.2.22 to give

$$\frac{\Delta E}{E_0} = \mathrm{R} * f * N_v * G \qquad 3.2.22\ \text{b}$$

and incorporate Equation 3.2.28 and Equation 3.2.29 to obtain

$$\frac{\Delta E}{E_0} = \left(f * \frac{2N_v}{\pi}\right)\mathrm{R} * G = \left(f * \frac{2N_v}{\pi}\right)\mathrm{R} * \frac{< c^2L^2 >}{< 2c + 2L >} \qquad 3.2.22\ \text{c}$$

where R is a function of *r* (see Equation 3.2.23) which is in turn a function *c*

When *L* is much larger than c and all parameters besides *L* are held constant, $\Delta E/E_0$ will be proportionate to *L*. $\Delta E/E_0$ is still very small, on the order of 10^{-6}, even when the cracks run the entire width of a specimen (the width of specimen S-LLZO-92314-B.2 is used as an example in figure3.2.19. Therefore increasing the scratch length, and there by increasing the crack length, will not have a significant impact on $\Delta E/E_0$.

The crack depth is a critical property of microcracks. Figure 3.2.20 shows the relationship of $\Delta E/E_0$ and *c*.

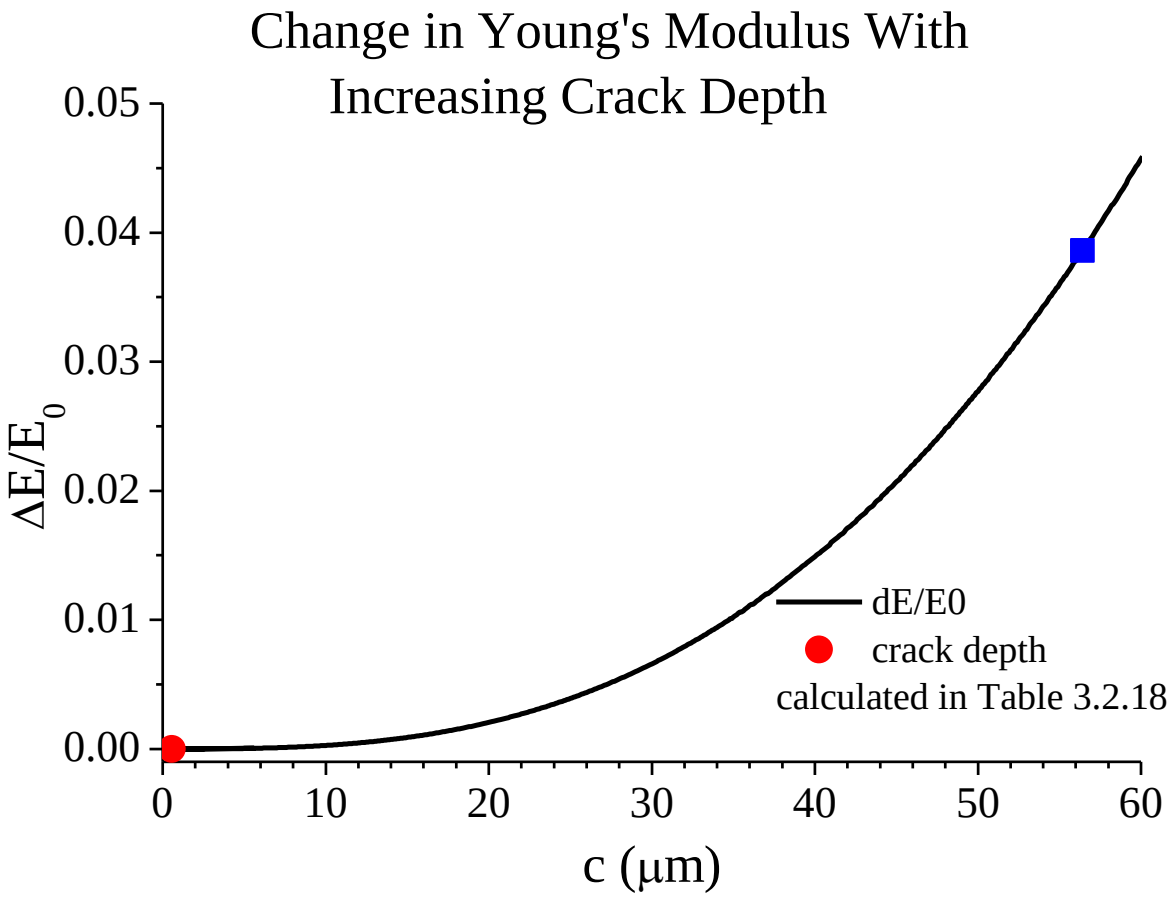

Figure 3.2.20 Change in Young's modulus as a function of crack depth according to Equation 3.2.22 c, black line. The red circle is the crack depth determined in Table 3.2.18 and the blue square represents a 100 fold increase in crack depth, which would correspond to a Young's modulus change that would be detectable by RUS analysis

Figure 3.2.20 shows the relationship between $\Delta E/E_0$ and the crack depth, *c*, using Equation 3.2.22 c. The red circle represents the calculated value of c as shown in Table 3.2.18, which is 5.1 X 10^{-8}. If *c* was actually two orders of magnitude larger than was estimated, then $\Delta E/E_0$= 3.86%. A Young's modulus change on the order of 4% would be detectable by the RUS analysis. To explain the power law relationship in Figure 3.2.20, Equation 3.2.22 c will be examined

$$\frac{\Delta E}{E_0} = \left(f * \frac{2N_v}{\pi}\right) \mathrm{R} * G = \left(f * \frac{2N_v}{\pi}\right) \mathrm{R} * \frac{< c^2 L^2 >}{< 2c + 2L >} \qquad 3.2.22\ \mathrm{c}$$

where R is a function of r (see Equation 3.2.23).

In Equation 3.2.22 c, we consider the crack depth to change and other factors such as *f* and N_v are held constant. R can be approximated as a linear function of c for the range shown in Figure 3.2.20. The crack length *L* is much larger than c, therefore <2*c*+2*L*> will be dominated by the *L* term, which is also a constant. Thus *G* will be proportional to c^2, making *G* a power law function of the second order. In turn, the product of *G* and R will be a power law function.

Figure 3.2.20 shows crack depth can have a noticeable impact on the Young's modulus, albeit the crack depth would have to be 100 fold higher than currently estimated in order to explain the decrease in E from sanding. A 100 fold increase in *c* correlated to a nearly a 10^6 fold increase in $\Delta E/E_0$. Thus it is important to consider which factors cause *c* to rise. Crack depth is a function of the applied load, hardness and fracture toughness, so their relationship to *c* and $\Delta E/E_0$ is plotted, using Equation 3.2.27, Equation 3.2.26 and finally Equation 3.2.22.

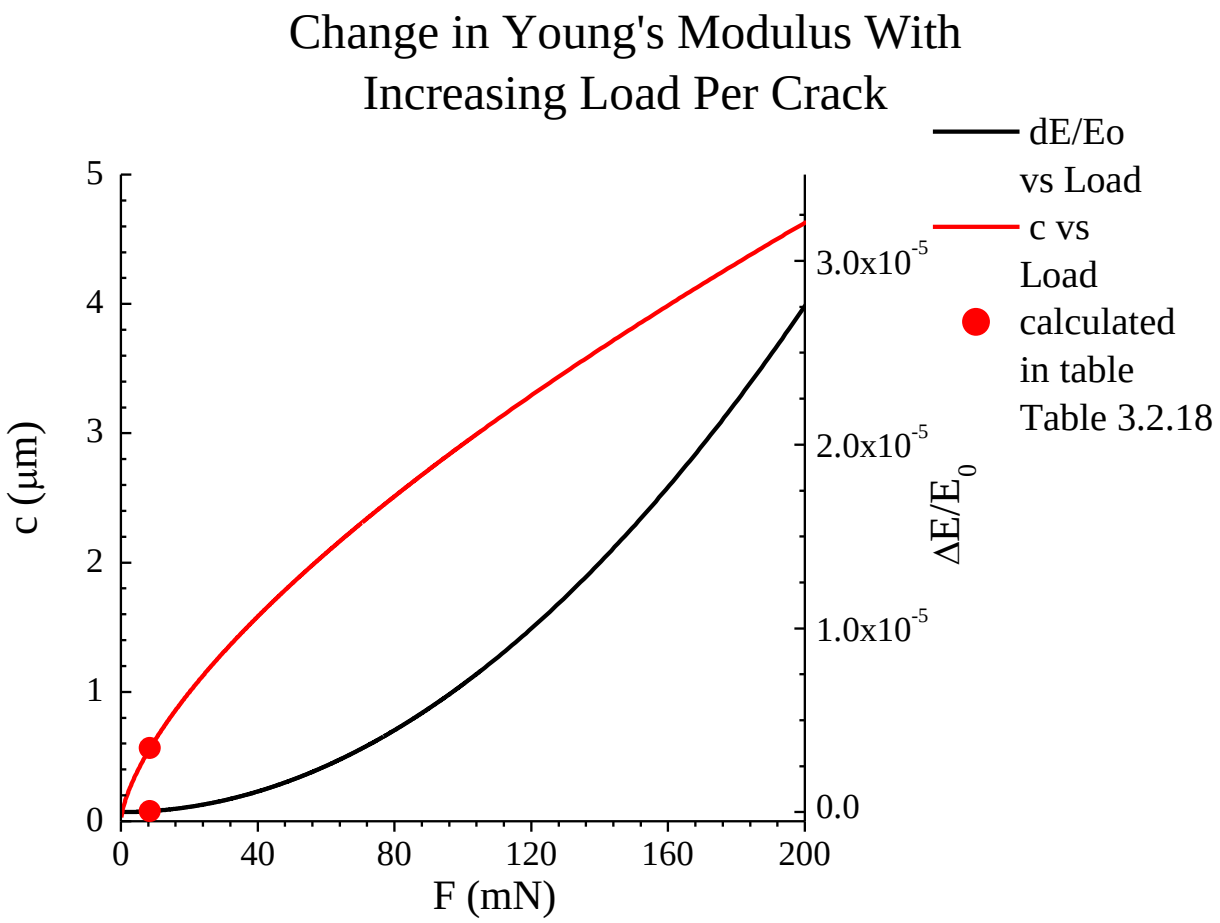

Figure 3.2.21 Change in Young's modulus (black line) and crack length, c, in microns (red line) as functions of Load, F, in mN. The red circles are the calculated values in Table 3.2.18 for each line and corresponds to the calculated load of 8.51 mN. The red line is a plot of crack length c as a function of F, from Equation 3.2.26.The black line is a plot of $\Delta E/E_0$ from Equation 3.2.22 in conjunction with 3.2.26

Figure 3.2.21 shows the F dependence of both $\Delta E/E_0$ (black line) and $\Delta E/E_0$ versus *c* (red line). The calculated value for the load is 8.51 mN, as shown in Table 3.2.18, which corresponds to $\Delta E/E_0=5.1 \text{ X } 10^{-8}$. Figure 3.2.21 shows *F*, like *c*, has a power law relationship with $\Delta E/E_0$, which is reasonable because c is a function of *F*. From Equation 3.2.26 it can be seen that *c* is proportionate to $F^{2/3}$.

$$c = \left(0.016 * \left(\frac{E}{H}\right)^{0.5} \frac{F}{K_C}\right)^{\frac{2}{3}} \qquad 3.2.26$$

Thus the red line for *c* versus load, in Figure 3.2.21 is equal to $F^{2/3}$ multiplied by some constant, which can be determined from Equation 3.2.26 as

$$c = 0.13531\, N^{-\frac{2}{3}} m * F^{\frac{2}{3}} \qquad 3.2.31$$

The calculated crack depth in Table 3.2.18 is 0.56 microns. Figure 3.2.20 shows *c* would have to increase by 1 or 2 orders of magnitude in order for $\Delta E/E_0$ to be measurable for the RUS analysis. Based on the relationship stated in Equation 3.2.31 the load would have to increase by well over two orders of magnitude. For example, the average change after sanding for specimens s-LLZO-92314 was 2.2%, as shown in Figure 3.2.20, to get this $\Delta E/E_0$ from sanding, c would have to be 46 microns, and in order to get this c value from changing the load alone, *F* would have to be 6.3 N. that is 6.3 N per scratch or contact point by the sand paper, which is significantly larger than the 8.5 mN load calculated in Table 3.2.18.

Values from literature were used to calculate the effects of microcracking on LLZO, see Table 3.2.18. However it has been seen in this study that LLZO can have drastically different elastic moduli values (see Table 3.1.02 for Young's modulus and shear modulus of various LLZO specimens from this study) compared to the Young's modulus values available in literature [Ni 2012]. Therefore, the LLZO specimens used in this study may have different K_c and H values than what is available in literature, K_c from Wolfenstine et al.[Wolfenstine 2013] and H from Ni et al.[Ni 2012]. Figure 3.2.22 plots $\Delta E/E_0$ versus K_c and Figure 3.2.23 plots $\Delta E/E_0$ versus H.

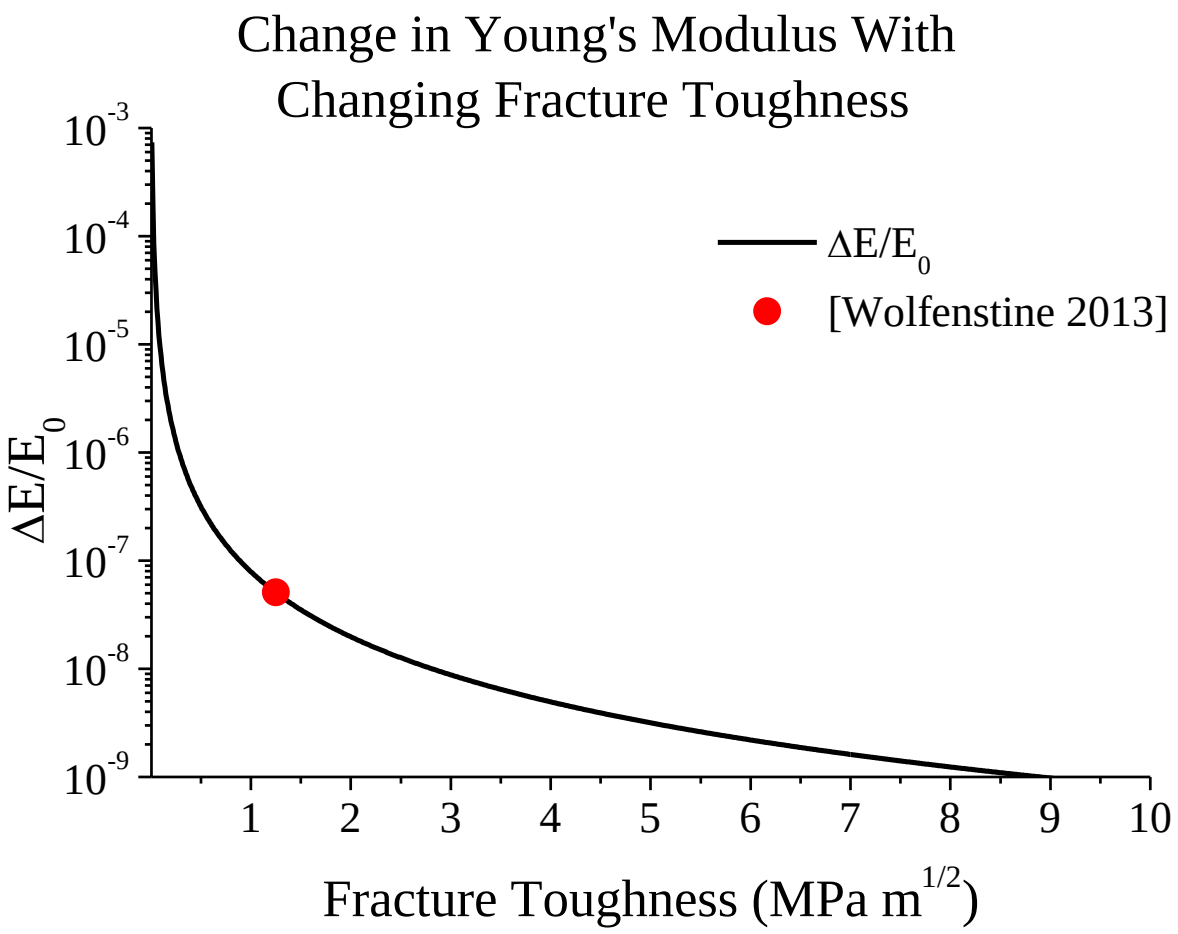

Figure 3.2.22 A semilog plot of the change in Young's modulus as a function of fracture toughness. The red circle represents the fracture toughness of 1.25 MPa *$m^{1/2}$ from Wolfenstine et al. [Wolfenstine 2013]. An increase in fracture toughness results in a sharp decrease in change in Young's modulus, since an increase in fracture toughness corresponds to a decrease in crack length for a given load. The black line represents Equation 3.2.22 c with varying *c* values, where *c* values are determined by Equation 3.2.26 with varying K_c values.

Figure 3.2.22 shows Young's modulus as a function of fracture toughness for S-LLZO-92314-B.2. Figure 3.2.22 follows Equation 3.2.22 c

$$\frac{\Delta E}{E_0} = \left(f * \frac{2N_v}{\pi}\right) \mathrm{R} * G = \left(f * \frac{2N_v}{\pi}\right) \mathrm{R} * \frac{< c^2 L^2 >}{< 2c + 2L >} \qquad 3.2.22\ \mathrm{c}$$

Where c is defined by Equation 3.2.26

$$c = \left(0.016 * \left(\frac{E}{H}\right)^{0.5} \frac{F}{K_C}\right)^{\frac{2}{3}} \qquad 3.2.26$$

The initial fracture toughness value was experimentally determined by Wolfenstine et al. [Wolfenstine 2013] based on measurements that ranged from 1.63 to 0.86 MPa $*m^{1/2}$, which would correspond to $\Delta E/E_0 = 1.1 \times 10^{-7}$ and $\Delta E/E_0 = 3.0 \times 10^{-8}$, when all other factors held constant. The red circle in Figure 3.2.22 is the average value, 1.25 MPa $*m^{1/2}$. As shown in Figure 3.2.22, as the fracture toughness increases the relative change in E decreases, again with other factors held constant. Of course, it is unlikely that the fracture toughness of LLZO could be significantly increased without perhaps and addition of fibers or particulate phases which might comprise LLZO's performance as an electrolyte. However, Figure 3.2.22 does illustrate as the higher the fracture toughness for any electrolyte material increases the resulting drop in Young's modulus due to sanding should decrease.

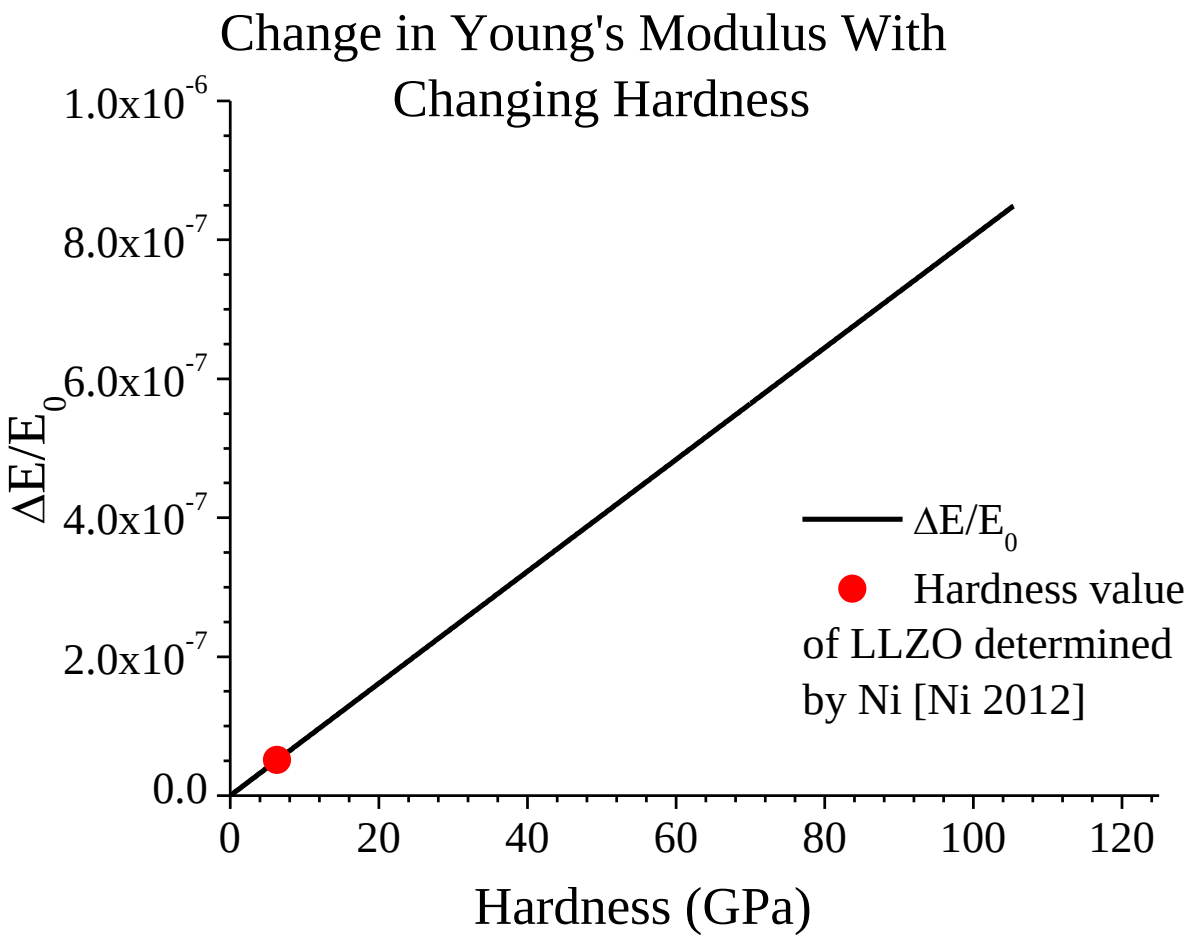

Figure 3.2.23 $\Delta E/E_0$ versus H. The red circle is the Hardness determined for LLZO by Ni et al. [Ni 2012]. The plot was determined by solving F according to Equation 3.2.27 a, then using *F* to solve for *c* according to Equation 3.2.26 and finally solving for 3.2.22 c

Figure 3.2.23 shows $\Delta E/E_0$ versus hardness, H. H values for LLZO were experimentally determined by Ni et al. [Ni 2012]. The value used in the calculations in Table 3.2.18 and for Figure 3.2.23 is 6.3 GPa (measured for an LLZO specimen with 3% porosity). The calculations done in Table 3.2.18 were for S-LLZO-92314-B.2 post sanding, which had a porosity of 1.3%. It was assumed the value from Ni would apply to S-LLZO-92314-B.2, so Figure 3.2.23 is particularly useful to determine the value of $\Delta E/E_0$ with different values of H. From Figure 3.2.23, even if the hardness was more than an order of magnitude larger, $\Delta E/E_0$ would still be quite small and this change in modulus would still not be measureable by RUS.

By incorporating Equation 3.2.27 into Equation 3.2.26, it is found that c is proportional to $H^{1/3}$. As previously stated, as long as L is much greater than *c*, *G* will be proportional to c^2. $\Delta E/E_0$ is proportional to *G*, and thus $\Delta E/E_0$ will be proportional to $H^{2/3}$. However, at low values, such as the H values in Figure 3.2.23, the Equation is effectively linear.

In conclusion, if sufficient microcracking present, noticeable change in elastic moduli of the material will occur. SEM micrographs were used to estimate the length and width as well as frequency of the surface scratches in order to estimate the dimensions of subsurface microcracks. Values for hardness and fracture toughness are available in literature [Ni 2012; Wolfenstine 2013]. Calculations for microcracking for specimen S-LLZO-92314-B.2 are shown in Table 3.2.18 and Table 3.2.19 for 600 and 1200 grit sandpaper respectively. From the model discussion here, the change in Young's modulus due to microcracking ($\Delta E/E_0$) was estimated to be 5.1 X 10^{-8} for the specimen that was sanded with 600 grit sandpaper and 1.6 X 10^{-9} for specimens sanded with 1200 grit sandpaper. These values would indicate microcracking has an extremely low impact on elastic moduli. However it was observed that sanding damage has a lesser effect on $\Delta E/E_0$ for sandpaper with a high grit number. Swain [Swain 1979] found that below 50mN of force per crack, no microcracking was observed in the various glass materials used in his study. It is uncertain if such a crack initiation threshold exists in LLZO, but using higher grit number sand paper as opposed to lower grit number sand paper can help to reduce the accumulation of microcrack damage.

With the information that was available, several assumptions had to be made in order to make rough estimates of the change in Young's modulus as a function of sanding-induced microcracks. The plots in Figure 3.2.19 through Figure 3.2.23 show microcracking as a function of crack length, L; crack depth, *c*; load per crack, *F*; Hardness, H; and fracture

toughness K_c. These figures explore how each of these parameters affects the $\Delta E/E_0$. Although the crack depth can have a strong influence on the $\Delta E/E_0$, $\Delta E/E_0$ is so low that the crack depth would have to increase significantly (more than an order of magnitude) before $\Delta E/E_0$ would be measureable by RUS.

4.0 Summary and Conclusions

The original intent of this study was to understand how the electrochemical cycling of Lithium Lanthanum Zirconium Oxide (LLZO) affects the Young's modulus, shear modulus and Poisson's ratio of the material. Any change in elastic moduli would likely be due lithium deposition, possibly as dendrites. The only published study of elastic moduli of LLZO was done by Ni et al. [Ni 2012]. Ni et al. used specimens of LLZO that were hot pressed at 1000˚C under a pressure of 40 MPa [Ni 2012]. The LLZO billets were then cut into rectangular parallelepipeds and analyzed using resonant ultrasound spectroscopy (RUS). Ni et al. found high elastic modulus values for LLZO using RUS; the Young's modulus, E, and shear modulus, G, of LLZO were 149.8 GPa and 59.6GPa at 3% porosity [Ni 2012]. Ni et al. also found LLZO had E= 132.6 GPa and G= 52.1 GPa at 6% porosity [Ni 2012]. The results from Ni et al. [Ni 2012] and the results from this study are listed in Table 3.1.02 which list the Young's modulus, shear modulus, Poisson's ratio, porosity and the RMS and peak count from the resonant ultrasound spectroscopy (RUS) analysis.

Table 3.1.02 shows that the measured elastic moduli in this study were noticeably lower than the results from Ni et al.[Ni 2012]. Each sample in this study was analyzed using RUS. Only specimens S-LLZO-62014 had results comparable to the LLZO specimens from Ni et al.[Ni 2012], see Figure 3.1.01 and figure 3.1.02. Sample S-LLZO-62014 was the second sample received in this study, so the procedure was not entirely established. Though the specimens had elastic moduli values that were comparable to published work, [Ni 2012], they were exposed to air for more than a few hours (they were stored in air overnight for multiple nights) and they were placed in acetone in order to wash off the thermoplastic, so the specimens were not electrochemically cycled. There were concerns that the prolonged exposure

to the acetone and the moisture in the air may have caused a reaction. The experimental procedure was changed so the specimens were stored in a glove box and the specimen was exposed less to acetone (see section 2.2.1.1 for more on the washing procedure).

Unfortunately, the billets received after S-LLZO-62014, would have noticeably lower elastic modulus compared to Ni et al. [Ni 2012]. Table 3.1.02 shows specimens S-LLZO-71014 had E values between 114 and 119 GPa, S-LLZO-72914 had E values from 96.3 to 101 GPa and S-LLZO-92314 had E vales from 90 to 100 GPa. The shear modulus was also noticeable lower than the samples from Ni et al. [Ni 2012]. From that point, much of the thesis work was focused on exploring possible causes for the discrepancies in moduli.

4.1 The Effect of Porosity on the Elastic Moduli of LLZO

Porosity is known to have an effect on the elastic moduli of LLZO. Figure 3.1.01 shows the Young's modulus versus the porosity of LLZO specimens from Ni et al. [Ni 2012] and the specimens S-LLZO-62014 (Section 3.2.1)

$$E(P)=167.16*\exp(-3.816*P) \quad 3.2.01$$

$$G(P)=67.40*\exp(-4.236*P) \quad 3.2.02$$

where E is Young's modulus, G is shear modulus P is the porosity.

The R^2 value for the exponential fit of the lines were 0.995 for E and 0.997 for G, see Table 3.1.01. Although there were only four data points to fit, Equations 3.2.01 and 3.2.02 fit extremely well. Unfortunately the rest of the specimens did not follow this pattern. Figure 3.2.02 shows all specimens from all billets received during this study and shows virtually no pattern between elastic moduli and porosity for the specimens as a whole group. However, Figure 3.1.04 shows a pattern of decreasing elastic modulus with increasing porosity for specimen S-LLZO-92314. The same pattern, of increasing porosity and decreasing elastic

moduli , is seen in Figure 3.1.01 for specimens S-LLZO-62014 and LLZO specimens from Ni et al. [Ni 2012]. Figure 3.1.01 and Figure 3.1.04 show that within a set of samples cut from the same billet, increasing porosity will cause decreasing modulus.

4.2 Fiber/Matrix Composite as a Model for the Change in Elastic Moduli of LLZO

Section 3.2.2 discusses how the elastic moduli could be affected by lithium deposition forming a fiber composite in the matrix of LLZO. Several models are explored, including the rule of mixtures(ROM), inverse rule of mixtures (IROM),modified Halpin-Tsai, Pan, Curtis, Manera and Christensen (Table 3.2.02 lists the Equations used to model the lithium LLZO composite system, as well as their source and conditions or assumptions inherent to the model). The models used in this discussion, have mainly, if not exclusively, applied to systems where the E and G values of the fiber were much higher than the E and G values of the matrix, and the fiber would serve to reinforce the matrix.

Several data sets [Yeh 2006; Sandler 2002; Manera 1977; Christensen 1972] with random fiber orientation were used to compare the model. These data sets are plotted in Figure 3.2.03 through Figure 3.2.06. The maximum fiber contribution to modulus of the composite is achieved when the fibers are oriented in the direction of the applied force [Kingery 1976a], like in Figure 3.2.08, so the experimental data follows most closely to the ROM model. On the other hand, the lowest fiber contribution of the fiber to the modulus is when the fibers are aligned perpendicular to the application of stress, like in Figure 3.2.07 and thus, the experimentally data follows closely to the IROM. The analysis of the models in section 3.2.2 helps to determine the utility of each model.

Each data sets had different materials which had different Young's modulus values for each fiber/matrix system. Each data set was normalized using Equation 3.2.15. The normalized

data was plotted in Figure 3.2.09 which plots the normalized Young's modulus versus the volume fraction of fiber for all the data sets, using Equation 3.2.19

$$\frac{E_C - E_m}{E_f - E_m} = E_N = V_f * M$$

where E_N is the normalized Young's modulus of the composite, which is unitless. E_C is the Young's modulus of the composite, E_f is the Young's modulus of the fiber and E_m is the Young's modulus of the matrix. M is a fiber-orientation dependent factor.

Figure 3.2.09 shows the data sets from Figure 3.2.03 through Figure 3.2.08 plotted according to Equation 3.2.19, would separate into 3 groups with different slopes, *M*, based on the orientation of the fiber. The slope, intercept and R^2 values are listed in Table 3.2.11. This is rather significant because it shows the data sets' major difference is the orientation of the fibers, but otherwise the data sets can be normalized (using Equation 3.2.19) to fit a line according to its orientation regardless of the fiber or matrix material. Therefore the normalization might be used as a guide to analyzing the orientation of the fibers in a particular data set, which would be applicable to a wide range of composite materials.

Figure 3.2.11 shows several of the models in Table 3.2.02 plotting E_c versus V_f for a matrix of LLZO with lithium dendrites as the fiber. Values had to be assumed for the E of LLZO, E of the lithium dendrites, Poisson's ratio of the matrix, the alignment of the fiber/dendrites and the aspect ratio of the dendrites. The Young's modulus value used for lithium metal was 10.65 GPa [Trivisonno 1961]. For LLZO, the Young's modulus was 149.8 GPa and the Poisson's ratio was 0.257 [Ni 2012]. The ROM and IROM typically serve as upper and lower bounds for a composite system when plotting the Young's modulus versus the volume fraction of the fiber; however the Pan and Christensen models were above these boundaries. The modified Halpin-Tsai and the Curtis model follow closely to ROM model and

can be considered good models to predict the relationship between E_c and V_f for a fiber/matrix composite consisting of dendrites in LLZO.

The Pan model gives a slightly decreasing slope for E versus V_f. When $V_f = 0$ E_c is equal to E_m which is true in Figure 3.2.11. However, as V_f approaches 1, the modulus of the matrix should contribute very little to the modulus of the composite, but in the Pan model more than 80% of the matrix modulus value is still added to the composite modulus at $V_f = 1$. Therefore, the Pan model seems better suited for a material where the added fiber reinforces the material and increases the E of the composite.

The Christensen model makes an even less reasonable model for the LLZO/dendrite composite shown in Figure 3.2.11 since it predicts an increase in Young's modulus of the composite as the volume fraction of fibers increases, which is only valid if the Young's modulus of the fiber is greater than that of the matrix, but this is not the case for the LLZO/dendrite composite, see section 3.2.2.3. Furthermore, the Christensen model is only applicable when the shear modulus of the fiber is greater than the shear modulus of the matrix, and this is not the case for the LLZO/dendrite composite, see Table 3.2.02.

The modified Halpin-Tsai makes a reasonable model for the LLZO/dendrite composite in Figure 3.2.11. The Curtis model does as well, but the orientation factor, *x*, is not determined by first principles and has to be determined by modeling the data. Since the Pan model and the Christensen model cannot be considered appropriate models for Li fibers in LLZO, the ROM and IROM once again serve as the upper and lower bounds of the models for the LLZO/dendrite system.

The Manera model was not used because the model assumes that the Young's modulus for the matrix, in this case LLZO, has to be between 2 and 4 GPa. LLZO was over 90 GPa in

all samples during this study (see table 3.1.02). Thus the LLZO matrix was much above the threshold of the Manera model.

A composite system of dendrite fibers in an LLZO matrix is a reasonable result of lithium deposition in a LLZO electrolyte. If the change in volume fraction of lithium in LLZO can be determined, then the changing modulus of LLZO upon cycling can be used to test the models included in this thesis.

4.3 Solid Solution as a Model for the Change in Elastic Moduli of LLZO

Lithium deposition within the LLZO could also act as a solid solution as discussed in section 3.2.3. A solid solution follows the Nordheim rule as shown in Equation 3.2.21 a

$$A = A_0 + (A_1 - A_0 + k)X - kX^2 \qquad 3.2.21\ a$$

where X is the atomic fraction of the solute atom, A can be a a varity of properties, A_1 is the value of A when X=1 ,the pure solute, *k* is the bowing parameter, A_0 is the value of A when X= 0, the pure solvent.

Nordheim's rule is effective for analyzing a solid solution, unfortunately no bowing parameter, *k,* is available for LLZO with lithium so Nordheim's rule cannot be used to predict the magnitude of changes in the Young's modulus. However, if LLZO specimens can be shown to form a solid solution with lithium after electrochemical cycling, the bowing parameter of lithium in LLZO could be determined for the first time. More importantly the model of Li deposition in LLZO could be determined.

4.4 The effect of Microcracking on the Elastic Moduli of LLZO

Microcracking can be detrimental to the elastic moduli of a material. There are multiples ways for microcracking to occur but of particular interest to this study is

microcracking due to sanding, which is a very common part of processing specimens. Specimens S-LLZO-92314 were analyzed using RUS, then sanded and analyzed again using RUS. The results for the before and after sanding RUS analysis are listed in Table 3.1.07. To analyze the effects of microcracking, a model modified from the model in Kim and Case [Kim 1993a; Case 1993; Kim 1993b] was used. This model considers the sanded layer as a microcrack damaged layer, and the rest of the material as a crack free layer. Kim and Case [Kim 1993b] induced a microcrack layer using Vickers indentation in alumina. Below the plastically deformed zone of the scratches microcracks will form [Zarudi 1996]. These cracks, unlike Vickers indentation cracks cannot be seen on the surface [Swain 1979; Zarudi 1996].

Sanding with 1200 grit number sandpaper caused a 1.6×10^{-9} relative change in Young's modulus, $\Delta E/E_0$, and sanding with 600 grit number sand paper produced a 5.1×10^{-8} relative change Young's modulus. Several estimates had to be made in order to make these calculations. First, measuring the length and width of the scratches is a tedious task that is subject to error as is counting the number of scratches. Also, the values in literature were assumed to be accurate for the particular specimens, but the Young's modulus, E, for the specimens in this study does not match the published values for E, so K_c and H may have different values for the specimens in this study versus the values available in literature. Due to the assumptions that were made, section 3.2.4.2 discusses some of the variables in the calculations for $\Delta E/E_0$ due to microcracking, including load, crack length, crack depth, hardness and fracture toughness. The depth of the crack has a strong impact on the change in Young's modulus due to sanding. However, it would still take more than an order of magnitude increase in the crack depth to cause the change in Young's modulus that was seen between sanding stages, see Figure 3.2.20. Therefore either (1) microcracking due to sanding is not the cause of

the change in modulus between sanding stage or (2) the model used to analyze the changes in modulus due to sanding is inadequate.

5.0 Future Work

Much work can still be done in this study. Table 3.1.07 shows there is a noticeable drop in Young's modulus and shear modulus after the specimen is sanded. Logically it would seem the specimen experiences some degradation due to the processing and the most likely explanation would be microcracking induced by the sanding. Section 3.2.4 discusses microcracking and shows that the model considered, which is applicable to a surface damage layers induced by Vickers indentation cracks, does not explain the changes observed in the LLZO after sanding. Thus, either the model, as applied to the sanding damage, is inadequate to describe the damage or another mechanism other than microcracking is responsible for the observed changes in modulus after sanding the LLZO specimens. Other than microcracking, there may be a reaction with the air that causes a drop in elastic modulus. The specimen is only exposed for a few hours at the most, and the time between initial RUS scanning and a second RUS scanning was even shorter. This would mean the reaction with air for LLZO is quite rapid, or at least fast enough to have noticeable effects within an hour or few hours of exposure to open air. Therefore, in the future more study of microcracking can be done to more thoroughly determine whether or not microcracking is the mechanisms causing a drop in elastic moduli.

According to the model presented in Section 3.2.4, it is highly unlikely microcracks are causing a measureable change in Young's modulus of the LLZO samples after sanding. However many assumptions had to be made to make these calculations. A key issue is that it is very difficult to determine the crack depth and crack length of the subsurface cracks induced by sanding the specimen surface. Also, only one specimen for each sandpaper grit was analyzed using SEM. More specimens could be inspected to get a better estimate of the scratch lengths, scratch widths and scratch number density, which are all used in the calculation for $\Delta E/E_0$.

Also, a direct determination of the subsurface crack depths and crack lengths would be very helpful.

This study serves as a good basis, or even a guide to continue the work. Simple mistakes during the study include washing the specimens with acetone directly and storing the specimens in air. These practices are completely acceptable for other materials, but are inappropriate for LLZO, and were corrected for specimens after S-LLZO-62014. Other incremental changes in the procedure included using a lapper to sand the specimens to a desired height (which limited the amount of material wasted) and cutting parallelepipeds using the aluminum block fixture discussed in section 2.2.1.2, which helped to ensure perpendicular cuts in the specimen.

RUS is a very useful tool to nondestructively determine the elastic moduli of a material. Defects such as chipping, cracks and impurities can reduce the elastic moduli of the specimens and make them difficult to analyze. Also, it was suspected that the LLZO specimens in this work may have had other phases present. What these phases were was beyond the scope of this study, but it might explain some of the difficulty with the RUS analysis. RUS alone cannot determine if other phases are present, but the analysis could be affected if there are.

Several models for the case of LLZO and lithium forming a fiber/matrix composite have been considered. The modified Halpin-Tsai model would be effective for modeling the composite. Also a model for a solid solution has been discussed. As data becomes available, these models could be useful to help understand how the lithium is being deposited.

Most importantly, the intended experiment should still be done. The intended work was to take specimens of LLZO, analyze the specimens using resonant ultrasound spectroscopy (RUS) to determine the elastic moduli of the specimens, cycle the specimens in a glove box

free of moisture, and then analyze them again with RUS to find the elastic moduli. Changes in elastic moduli would most likely be due to lithium deposition. Unfortunately, few specimens could be produced for this study, and even worse was that the RUS results for the LLZO specimens were different from billet to billet. When specimens can be produced with consistent elastic moduli values, the intended study should take place. If this work continues, the number of variables should be reduced, for instance: if all the work could be done in a glove box, or a moisture free environment, the risk of the materials interacting with the atmosphere would be reduced. Other methods could also be utilized to reduce the number of variables in play during the experimental procedure, but these would have to be determined by the researchers who continue the study. Ultimately, reducing the variables and having consistent specimens, should allow for further progress in this study.

REFERENCES

REFERENCES

[Amine 2014] Amine, K., Kanno, R., Tzeng, Y. Rechargeable lithium batteries and beyond: Progress, challenges, and future directions. *MRS Bulletin* 39 (2014) 395–401.

[ASTM standard E 2001-98 1999] ASTM standard E 2001-98. Standard Guide for Resonant Ultrasound Spectroscopy for Defect Detection in Both Metallic and Non-metallic Parts. 100 Barr Harbor Dr., West Conshohocken, Pa, 1999.

[Aurbach 2002] Aurbach, D., Zinigrad, E., Cohen, Y., Teller, H. A short review of failure mechanisms of lithium metal and lithiated graphite anodes in liquid electrolyte solutions. *Solid State Ionics* 148 (2002) 405–416.

[Awaka 2011] Awaka, J., Takashima, A., Kataoka, K., Kijima, N., Idemoto, Y., Akimoto, J. Crystal structure of fast lithium-ion-conducting cubic $Li_7La_3Zr_2O_{12}$. *Chemistry Letters* 40 (2011) 60–62.

[Barsoum 1997a] Barsoum, M.W. Composite Crystal Structures. In: R. Gibala, M. Tirrell, C.A. Wert, eds., Fundamentals of Ceramics. McGraw-Hill, New York, 1997, 70–73.

[Barsoum 1997b] Barsoum, M.W. Phase Equilibria. In: R. Gibala, M. Tirrell, C. Wert, eds., Fundamentals of Ceramics. McGraw-Hill, New York, 1997, 271–288.

[Barsoum 1997c] Barsoum, M.W. Mechanical Properties: Fast Fracture. In: R. Gibala, M. Tirrell, C. Wert, eds., Fundamentals of Ceramics. McGraw-Hill, New York, 1997, 391–439.

[Barton 1962] Barton, J.L., Bockris, J.O. The electrolytic growth of dendrites from ionic solutions. *Proceedings of the Royal Society A: Mathematical, Physical and Engineering Sciences* 268 (1962) 485–505.

[Bower 1994] Bower, A.F., Fleck, N.A. Brittle fracture under contact a sliding. *Journal of the Mechanics and Physics of Solids* 42 (1994) 1375–1396.

[Brandt 1994] Brandt, K. Historical development of secondary lithium batteries. *Solid State Ionics* 69 (1994) 173–183.

[Brissot 1999] Brissot, C., Rosso, M., Chazalviel, J., Lascaud, S. Dendritic growth mechanisms in lithiumrpolymer cells. *Journal of Power Sources* 81-82 (1999) 925–929.

[Bruce 2008] Bruce, P.G. Energy storage beyond the horizon: Rechargeable lithium batteries. *Solid State Ionics* 179 (2008) 752–760.

[Budiansky 1975] Budiansky, B., O'Connell, R.J. Elastic moduli of a cracked solid. *International Journal of Solids and Structures* 12 (1975) 81–97.

[Case 1993] Case, E.D., Kim, Y. The effect of surface-limited microcracks on the effective Young's modulus of ceramics. *Journal of Materials Science* 28 (1993) 1885–1900.

[Case 1980] Case, E.D., Smyth, J.R., Hunter, O. Grain-size dependence of microcrack initiation in brittle materials. *Journal of Materials Science* 15 (1980) 149–153.

[Chatani 1987] Chatani, Y., Okamura, S. Crystal structure of poly(ethylene oxide)- sodium iodide complex. *Polymer* 28 (1987) 1815–1820.

[Chau 2007] Chau, K.T., Chan, C.C. Emerging energy-efficient technologies for hybrid electric vehicles. *Proceedings of the IEEE* 95 (2007) 821–835.

[Christensen 1972] Christensen, R.M., Waals, F.M. Effective stiffness of randomly oriented fibre composites. *Journal of Composite Materials* 6 (1972) 518–535.

[Curtis 1978] Curtis, P.T., Bader, M.G., Bailey, J.E. The stiffness and strength of a polyamide thermoplastic reinforced with glass and carbon fibres. *Journal of Materials Science* 3 (1978) 377–390.

[Darrow 1969] Darrow, M.S., White, W.B., Roy, R. Micro-indentation hardness variation as a function of composition for polycrystalline solutions in the systems PbS/PbTe, PbSe/PbTe, and PbS/PbSe. *Journal of Materials Science* 4 (1969) 313–319.

[Dean 1973] Dean, G.D., Turner, P. The elastic properties of carbon fibres and their composites. *Composites* 4 (1973) 174–180.

[Delucchi 2014] Delucchi, M. a, Yang, C., Burke, a F., Ogden, J.M., Kurani, K., Kessler, J., Sperling, D. An assessment of electric vehicles: technology, infrastructure requirements, greenhouse-gas emissions, petroleum use, material use, lifetime cost, consumer acceptance and policy initiatives. *Philosophical transactions. Series A, mathematical, physical, and engineering sciences* 372 (2014) 20120325.

[Dollé 2002] Dollé, M., Sannier, L., Beaudoin, B., Trentin, M., Tarascon, J.-M. Live scanning electron microscope observations of dendritic growth in lithium/polymer cells. *Electrochemical and Solid-State Letters* 5 (2002) A286.

[Dunn 2011] Dunn, B., Kamath, H., Tarascon, J.-M. Electrical energy storage for the grid: a battery of choices. *Science* (New York, N.Y.) 334 (2011) 928–35.

[Ebert 1976] Ebert, L.B. Intercalation compounds of graphite. *Annual Review of Science* 6 (1976) 181–213.

[Fan 2012] Fan, X., Case, E.D., Baumann, M.J. The effect of indentation-induced microcracks on the elastic modulus of hydroxyapatite. *Journal of Materials Science* 47 (2012) 6333–6345.

[Fan 2013a] Fan, X., Case, E.D., Lu, X., Morelli, D.T. Room temperature mechanical properties of natural-mineral-based thermoelectrics. *Journal of Materials Science* 48 (2013) 7540–7550.

[Fan 2013b] Fan, X., Case, E.D., Yang, Q., Nicholas, J.D. Room temperature elastic properties of gadolinia-doped ceria as a function of porosity. *Ceramics International* 39 (2013) 6877–6886.

[Fergus 2010] Fergus, J.W. Ceramic and polymeric solid electrolytes for lithium-ion batteries. *Journal of Power Sources* 195 (2010) 4554–4569.

[Fletcher 2011] Fletcher, S. Bottled Lightning: Super batteries, electric cars, and the new lithium economy. Hill and Wang, New York, 2011.

[Geiger 2011] Geiger, C. a, Alekseev, E., Lazic, B., Fisch, M., Armbruster, T., Langner, R., Fechtelkord, M., Kim, N., Pettke, T., Weppner, W. Crystal chemistry and stability of "$Li_7La_3Zr_2O_{12}$" garnet: a fast lithium-ion conductor. *Inorganic Chemistry* 50 (2011) 1089–97.

[Gireaud 2006] Gireaud, L., Grugeon, S., Laruelle, S., Yrieix, B., Tarascon, J.M. Lithium metal stripping/plating mechanisms studies: A metallurgical approach. *Electrochemistry Communications* 8 (2006) 1639–1649.

[Goodenough 2012] Goodenough, J.B. Rechargeable batteries: challenges old and new. *Journal of Solid State Electrochemistry* 16 (2012) 2019–2029.

[Goodenough 2010] Goodenough, J.B., Kim, Y. Challenges for rechargeable Li batteries. *Chemistry of Materials* 22, 587–603, (2010) .

[Halliday 1966] Halliday, D., Resnick, R. Physics. Wiley, New York, 1966.

[Harry 2014] Harry, K.J., Hallinan, D.T., Parkinson, D.Y., MacDowell, A. a, Balsara, N.P. Detection of subsurface structures underneath dendrites formed on cycled lithium metal electrodes. *Nature Materials* 13 (2014) 69–73.

[Hassan 2005] Hassan, F.E.H., Akbarzadeh, H. First-principles investigation of BN_xP_{1-x}, BN_xAs_{1-x} and BP_xAs_{1-x} ternary alloys. *Materials Science and Engineering:* B 121 (2005) 170–177.

[Hermann 2014] Hermann, M., Saravi, M. A First Course in Ordinary Differential Equations. Springer, New York, 2014.

[Hoenig 1979] Hoenig, A. Elastic moduli of a non-randomly cracked body. *International Journal of Solids and Structures* 15 (1979) 137–154.

[Huggins 2009] Huggins, R.A. Advanced Batteries. Springer, Stanford, 2009.

[Hull 1981] Hull, D. Elastic Properties. In: An Introduction to Composite materials. Cambridge University Press, Cambridge, 1981, 81–100.

[Islam 2011] Islam, M.A., Begum, K. prediction models for the elastic modulus of fiber-reinforced polymer composites: An analysis. *Journal of Scientific Research* 3 (2011) .

[Jasinski 1967] Jasinski, R. High-Energy Batteries. Plenum Press, New York, 1967.

[Jen 1991] Jen, S.U., Chen, T.P., Chang, S.A. Electrical resistivity of Co-Ni-Pd and Co-Pd alloys. *Journal of Applied Physics* 70 (1991) 5831.

[Jeong 2008] Jeong, S.K., Seo, H.Y., Kim, D.H., Han, H.K., Kim, J.G., Lee, Y.B., Iriyama, Y., Abe, T., Ogumi, Z. Suppression of dendritic lithium formation by using concentrated electrolyte solutions. *Electrochemistry Communications* 10 (2008) 635–638.

[Johnson 1998] Johnson, B.A., White, R.E. Characterization of commercially available lithium-ion batteries. *Journal of Power Sources* 70 (1998) 48–54.

[Kanno 1989] Kanno, R., Takeda, Y., Ichikawa, T., Nakanishi, K., Yamamoto, O. Carbon as negative electrodes in lithium secondary cells. *Journal of Power Sources* 26 (1989) 535–543.

[Kasap 2007] Kasap, S.O. Electrical and Thermal Conduction in Solids. In: Principles of Electron Materials and Devices. McGraw-Hill, New York, 2007, 125–139.

[Kim 1993a] Kim, Y., Case, E.D. The effect of surface-limited microcracks on the effective Young ' s modulus of ceramics Part II Application of analysis to particular microcrack geometries. *Journal of material science* 28 (1993) 1901–1909.

[Kim 1993b] Kim, Y., Case, E.D., Gaynor, S. The effect of surface-limited microcracks on the effective Young's modulus of ceramics Part III Experiments. *Journal of material science* 28 (1993) 1910–1918.

[Kingery 1976a] Kingery, W.D., Bowen, H.K., Uhlmann, D.R. Elasticity, Anelasticity and Strength. In: Introduction to Ceramics. Wiley, New York, 1976, 769–815.

[Kingery 1976b] Kingery, W.D., Bowen, H.K., Uhlmann, D.R. Solid solutions. In: Introduction to Ceramics. Wiley, New York, 1976, 131–139.

[Kriz 1979] Kriz, R.D., Stinchcomb, W.W. Elastic moduli of transversely isotropic graphite fibers and their composites. *Experimental Mechanics* 19 (1979) 41–49.

[Kummer 1972] Kummer, J.T. Beta-alumina electrolytes. *Progress in Solid State Chemistry* 7 (1972) 141–175.

[Lawn 2011] Lawn, B.R., Cook, R.F. Probing material properties with sharp indenters: a retrospective. *Journal of Materials Science* 47 (2011) 1–22.

[Lee 1968] Lee, L.H. Strength-composition relationships of random short glass fiber-thermoplastics composites. Polymer Engineering and Science 9 (1968) 213–224.

[Leisure 2004] Leisure, R.G., Foster, K., Hightower, J.E., Agosta, D.S. Internal friction studies by resonant ultrasound spectroscopy. *Materials Science and Engineering* A 370 (2004) 34–40.

[Li 2014] Li, Z., Huang, J., Yann Liaw, B., Metzler, V., Zhang, J. A review of lithium deposition in lithium-ion and lithium metal secondary batteries. *Journal of Power Sources* 254 (2014) 168–182.

[Manera 1977] Manera, M. Elastic properties of randomly oriented short fiber-glass composites. *Journal of Composite Materials* 11 (1977) 235–247.

[Meier 2014] Meier, K., Laino, T., Curioni, A. Solid-state electrolytes: revealing the mechanisms of li-ion conduction in tetragonal and cubic llzo by first-principles calculations. *The Journal of Physical Chemistry C* (2014) 6668–6679.

[Migliori 1997] Migliori, A., Sarrao, J.L. Resonant Ultrasound Spectroscopy. Wiley, New York, 1997.

[Migliori 1993] Migliori, A., Sarrao, J.L., Visscher, M., Bell, T.M., Lei, M., Fisk, Z., Leisure, R.G. Resonant ultrasound spectroscopic techniques for measurement of the elastic moduli of solids. *Physica B* 183 (1993) 1–24.

[Miyashiro 2005] Miyashiro, H., Seki, S., Kobayashi, Y., Ohno, Y., Mita, Y., Usami, A. All-solid-state lithium polymer secondary battery with $LiNi_{0.5}Mn_{1.5}O_4$ by mixing of Li_3PO_4. *Electrochemistry Communications* 7 (2005) 1083–1086.

[Mizushima 1980] Mizushima, K., Jones, P.C., Wiseman, P.J., Goodenough, J.B. A new cathode material for batteries of high energy density. *Materials Research Bulletin*. 15 (1980) 783–789.

[Mogi 2001] Mogi, R., Inaba, M., Abe, T., Ogumi, Z. In situ atomic force microscopy observation of lithium deposition at an elevated temperature. *Journal of Power Sources* 97-98 (2001) 265–268.

[Mokhtari 2004] Mokhtari, A., Akbarzadeh, H. First principles investigation of the electronic and structural properties of $Mg_{3x}Be_{3-3x}N_2$ ternary alloy. *Journal of Physics: Condensed Matter* 16 (2004) 6063–6074.

[Monroe 2005] Monroe, C., Newman, J. The impact of elastic deformation on deposition kinetics at lithium/polymer interfaces. *Journal of The Electrochemical Society* 152 (2005) A396.

[Mori 1996] Mori, K., Nishimura, K. Superconductivity and electrical resistivity in $Zr_2(Co_{1-x}M_x)$ system (M=Ni,Fe). 2*1st International Conference on Low Temperature Physics* 1996, 861–862.

[Murugan 2011] Murugan, R., Ramakumar, S., Janani, N. High conductive yttrium doped $Li_7La_3Zr_2O_{12}$ cubic lithium garnet. *Electrochemistry Communications* 13 (2011) 1373–1375.

[Murugan 2007] Murugan, R., Thangadurai, V., Weppner, W. Fast lithium ion conduction in garnet-type $Li_7La_3Zr_2O_{12}$. *Angewandte Chemie (International ed. in English)* 46 (2007) 7778–81.

[Nagy 1997] Nagy, G., Sugimoto, Y., Denuault, G. Three-dimensional random walk simulations of diffusion controlled electode processes: (I) A hemisphere, disc and growing hemisphere. *Journal of Electroanalytical Chemistry* 433 (1997) 167–173.

[Nanjundaswamy 1997] Nanjundaswamy, K.S., Goodenough, J.B., Padhi, A.K. Phospho-olivines as positive-electrode materials for rechargeable lithium batteries. *J. Electrochem. Soc.*, 144 (1997) 1188–1194.

[Ni 2012] Ni, J.E., Case, E.D., Sakamoto, J., Rangasamy, E., Wolfenstine, J. Room temperature elastic moduli and Vickers hardness of hot-pressed LLZO cubic garnet. *Journal of Materials Science* 47 (2012) 7978–7985.

[Ogi 2006] Ogi, H., Niho, H., Hirao, M. Internal-friction mapping on solids by resonance ultrasound microscopy. *Applied Physics Letters* 88 (2006) 141110.

[Ohanian 1985] Ohanian, H.C. Physics. W.W. Norton & Company, New York, 1985.

[Orsini 1998] Orsini, F., Du Pasquier, A., Beaudoin, B., Tarascon, J.M., Trentin, M., Langenhuizen, N., De Beer, E., Notten, P. In situ scanning electron microscopy (SEM) observation of interfaces within plastic lithium batteries. *Journal of Power Sources* 76 (1998) 19–29.

[Pan 1996] Pan, N. The elastic constants of randomly oriented fiber composites: A new approach to prediction. *Science and Engineering of composite materials* 5 (1996) 63–72.

[Park 2008] Park, H.E., Hong, C.H., Yoon, W.Y. The effect of internal resistance on dendritic growth on lithium metal electrodes in the lithium secondary batteries. *Journal of Power Sources* 178 (2008) 765–768.

[Ponton 1989] Ponton, C.B., Rawlings, R.D. Vickers indentation fracture toughness test Part 1 Review of literature and formulation of standardised indentation toughness Equations. *Materials Science And Technology* 5 (1989) 865–872.

[Popplewell 1907] Popplewell, W.C. Strength of Materials. Oliver and Boyd, London, 1907.

[Purushothaman 2006] Purushothaman, B.K., Landau, U. Rapid charging of lithium-ion batteries using pulsed currents. *Journal of The Electrochemical Society* 153 (2006) A533.

[Qi 2010] Qi, Y., Harris, S.J. In Situ Observation of Strains during Lithiation of a Graphite Electrode. *Journal of The Electrochemical Society* 157 (2010) A741.

[Rangasamy 2012] Rangasamy, E., Wolfenstine, J., Sakamoto, J. The role of Al and Li concentration on the formation of cubic garnet solid electrolyte of nominal composition $Li_7La_3Zr_2O_{12}$. *Solid State Ionics* 206 (2012) 28–32.

[Rao 2003] Rao, S.S., Ravinder, D. Composition dependence of elastic moduli of gadolinium-substituted nickel–zinc ferrites. *Materials Letters* 57 (2003) 3802–3804.

[Ravinder 2001] Ravinder, D., Alivelumanga, T. Room temperature elastic behaviour of cadmium substituted manganese ferrites. *Materials Letters* 49 (2001) 1–6.

[Reddick 1955] Reddick, H.W., Miller, F.H. Advanced Mathematics for Engineers. Wiley, 1955.

[Ren 2009] Ren, F., Case, E.D., Morrison, A., Tafesse, M., Baumann, M.J. Resonant ultrasound spectroscopy measurement of Young's modulus, shear modulus and Poisson's ratio as a function of porosity for alumina and hydroxyapatite. *Philosophical Magazine* 89 (2009) 1163–1182.

[Ren 2007] Ren, F., Case, E.D., Timm, E.J., Schock, H.J. Young's modulus as a function of composition for an n-type lead–antimony–silver–telluride (LAST) thermoelectric material. *Philosophical Magazine* 87 (2007) 4907–4934.

[Rettenwander 2013] Rettenwander, D., Geiger, C.A., Amthauer, G. Synthesis and crystal chemistry of the fast Li-ion conductor $Li_7La_3Zr_2O_{12}$ doped with Fe. *Inorganic Chemistry*(2013) 8005–8009.

[Rice 1998] Rice, R.W. Porosity of Ceramics. Marcel Decker, New York, 1998.

[Rosso 2006] Rosso, M., Brissot, C., Teyssot, A., Dollé, M., Sannier, L., Tarascon, J.-M., Bouchet, R., Lascaud, S. Dendrite short-circuit and fuse effect on Li/polymer/Li cells. *Electrochimica Acta* 51 (2006) 5334–5340.

[Sakamoto 2013] Sakamoto, J., Rangasamy, E., Kim, H., Kim, Y., Wolfenstine, J. Synthesis of nano-scale fast ion conducting cubic $Li_7La_3Zr_2O_{12}$. *Nanotechnology* 24 (2013) 424005.

[Sandler 2002] Sandler, J., Werner, P., Shaffer, M.S.P., Demchuk, V., Altstadt, V., Windle, A.H. Carbon-nanofibre-reinforced poly (ether ether ketone) composites. *Composites: Part A* 33 (2002) 1033–1039.

[Schenk 1998a] Schenk, M., Dunog, L.T.H. Solid-solution hardening of $Cd_{1-x}Zn_xTe$ bulk crystals. *Semiconductor Science and Technology* 13 (1998) 335–339.

[Schenk 1998b] Schenk, M., Silber, C. Lattice parameter and microhardness investigations on $CdTe_{1-x}Se_x$. *Material Science: Materials in Electronics* 9 (1998) 295–300.

[Schmidt 2014] Schmidt, R.D., Case, E.D., Lobo, Z., Thompson, T., Sakamoto, J., Zhou, X.-Y., Uher, C. Influence of silver nanoparticle addition, porosity, and processing technique on the mechanical properties of $Ba_{0.3}Co_4Sb_{12}$ skutterudites. *Journal of Materials Science* 49 (2014) 7192–7212.

[Sharp 1993] Sharp, S.J., Ashby, M.F., Fleck, N.A. Material response under static and sliding indentation loads. *Acta Metallurgica et Materialia*. 41 (1993) 685–692.

[Shchennikov 2003] Shchennikov, V. V, Ovsyannikov, S. V, Frolova, N.Y. High-pressure study of ternary mercury chalcogenides: phase transitions,mechanical and electrical properties. *Physics D: Applied Physics* 36 (2003) 2021–2026.

[Shimonishi 2011] Shimonishi, Y., Toda, A., Zhang, T., Hirano, A., Imanishi, N., Yamamoto, O., Takeda, Y. Synthesis of garnet-type $Li_{7-x}La_3Zr_2O_{12-1/2x}$ and its stability in aqueous solutions. *Solid State Ionics* 183 (2011) 48–53.

[Swain 1979] Swain, M.V. Microfracture about scratches in brittle solids. *Proceedings of the Royal Society A.* 366 (1979) 575–597.

[Tai 2008] Tai, N.-H., Yeh, M.-K., Peng, T.-H. Experimental study and theoretical analysis on the mechanical properties of SWNTs/phenolic composites. *Composites Part B: Engineering* 39 (2008) 926–932.

[Takada 2013] Takada, K. Progress and prospective of solid-state lithium batteries. *Acta Materialia* 61 (2013) 759–770.

[Tang 2009] Tang, M., Albertus, P., Newman, J. Two-dimensional modeling of lithium deposition during cell charging. *Journal of The Electrochemical Society* 156 (2009) A390.

[Tenenbaum 1985] Tenenbaum, M., Pollard, H. Ordinary Differential Equation: An elementary textbook for students of mathematics, engineering, and the sciences. Dover Publications, New York, 1985.

[Terada 1997] Terada, Y., Ohkubo, K., Mohri, T., Suzuki, T. Thermal conductivity in nickel solid solutions. *Journal of Applied Physics* 81 (1997) 2263.

[Thangadurai 2003] Thangadurai, V., Kaack, H., Weppner, W. Novel fast lithium ion conduction in garnet-type $Li_5La_3M_2O_{12}$ (M= Nb, Ta). *Journal of the American Ceramic Society*. 40 (2003) 437–440.

[Thompson 2014] Thompson, T., Wolfenstine, J., Allen, J.L., Johannes, M., Huq, A., David, I.N., Sakamoto, J. Tetragonal vs. cubic phase stability in Al – free Ta doped $Li_7La_3Zr_2O_{12}$ (LLZO). *Journal of Materials Chemistry A* 2 (2014) 13431.

[Trivisonno 1961] Trivisonno, J., Smith, C.S. Elastic constants of lithium-magnesium alloys. *Acta Metallurgica* 9 (1961) 1064–1071.

[Ulrich 2002] Ulrich, T., McCall, K.R., Guyer, R. a. Determination of elastic moduli of rock samples using resonant ultrasound spectroscopy. *The Journal of the Acoustical Society of America* 111 (2002) 1667.

[Vincient 1984] Vincient, C.A. Modern Batteries: An Introduction To Electrochemical Power Sources. Edward Arnold, London, 1984.

[Wachtman] Wachtman, J.B., Cannon, W.R., Matthewson, M.J. Indentation Test. In: *Mechanical Properties of Ceramics*. Wiley, New York, 2009, 106–115.

[Walsh 1965] Walsh, J.B. the Effect of cracks in rocks on Poisson's ratio. *Journalo F Geophysical Research* 70 (1965) 5249–5257.

[Wen 2012] Wen, J., Yu, Y., Chen, C. A review on lithium-ion batteries safety issues: Existing problems and possible solutions. *Materials Express* 2 (2012) 197–212.

[Whittingham 1976] Whittingham, M.S. Electrical energy storage and intercalation chemistry. *Science* (New York, N.Y.) 192 (1976) 1126–7.

[Whittingham 2012] Whittingham, M.S. History, evolution, and future status of energy storage. *Proceedings of the IEEE* 100 (2012) 1518–1534.

[Wolfenstine 2013] Wolfenstine, J., Jo, H., Cho, Y.-H., David, I.N., Askeland, P., Case, E.D., Kim, H., Choe, H., Sakamoto, J. A preliminary investigation of fracture toughness of $Li_7La_3Zr_2O_{12}$ and its comparison to other solid Li-ion conductors. *Materials Letters* 96 (2013) 117–120.

[Wolfenstine 2012a] Wolfenstine, J., Ratchford, J., Rangasamy, E., Sakamoto, J., Allen, J.L. Synthesis and high Li-ion conductivity of Ga-stabilized cubic $Li_7La_3Zr_2O_{12}$. *Materials Chemistry and Physics* 134 (2012) 571–575.

[Wolfenstine 2012b] Wolfenstine, J., Sakamoto, J., Allen, J.L. Electron microscopy characterization of hot-pressed Al substituted $Li_7La_3Zr_2O_{12}$. *Journal of Materials Science* 47 (2012) 4428–4431.

[Yamaki 1998] Yamaki, J., Tobishima, S., Hayashi, K., Nemoto, Y., Arakawa, M. A consideration of the morphology of electrochemically deposited lithium in an organic electrolyte. *Journal of Power Sources* 74 (1998) 219–227.

[Yao 1967] Yao, Y.Y., Kummer, J.T. Ion exchange properties of and rates of ionic diffusion in beta-alumina. *Journal Of Inorganic Nuclear Chemistry* 29 (1967) 2453–2475.

[Yazami 1983] Yazami, R., Universitaire, D. A reversible graphite-lithium electrochemical generators. *Journal of Power Sources* 9 (1983) 365–371.

[Yeh 2006] Yeh, M.-K., Tai, N.-H., Liu, J.-H. Mechanical behavior of phenolic-based composites reinforced with multi-walled carbon nanotubes. *Carbon* 44 (2006) 1–9.

[Yoon 2013] Yoon, H., Howlett, P.C., Best, a. S., Forsyth, M., MacFarlane, D.R. Fast charge/discharge of Li metal batteries using an ionic liquid electrolyte. *Journal of the Electrochemical Society* 160 (2013) A1629–A1637.

[Zadler 2004] Zadler, B.J., Le Rousseau, J.H.L., Scales, J. a., Smith, M.L. Resonant Ultrasound Spectroscopy: theory and application. *Geophysical Journal International* 156 (2004) 154–169.

[Zarudi 1996] Zarudi, I., Zhang, L., Mai, Y.W. Subsurface damage in alumina induced by single-point scratching. *Journal of material science* 31 (1996) 905–914.

[Zhang 2011] Zhang, W.-J. A review of the electrochemical performance of alloy anodes for lithium-ion batteries. *Journal of Power Sources* 196 (2011) 13–24.

[Zimmermann 2001] Zimmermann, A., Carter, W.C., Fuller, E.R. Damage evolution during microcracking of brittle solids. *Acta Materialia* 49 (2001) 127–137.